DISSERTATION

Investigation of inflammation-promoted gadolinium retention within the central nervous system in the EAE mouse model and *ex vivo*

Untersuchung der durch Entzündung vermittelten Gadolinium-Retention im zentralen Nervensystem am EAE-Mausmodell und *ex vivo*

zur Erlangung des akademischen Grades
Medical Doctor - Doctor of Philosophy (MD/PhD)

vorgelegt der Medizinischen Fakultät
Charité – Universitätsmedizin Berlin

von
Lina Carlotta Anderhalten

Erstbetreuung: Prof. Dr. rer. nat. Carmen Infante Duarte

Datum der Promotion: 29. November 2024

Table of contents

List of tables ... iii
List of figures ... iv
List of abbreviations ... v
Abstract ... 6
1 Introduction ... 10
1.1 Gadolinium-based contrast agents ... 10
1.2 Safety issues and retention of gadolinium after administration of GBCAs ... 10
1.3 Multiple sclerosis and blood-brain-barrier disruption ... 12
1.4 Contrast-enhanced MRI in the diagnosis of MS ... 14
1.5 Motivation, hypothesis, and aims of the thesis ... 14
2 In-depth Methods ... 16
2.1 Experimental autoimmune encephalomyelitis ... 16
2.2. Administration of GBCAs *in vivo* and study design ... 18
2.3 7 Tesla MRI *in vivo* ... 20
2.4 Sacrifice of mice and preparation of brain and blood samples ... 24
2.5 Hematoxylin and eosin staining ... 25
2.6 Inductively coupled plasma mass spectrometry ... 26
2.7 Laser ablation inductively coupled plasma mass spectrometry ... 28
2.8 MRI calibration in homogenized mouse brain tissue ... 30
2.9 Generation of organotypic hippocampal slice cultures ... 31
2.10 Establishment of optimal *ex vivo* culture conditions ... 33
2.11 *Ex vivo* assessment of the effects of GBCAs on neuronal viability ... 35
2.12 Imaging mass cytometry ... 36
2.13 Statistical analysis ... 37
3 Essential Results ... 39
3.1 Clinical and histological signs of EAE ... 39
3.2 T_1 relaxometry detects enhanced T_1 time shortening in EAE brains ... 40
3.3 LA-ICP-MS confirms augmented Gd retention in EAE cerebella ... 42
3.4 LA-ICP-MS detects higher Zn levels within the CN of EAE mice ... 43
3.5 ICP-MS reveals enhanced Gd blood levels until day 40 p.f.i. of both GBCAs ... 44
3.6 *In vivo* T_1 relaxometry underestimates shortening of cerebellar T_1 relaxation times after gadopentetate administration ... 45
3.7 Gadopentetate induces neuronal cell death in chronic hippocampal slices ... 47
3.8 IMC reveals homogeneous Gd retention in brain slices post-GBCA treatment ... 48
3.9 ICP-MS quantifies Gd retention in chronic slices after GBCA treatment ... 49

4 Discussion 50
  4.1 Summary of essential results 50
  4.2 Interpretation of *in vivo* results on inflammation-promoted Gd retention 50
  4.3 Interpretation of *ex vivo* results on GBCA toxicity during inflammation 56
  4.4 Quantitative T_1 relaxometry for monitoring of Gd retention 58
  4.5 Limitations of the study 59
  4.6 Implications for clinical practice and future directions 60
5 Conclusion 62
Reference list 63
Statutory declaration 72
Declaration of your own contribution to the publications 73
Printing copy of the publication 75
Curriculum vitae 87
Publication list 89
Acknowledgments 90

List of tables

Table 1: Clinical assessment of EAE severity 18
Table 2: Parameters of 2-dimensional MRI sequences 24
Table 3: Instrumental parameters of the ICP-MS system 28
Table 4: Instrumental parameters of the LA-ICP-MS system 30
Table 5: Determination of suitable culture media ……….. 34
Table 6: Analysis of Gd blood content using ICP-MS 45
Table 7: 7 Tesla MRI calibration for GBCAs in homogenized mouse brain 45
Table 8: Analysis of Gd content within chronic hippocampal slices using ICP-MS ….... 49

List of figures

Figure 1: Hypothetical behavior of GBCAs after uptake into the CNS 12

Figure 2: Illustration of the neuropathology of MS ………………………………………. 13

Figure 3: Illustration of ear punching for mouse identification …………………………..… 18

Figure 4: Experimental setup for assessment of Gd retention *in vivo* ……….………..... 20

Figure 5: Schematic illustration of the MRI principle …………………………….……..… 21

Figure 6: Schematic illustration of the LA-ICP-MS system ……………….…………..…. 29

Figure 7: Sterile generation of hippocampal slice cultures ………………….……………. 32

Figure 8: Experimental setup for assessment of Gd toxicity *ex vivo* …………………… 36

Figure 9: Clinical and histological assessment of EAE-related properties ……….….… 39

Figure 10: 7 Tesla MRI relaxometry of the CN region *in vivo* ……………………….…... 41

Figure 11: Analysis of cerebellar Gd retention using LA-ICP-MS ……………………..... 42

Figure 12: Analysis of the distribution of cerebellar elements using LA-ICP-MS ……... 44

Figure 13: 7 Tesla MRI calibration *in vitro* ………………………………………………... 46

Figure 14: Toxicity assessment of GBCAs *ex vivo* 48

Figure 15: Assessment of Gd retention within the DG *ex vivo* ………………………… 49

Figure 16: Discussion of essential *in vivo* results …………………………………….….. 55

List of abbreviations

ABA, Allen mouse brain atlas

BBB, blood-brain-barrier

Ca, calcium

CE, contrast-enhanced

CFA, complete Freund's adjuvant

CFP, cyan fluorescent protein

CNS, central nervous system

CN, deep cerebellar nuclei

CSF, cerebrospinal fluid

Cu, copper

DG, dentate gyrus

DN, dentate nucleus

EAE, experimental autoimmune encephalomyelitis

ECM, extracellular matrix

FBS, fetal bovine serum

FDA, US Food and Drug Administration

Fe, iron

fg, femtogram

GAG, glycosaminoglycans

GBCA, gadolinium-based contrast agent

Gd, gadolinium

$\mathbf{Gd^{3+}}$, ionic gadolinium

$\mathbf{GdPO_4}$, gadolinium phosphate salt

$\mathbf{^1H}$, hydrogen nucleus

HC, healthy control

Hz, Hertz

H&E, hematoxylin and eosin

ICP-MS, inductively coupled plasma mass spectrometry

i.v., intravenous

IMC, imaging mass cytometry

LA-ICP-MS, laser ablation inductively coupled plasma mass spectrometry

MRI, magnetic resonance imaging

MS, multiple sclerosis

ms, milliseconds

NMDA, N-methyl-D-aspartic acid

NMR, nuclear magnetic resonance

NSF, nephrogenic systemic fibrosis

P, phosphorus

PFA, paraformaldehyde

p.f.i., post-final injection

PI, propidium iodide

PLP, proteolipid protein

PPMS, primary progressive multiple sclerosis

PTX, pertussis toxin

RF, radio frequency

ROI, region of interest

ROS, reactive oxygen species

RRMS, relapsing-remitting multiple sclerosis

$\mathbf{R_1}$, T_1 relaxation rate

$\mathbf{r_1}$, T_1 relaxivity

SI, signal intensity

SF, sector-field

TNFα, tumor necrosis factor-alpha

$\mathbf{T_1}$, T_1 relaxation time

µM, micromolar

Zn, zinc

Abstract

Multiple sclerosis (MS) is a chronic inflammatory disease of the central nervous system (CNS) that is characterized by autoimmune-driven inflammation, resulting in myelin destruction and damage to neuronal axons and cell bodies. These alterations manifest as CNS lesions in magnetic resonance imaging (MRI). In MS patients, MRI has shown the presence of cerebral gadolinium (Gd) retention following repeated injections of mainly linear gadolinium-based contrast agents (GBCAs). Using the experimental autoimmune encephalomyelitis (EAE), a mouse model of MS, we previously observed that EAE mice exhibited enhanced cerebellar short-term Gd retention compared to healthy controls (HC) following injections of gadopentetate dimeglumine. Since MS patients generally undergo multiple contrast-enhanced (CE) MRIs throughout their lives, the concern of augmented Gd retention and potential long-term consequences may be specifically relevant for them. This thesis aimed to investigate the long-term character of inflammation-promoted brain Gd retention and contributing factors after repeated application of linear gadopentetate or macrocyclic gadobutrol. By combining longitudinal T_1 mapping of the brain and cross-sectional (laser ablation-) inductively coupled plasma mass spectrometry (LA-/ICP-MS) assessments of blood and cerebellum, we took an interdisciplinary approach to address Gd retention patterns and kinetics in EAE and HC mice. MRI calibration was performed to assess the impact of inflammation on Gd bonds and compare the binding behavior of the two tested GBCAs. In addition, this thesis presents the establishment of an *ex vivo* model of living brain tissue and its utilization to determine Gd-induced neurocytotoxicity under naïve and inflammatory conditions. Within this model, the retained Gd content was visualized by Imaging Mass Cytometry (IMC), and quantified by ICP-MS. Quantitative T_1 relaxometry and LA-ICP-MS results confirmed that in EAE mice Gd retention was enhanced after injections of both GBCAs. While gadopentetate led to persistent retention, particularly inside the inflamed cerebellar nuclei (CN), gadobutrol caused weak and diffuse Gd content, which cleared over the observational period. MRI calibration showed that *in vivo* MRI underestimated the T_1 effect of Gd after the administration of gadopentetate, suggesting that Gd may be partially bound in insoluble deposits. After incubation with gadopentetate *ex vivo*, retained Gd content at approximately 1.5 mM led to a reduction in neuronal viability, which further decreased under inflammatory conditions. Taken together, the results indicate that inflammation promotes the extent of Gd brain retention, particularly after linear GBCA administration, and significantly influences its retention pattern, binding to endogenous ligands, and cytotoxic potential. Thus, multiple administrations of mainly linear GBCAs may pose a long-term risk for patients suffering from chronic neuroinflammatory disorders like MS.

Zusammenfassung

Die Multiple Sklerose (MS) ist eine chronisch-entzündliche Autoimmunerkrankung, bei der es zur Bildung von Entmarkungsherden und neuronaler Schädigung im zentralen Nervensystem (ZNS) kommt. Die Magnetresonanztomographie (MRT) ermöglicht die Darstellung von resultierenden ZNS-Läsionen und ist essentiell für die MS-Diagnosestellung. In der MRT wurden nach Gabe von linearen Gadolinium-haltigen Kontrastmitteln (GdKM) zerebrale Gadolinium-(Gd-)Ablagerungen festgestellt. Unter Verwendung der Autoimmunenzephalomyelitis (EAE), einem MS-Mausmodell, konnten wir bereits zeigen, dass wiederholte Injektionen von Gadopentetat-Dimeglumin zu einer kurzfristigen Gd-Kleinhirnretention führten und dass dieser Effekt bei EAE-Mäusen im Vergleich zu gesunden Kontrollen (HC) verstärkt war. Diese Erkenntnis ist alarmierend, da MS-Patienten im Verlauf häufiger kontrastmittelverstärkte MRTs erhalten als Gesunde. Ziel dieser Studie war es, die durch Entzündung vermittelte Gd-Retention im Gehirn nach multipler Gabe von linearem Gadopentetat oder makrozyklischem Gadobutrol zu definieren und Langzeitfolgen verstärkter Ablagerung zu analysieren. Hierfür haben wir Gd-Retentionsmuster und -kinetik in EAE- und HC-Gehirnen mittels longitudinalem T_1-Mapping verglichen und interdisziplinär mit Blut- und Kleinhirnanalysen mittels (Laserablations-) induzierter gekoppelter Plasma-Massenspektrometrie (LA-/ICP-MS) kombiniert. Eine MRT-Kalibrierung sollte potenziell entstandene Gd-Verbindungen unter naiven und entzündlichen Bedingungen analysieren und Unterschiede im Bindungsverhalten der beiden GdKM-Typen bewerten. Außerdem wurde ein *ex vivo*-Modell von lebendem Hirngewebe etabliert, das zur Bestimmung potentiell zytotoxischer Gd-Wirkungen genutzt wurde. Das retinierte Gd konnte *ex vivo* mittels Imaging-Massenzytometrie (IMC) visualisiert und mittels ICP-MS quantifiziert werden. Die Ergebnisse der quantitativen T_1-Relaxometrie- und LA-ICP-MS-Analysen bestätigten, dass die Gd-Retention in EAE-Gehirnen nach Gabe beider GdKMs verstärkt war. Nach Gadopentetat-Injektion lagerte sich Gd vor allem in den Kleinhirnkernen ab und blieb über den gesamten Beobachtungszeitraum erhalten. Gadobutrol führte zu einer schwachen, diffuseren Retention, die im Studienverlauf effizient ausgewaschen wurde. Die MRT-Kalibrierung ergab, dass der T_1-verkürzende Effekt von Gd in der *in vivo* MRT nach linearer GdKM-Injektion unterschätzt wurde, was Resultat der Bildung unlöslicher Gd-Spezies sein könnte. In einem *ex vivo*-Paradigma neuronaler Entzündung zeigte ausschließlich Gadopentetat toxische Wirkungen auf Hirngewebe. Insgesamt stellten wir fest, dass die neuronale Entzündung das Ausmaß der Gd-Retention im ZNS vor allem nach Applikation von linearem GdKM förderte. Sie hatte Einfluss auf Retentionsmuster, das endogene Bindungsverhalten und das neurotoxische Potenzial von Gd. Die mehrfache Gabe linearer GdKM könnte daher Langzeitrisiken für Patienten mit chronisch-entzündlichen ZNS-Erkrankungen wie der MS darstellen.

1 Introduction

1.1 Gadolinium-based contrast agents

Gadolinium-based contrast agents (GBCAs) are commonly used in clinical and preclinical magnetic resonance imaging (MRI) to enhance contrasts in MR images and improve their diagnostic value (1). Since the introduction of GBCAs to clinical practice around three decades ago, their use steadily increased with around 30 million contrast-enhanced MRIs per year estimated in 2016. Around 25% of MRI procedures involved GBCA injections, particularly examinations of the central nervous system (CNS), i.e. spine and brain (2). Following intravenous (i.v.) injection, GBCAs rapidly distribute to extracellular spaces, unless natural barriers impede their infiltration (3). GBCAs used in clinical routine are low-molecular-weight compounds consisting of a paramagnetic gadolinium (Gd) ion (Gd^{3+}) and a chelate of linear or macrocyclic structure. Gd^{3+} increases the relaxation rate of surrounding water protons, resulting in a signal enhancement of the MR image (1). The molecular structure of the Gd^{3+} ligand mainly determines the thermodynamic and kinetic stability of a GBCA *in vivo*. While in linear GBCAs the polyaminocarboxylic chelate does not enclose Gd^{3+} completely, in macrocyclic agents it fully surrounds the ion like a rigid cage (2) (Figure 1).

1.2 Safety issues and retention of gadolinium after administration of GBCAs

Although free ionic Gd^{3+} is known to be highly toxic, chelation reduces GBCA toxicity by increasing the *in vivo* stability and solubility (1). All GBCAs were assumed to be inert and rapidly eliminated via the kidneys after i.v. administration (half-life of less than 2 h, 95% eliminated after 24h), remaining in their original structure as intact complex (2, 4). The clinical use of GBCAs was considered safe in patients with normal renal function during the past three decades due to a consistently low incidence of adverse effects (1, 5-7). In patients with kidney dysfunction, the renal clearance of GBCAs is reduced (8). In this context, Grobner was the first to assume a link between i.v. administration of GBCAs and the development of nephrogenic systemic fibrosis (NSF), a rare but serious condition in patients with advanced kidney disease (9). Preclinical animal studies correlated NSF-like skin lesions with the release of ionic Gd^{3+} from its ligand (10) and suggested the dissociation of GBCAs as a result of an extended residence inside the body (10-12).

However, more recently linear GBCAs were reported to cause Gd retention in various organs, including the CNS, after i.v. administration in patients with normal renal function (1, 13, 14). In 2014, Kanda *et al.* were the first to report on a relationship between previous linear GBCA administrations and elevated T_1 signal intensities (SI) in unenhanced cerebral T_1-weighted MRI scans, in particular within the dentate nucleus (DN) (15). The aforementioned findings were corroborated by multiple researchers in both human subjects (16-21) and animal models (22-28), primarily following multiple administrations of linear GBCAs. The amount of Gd deposited within neural tissue, specifically within the DN, was quantified through the utilization of inductively coupled plasma mass spectrometry (ICP-MS) or laser ablation ICP-MS (LA-ICP-MS) after the application of GBCAs *in vivo* (29-33).

There is increasing evidence that the probability of interstitial deposition is predominantly high for linear agents compared to macrocyclic GBCAs, irrespective of kidney function (1, 34-36). Using human serum at pH 7.4, Frenzel *et al.* demonstrated the reduced kinetic stability of linear GBCAs, resulting in dechelation, compared to macrocyclic GBCAs *ex vivo* (34). In the CNS *in vivo*, the thermodynamic and kinetic stability of GBCAs is more complex and dechelation may involve multiple equilibria (1). When entering areas of the brain physiologically rich in endogenous metals like copper (Cu), calcium (Ca) (37), iron (Fe) (38, 39), and zinc (Zn) (3, 40-42), linear GBCAs may gradually dissociate and release Gd^{3+} from its ligand. The endogenous metals can then bind to the ligand in a process called transmetallation, while free Gd^{3+} may bind to endogenous macromolecules as competing chelators. Thus, Gd^{3+} undergoes transchelation, which results in the formation of soluble Gd deposits (43) (illustrated in Figure 1). It was further demonstrated that released Gd^{3+} may react with anionic inorganic phosphates forming insoluble deposits of Gd phosphate salt ($GdPO_4$) (3, 34, 40) (Figure 1), leading to long-term retention within the CNS. Contrary to that, no permanent retention was observed for the kinetically stable macrocyclic GBCAs (44-48). Depending on the agent, macrocyclic compounds follow specific washout kinetics (44, 45), but are expected to be continuously cleared from the brain as intact chelate (26, 36, 49-51).

Accumulating evidence on Gd deposition has led to restrictions on the clinical routine application of linear GBCAs by the European Medicines Agency (52) as well as class warnings by the US Food and Drug Administration (FDA) (53). The FDA maintained the authorization for linear GBCAs, stating that clinicians should consider the characteristics of each specific GBCA cautiously and limit their utilization to reasonable applications (53). Regarding toxicity issues, so far there is no distinct evidence of clinical consequences following intracerebral Gd deposition (54-56). However, long-term retention of Gd may have delayed effects on the health of both patients with neuroinflammatory disorders and healthy individuals.

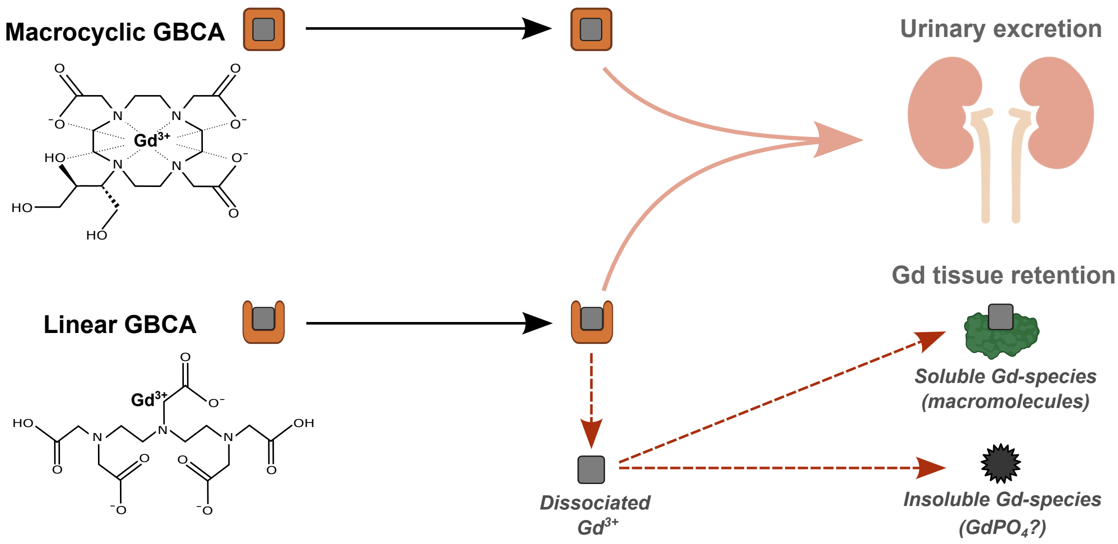

Figure 1: Hypothetical behavior of macrocyclic and linear GBCAs after uptake into the CNS *(own representation)*

1.3 Multiple sclerosis and blood-brain-barrier disruption

Multiple sclerosis (MS) is a chronic neuroinflammatory and neurodegenerative disease of the CNS affecting about 2.8 million people worldwide. It represents one of the leading causes of nontraumatic disability in young adults (57). The pathogenesis of MS involves a cell-mediated autoimmune response that causes myelin destruction and neuroaxonal damage inside the CNS, leading to the formation of multifocal lesions inside the brain and spinal cord (57, 58). Beyond focal inflammatory processes, diffuse white and gray matter pathology (i.e. demyelination and atrophy) contribute to the emergence of cognitive, motor, sensory, visual, and autonomic deficits in MS (57, 59). The most common clinical presentation of MS is the relapsing-remitting phenotype (RRMS), with intervals of intensified neurological disability followed by phases of recovery. This form can progress into a phase of gradual deterioration, which is then referred to as secondary progressive MS. Another form is primary progressive MS (PPMS), characterized by continuous clinical worsening without periods of remission (57, 59).

The blood-brain barrier (BBB) plays a complex role in immune surveillance and preservation of the CNS (59). It is composed of capillary endothelial cells, pericytes, basal lamina, astrocytes, and perivascular macrophages, forming the neurovascular unit (60). In MS, the breakdown of the BBB is believed to be a crucial step in the initiation and maintenance of the immune attack against CNS structures (Figure 2) (58, 59). The disruption of BBB integrity is characterized by the invasion of presumably peripherally activated auto-reactive mononuclear cells into the CNS via transmigration across endothelial cells of brain capillaries (58, 61). The induced immune response is amplified and self-sustained by the local activation of microglia and macrophages and the release of cytokines, auto-antibodies, free radicals, proteases, and other toxic mediators into the central compartment. In addition, proinflammatory leukocytes are continuously recruited from the peripheral compartment (58). Their ongoing invasion into the CNS and the prevailing proinflammatory milieu reinforce BBB impairment (60, 61).

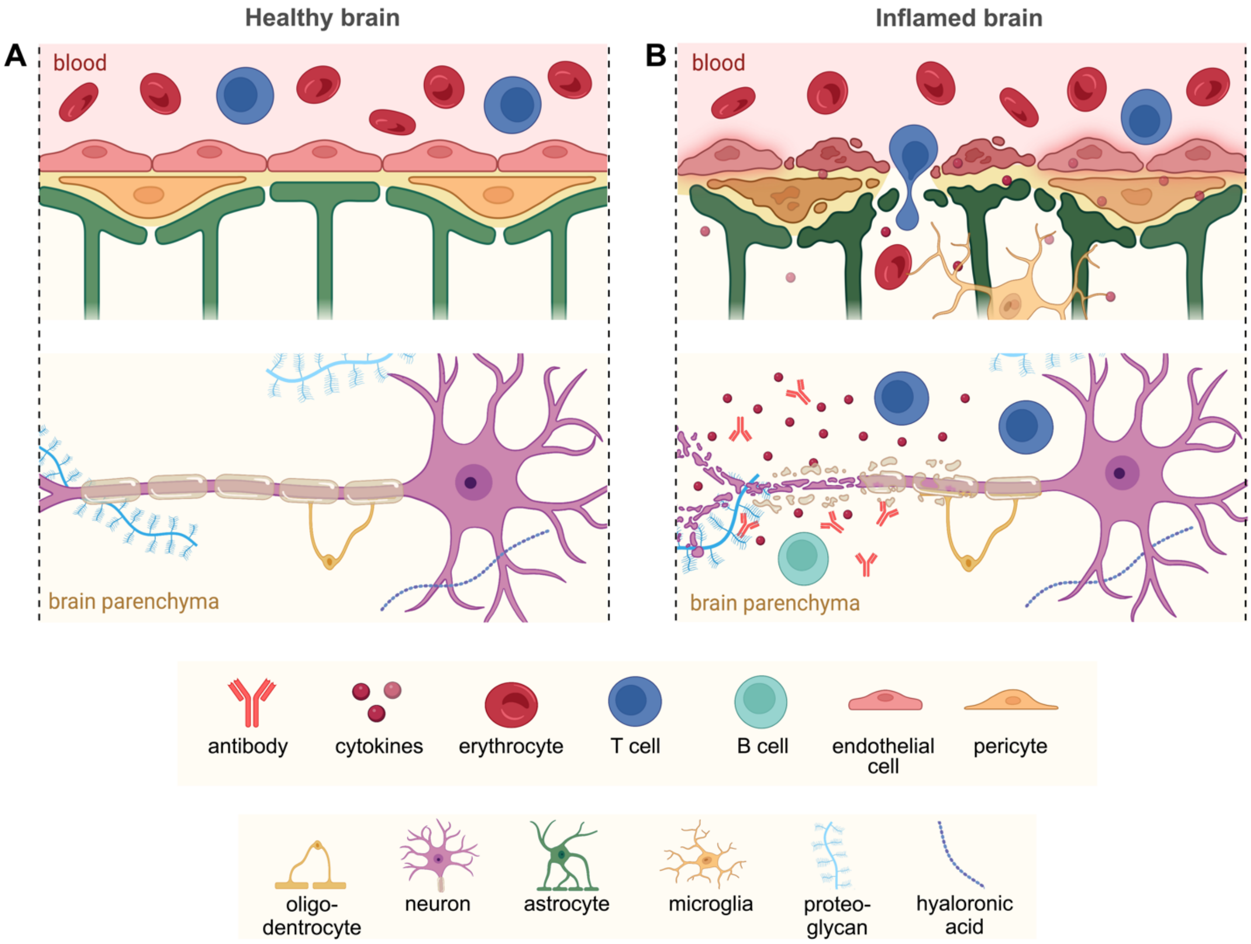

Figure 2: Illustration of the neuropathology of MS. A In the healthy CNS, the BBB is intact and protects the brain from external insults. **B** In MS and EAE, myelin-reactive T cells probably activated in the periphery as well as B cells and monocytes migrate into the CNS across the brain barriers, principally through a leaky BBB. Infiltrated immune cells, cytokines, and autoantibodies mediate demyelination and neuroaxonal damage, eventually resulting in oligodendrocyte and neuronal loss (*own representation*).

1.4 Contrast-enhanced MRI in the diagnosis of MS

MRI represents the common non-invasive imaging tool in the diagnosing and monitoring of MS in patients (62). In the clinical setting, conventional MRI provides information on the number, location, and size of MS lesions and general brain volume as a measure of atrophy. Focal demyelination and neuroaxonal loss can be assessed in T_2-weighted MRI scans (hyperintense regions) or T_1-weighted MRI scans ("black holes"). In addition, Gd-based contrast-enhanced (CE) T_1-weighted MRI detects active lesions in the early phase of inflammation (57, 63). Parenchymal extravasation of GBCAs (64, 65) reflects BBB leakage in MS and provides information on the magnitude of BBB impairment (62). In MS diagnosis, lesions are assessed for dissemination in time and space according to the McDonald criteria (63), which underwent repeated revisions during the last two decades (66-68). Evolving safety concerns about repetitive injections of GBCAs due to the risk of intracerebral retention have led to the revision of recommendations on the use of CE-MRI in MS patients (69). The standardized brain MRI protocol includes axial and sagittal T_2-weighted 3D-fluid-attenuated inversion recovery (FLAIR) sequences, an axial T_2-weighted sequence, and an axial T_1-weighted sequence post GBCA administration (doses of 0.1 mmol/kg body weight, macrocyclic agents only) using 1.5 or 3 Tesla scanners (69). The administration of GBCAs should be limited to the initial MS diagnosis to prove lesion dissemination in time (Gd-enhancing and non-enhancing lesions in baseline MRI scan), to exclude differential diagnoses, and to predict future disease activity. Contrast enhancement is not advised as a standard component of monitoring MS disease activity and treatment response, provided that a recent MRI scan (i.e. within approx. 12 months or 3-6 months after treatment initiation) is available (69).

1.5 Motivation, hypothesis, and aims of the thesis

In MS patients, intracerebral Gd retention was observed using MRI after multiple administrations of linear GBCAs (16, 70-75) and macrocyclic GBCAs (76, 77), albeit the latter has been controversially discussed (78, 79). The concern about Gd retention is of high relevance in MS patients as they, unlike the general average person, receive multiple CE-MRIs over the course of their lives. In experimental autoimmune encephalomyelitis (EAE), we previously demonstrated that neuroinflammation may facilitate brain retention of Gd after repeated i.v. injections of linear gadopentetate dimeglumine in the short term. Using synchrotron-based X-ray fluorescence microscopy, we observed that the deep cerebellar nuclei (CN) of EAE mice exhibited greater Gd deposits compared to healthy controls (HC) (80). We hypothesize that enhanced BBB permeability and inflammatory processes in the CNS may further contribute to increased cumulative Gd retention in MS, potentially increasing Gd toxicity and posing a long-term hazard to patients.

The insufficient knowledge about how linear and macrocyclic GBCAs behave in terms of magnitude, distribution pattern, and retention kinetics in inflamed vs. healthy brains, which factors contribute to Gd brain retention, and which long-term effects deposits may have on living neuronal tissue, motivated this doctoral thesis. In an interdisciplinary approach, this dissertation combines the quantitative investigation of dynamic inflammation-promoted Gd retention patterns in the EAE mouse model applying longitudinal T_1 relaxometry and cross-sectional ICP-MS/LA-ICP-MS assessments with the controlled *ex vivo* investigation of potential toxic GBCA effects on living brain tissue. Additional MRI calibration evaluated the potential forms of deposited Gd; how linear and macrocyclic GBCA differ in their binding behavior; and what effect neuroinflammation may have on it. I principally pursued three aims during my MD/PhD studies:

1. Investigation of the effect of neuroinflammation on the kinetics and distribution patterns of cerebellar long-term Gd retention after repeated administration of linear and macrocyclic GBCAs *in vivo* using the EAE mouse model.
2. Assessment of the effect of Gd retention on neuronal viability in chronic murine organotypic hippocampal slice cultures under inflamed and non-inflamed conditions *ex vivo*.
3. Investigation of potential bindings in which Gd may be present inside the brain parenchyma after linear and macrocyclic GBCA administration.

2 In-depth Methods

In addition to the methodology utilized in the study by Anderhalten et al. (81), which my MD/PhD thesis is based on, this chapter gives a detailed description of the methods established and applied during my doctorate.

2.1 Experimental autoimmune encephalomyelitis

The induction of EAE was done with the assistance of R. V. Silva. The weighting, scoring, and consequent sacrificing of mice were conducted by L. Anderhalten.

EAE is the most frequently employed rodent model of MS and recapitulates many of its molecular and cellular mechanisms, allowing for the investigation of disease pathogenesis and potential therapeutic effects (82). In both MS and EAE, the CNS white matter shows disseminated lesions related to the infiltration of mainly T-cells, B-cells, monocytes, and macrophages. Ongoing inflammation, demyelination, gliosis, and neuroaxonal damage ultimately lead to severe clinical disability (57, 58, 83). While the specific trigger of autoimmunity in MS remains unknown, the pathogenesis of EAE is induced artificially by immunization with CNS antigens (82). EAE is characterized by an invasion of the CNS by autoreactive mononuclear cells and an increasing breakdown of the BBB, showing strong histopathological similarities to those found in MS (61, 82, 83). In brief, professional antigen-presenting cells phagocytize CNS antigens after immunization, travel to lymph nodes or spleen, and interact with lymphocytes to form encephalitogenic T-cells. These peripherally activated T-cells and other mononuclear cells invade the brain via impaired BBB, causing inflammation and demyelination of axons (84). The EAE adheres to a typical clinical course with an initial prodromal phase of 10-15 days, succeeded by weight loss, ascending tail, and limb paralysis (83).

The development of encephalomyelitis resembling MS is determined by a combination of factors, including the specific autoantigens and strain involved (85). Depending on the myelin-derived peptide applied for immunization, the EAE disease course either follows a relapsing-remitting or a rather chronic form resembling the RRMS (85% of MS cases) or PPMS phenotype (15% of MS cases) (57, 83, 85). The immunization of SJL/J mice with proteolipid protein (PLP) causes a relapsing-remitting form of paralysis and is characterized by an initial peak of clinical disability and subsequent remission, allowing data collection during different stages in a relapsing disease setting (83, 85-87). Typically, lesions appear in the brainstem, spinal cord, optic nerve, cerebellum, and cerebral cortex, starting with perivascular and meningeal infiltration of leukocytes (82, 84). In contrast, immunization of C57BL/6 mice with myelin oligodendrocyte glycoprotein (MOG) represents a rather chronic form of EAE with a reduced tendency to resolve demyelination after the peak of disease and leads to pronounced inflammation of the spinal cord (83, 85-87).

EAE can be induced by active immunization with myelin peptides or by transferring encephalitogenic T cells generated in a donor mouse to a recipient animal (83, 87). In this study, we chose the active form of EAE induction in SJL/J mice, as from our experience it is less severe than the adoptive transfer model, ensuring a high overall survival of mice in our longitudinal study setup. Moreover, according to the 3R principle (88), it does not require both donor and recipient mice, leading to the use of lower numbers of experimental animals compared to the adoptive transfer EAE.

In the current study, 9-12 weeks-old female SJL/J mice (Janvier Labs, France) were assigned to the trial in a randomized manner. Since the incidence of MS worldwide is about three times greater in women than in men (57) and sex differences that may affect disease severity and progression should be excluded, we assigned only female mice to this study. The induction of EAE was carried out actively by subcutaneous immunization with an emulsion containing $PLP_{139-151}$ peptide (250 µg/mouse; purity 95%; Pepceuticals, Leicester, United Kingdom) and Mycobacterium tuberculosis H37Ra (800 µg/mouse; Difco, Franklin Lakes, NJ) in complete Freund's adjuvant (CFA; 100 µL/mouse). Each mouse received four subcutaneous injections of the emulsion - two injections provided underneath the armpits and on both sides of the flanks. The co-adjuvant Pertussis toxin (PTX; 250 ng/mouse; List, Biological Laboratories, Campbell, CA) was additionally applied intraperitoneally (i.p.) on day 0 (day of immunization) and day 2 of the *in vivo* study (Figure 4). PTX facilitates the entrance of autoreactive immune cells into the CNS across the BBB, most likely by increasing its permeability, and represents an integral part of active EAE induction (82).

Monitoring for clinical EAE signs was carried out daily according to Table 1. The score ranges from 0 (no disease) to 5 (EAE-induced death) and is well-established for monitoring clinical EAE severity. While paresis per definition is a partial loss of motor function, plegia defines its complete loss. The animals were weighed one to three times a day and from a weight loss of more than 15%, 200 µl of 5% glucose was injected i.p. daily to guard against further weight loss. Wet food and crushed nest material were provided ad libitum. All mice were marked by ear-punching for identification prior to GBCA application according to the standardized scheme displayed in Figure 3.

Table 1: Clinical assessment of EAE severity

EAE score	Clinical deficiency
0.00	No disease
0.25	(TPA)
0.50	TPA
0.75	TPA – TPL
1.00	TPL / TPA + RRW
1.25	TPA – TPL + RRW
1.50	TPL + RRW
1.75	(HPA) + TPA / TPL / RRW
2.00	HPA + TPA / TPL / RRW
2.50	HPA – HPL + TPA / TPL / RRW
3.00	HPL + TPA/ TPL/ RRW
4.00	FPA + TPL + HPL
4.50	FPL + TPL + HPL, moribund
5.00	EAE-induced death

Note: TPA= tail paresis, TPL= tail plegia, RRW= righting reflex weak (was tested 5 times per side), HPA= hindlimb paresis, HPL= hindlimb plegia, FPA= forelimb paresis, FPL= forelimb plegia. *(This scoring system aligns with the EAE scoring commonly employed by the FEM animal facility at Charité – Universitätsmedizin Berlin (CVK), consistent with the scoring used by Millward et al., 2017 (145); Wang et al., 2019 (80); and Anderhalten et al., 2022 (81).)*

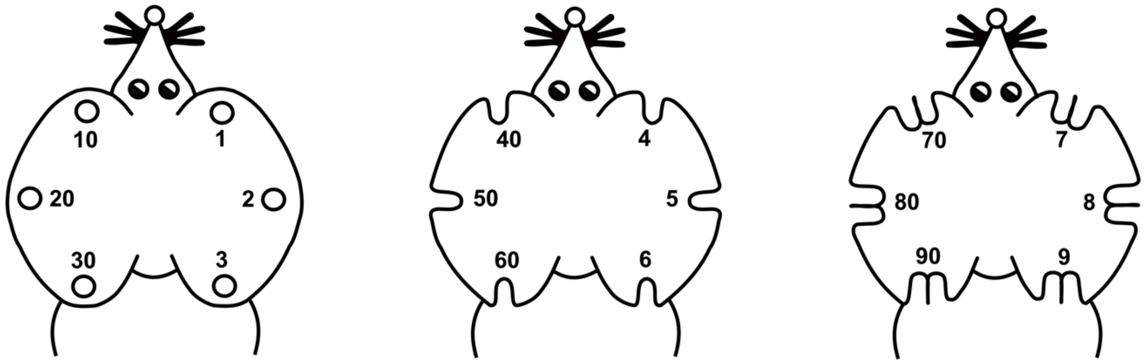

Figure 3: Illustration of ear punching producing notches for mouse identification *(own representation)*

2.2. Administration of GBCAs *in vivo* and study design

All i.v. injections of GBCAs were done by L. Anderhalten. The study design was established by C. Infante-Duarte, S. Wang, and L. Anderhalten.

Healthy control mice (HC, *n=24*) and EAE mice (*n*=29) received multiple i.v. injections of GBCA into the tail vein, starting on days 12 to 13 post-immunization when EAE mice reached the peak of clinical disability. All mice were exposed to eight daily injections of either a GBCA of linear structure (Gadopentetate dimeglumine; Magnevist, Bayer, Germany) or a macrocyclic structured agent (Gadobutrol; Gadovist, Bayer, Germany) at a cumulative dose of 20 mmol/kg body weight (BW; single doses of 2.5 mmol/kg) (chemical GBCA structures shown in Figure 1). To reduce stress and ensure the success of each application, a pause of two days was conducted after four consecutive injections followed by four additional injections.

Prior to GBCA injections, mice were transferred to a heating box (37°C) to achieve a dilatation of the venous system and to prevent the body temperature from dropping outside of the cage system. An additional infrared heat lamp was used to ensure continuous vasodilatation during injections. Injections were carried out with a small supply of isoflurane ($\leq$1% isoflurane, 30% O_2, 70% N_2O) via a face mask and the mice were held in a restrainer while the tail was gently pulled. The mouse tail was strictly cleaned with disinfectant (70% Ethanol) to avoid unsterile injection. GBCAs were applied to one of the tail veins using a 27-gauge disposable hypodermic needle (Sterican cannula, 0,40 x 20 mm, B. Braun Melsungen AG, Germany). The needle was inserted at an angle of approximately 30 degrees, then advanced half a cm into the vein to avoid slipping out, and the GBCA was slowly injected. A resistance-free advance of the needle and subsequent flow of blood back into the cannula was considered a sign of successful venipuncture. To ensure eight continuous injections per mouse, administrations were started in vein sections of the tail tip and then extended to the base of the tail. After GBCA administration, the puncture site was wiped with sterile gauze and bleeding was stopped by applying gentle pressure. The animals were monitored for acute adverse effects for at least 30 minutes after each GBCA application.

Gadopentetate is an ionic linear GBCA consisting of Gd^{3+} chelated with diethylenetriamine pentaacetic acid. Gadobutrol is a non-ionic complex of Gd^{3+} and the macrocyclic ligand dihydroxy-hydroxymethylpropyl-tetraazacyclododecane-triacetic acid (89). Due to its higher marketed concentration of 1.0 mmol/ml (157.25 mg Gd/ml) compared to gadopentetate (0.5 mmol/ml; 78.63 mg Gd/ml), gadobutrol was diluted in NaCl 1:2 prior to i.v. injection. This way, the weight-adapted injection volume was the same for both compounds and didn’t exceed 100 µl per single dosage per mouse.

Choosing a combination of cross-sectional and longitudinal study design enabled the repeated acquisition of MRI data from individual animals over time (longitudinal; maximum of 4 scans/mouse), and additionally allowed for histological and mass spectrometric assessment of brain tissues of animals sacrificed at the respective MRI time points post-final injection (p.f.i.) of GBCAs (cross-sectional, n=4-5/time point p.f.i.). The schematic study design is depicted in Figure 4. Cranial 7-Tesla MRI scans were acquired prior to GBCA injections (baseline, day 12/13 post-immunization) and 1, 10, and 40 days p.f.i. of GBCAs (day 23/24, 33/34 and 63/64 post-immunization). An interval of 24h between the last GBCA injection and the first MRI scan p.f.i. was carefully complied with. At every time point of sacrifice - after successful MRI acquisition – 4 to 5 mice per treatment group were removed from the experiment. Further assessment of Gd retention using (LA-)ICP-MS was done in cerebellar tissue and blood samples of 2 mice/group.

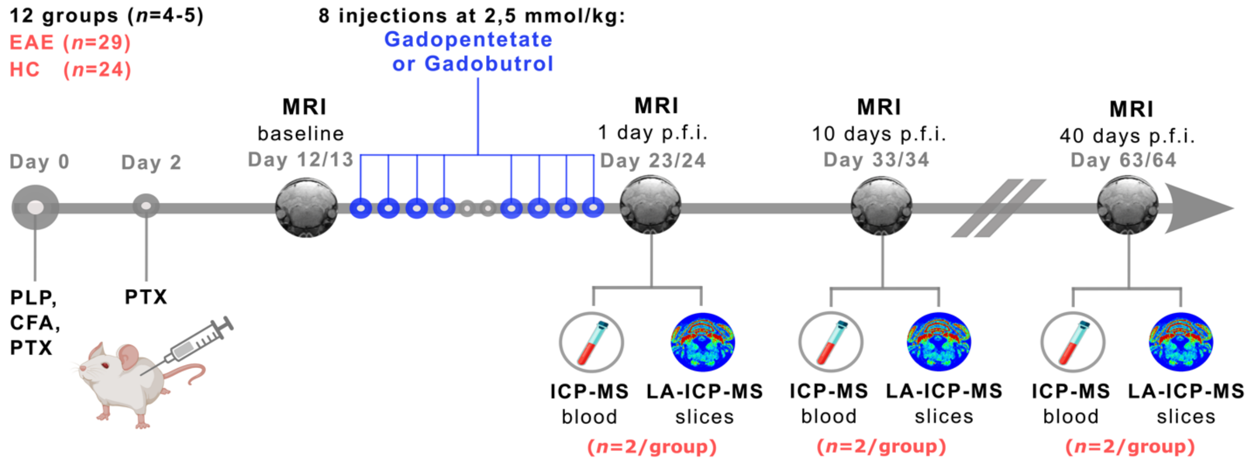

Figure 4: Experimental setup for assessment of Gd retention *in vivo*. When EAE mice reached maximal clinical disability (days 12 to 13 post-immunization), HC and EAE mice underwent a baseline brain MRI followed by eight i.v. injections of gadopentetate or gadobutrol over a period of 10 days, respectively (single dose: 2.5 mmol/kg BW, cumulative dose: 20 mmol/kg BW, two-day pause in between). On days 1, 10, and 40 p.f.i., further MRI brain scans of HC and EAE mice were acquired. 4-5 animals/group were sacrificed after each MRI session p.f.i of GBCAs. Blood was collected and brains were processed for the assessment of Gd retention using (LA-)ICP-MS (*n*=2/group). *(Modified from Anderhalten et al., 2022 (81) with kind permission by Wolters Kluwer Health, Inc.)*

2.3 7 Tesla MRI *in vivo*

All MRI scans were acquired by L. Anderhalten. MR image analysis was conducted in collaboration with S. Mueller.

MRI, compared to conventional X-ray and computer tomography, does not require the use of any harmful ionizing radiation and is based exclusively on the interaction of a magnetic field and radio frequency (RF) pulses (90). It is a medical imaging method founded upon the physical phenomenon of nuclear magnetic resonance (NMR). NMR was first demonstrated by F. Bloch and E. Purcell in 1945 and is based on the principle that certain atomic nuclei absorb and emit energy in the radiofrequency range of the electromagnetic spectrum when placed in a constant external magnetic field (B0) (91, 92). The MRI used in clinical diagnostics is based on the fact that the human body consists of around 70% water, which contains hydrogen nuclei (^1H). These nuclei have a property called nuclear spin, which generates a local magnetic field around each proton with poles aligning along its rotational axis similar to a bar magnet (93, 94). Figure 5 explains the basic MRI principle.

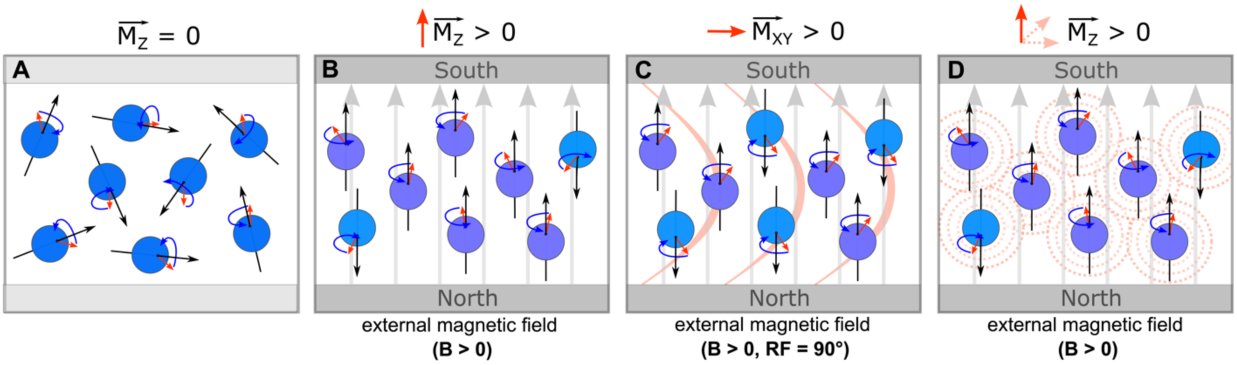

Figure 5: **Schematic illustration of the MRI principle. A** With no external magnetic field applied, nuclei align randomly, magnetic moments cancel each other out, and the longitudinal net magnetization vector (M_Z) is zero. **B** The application of an external magnetic field causes a parallel (low-energy state) or antiparallel (high-energy state) alignment of protons to the field in favor of the parallel-orientated protons. The imbalance in energy levels gives rise to a small increase in M_Z. **C** Perpendicular RF pulses matching the proton's Larmor frequency excite the protons and synchronize their precession, creating a transverse magnetization (M_{XY}) orthogonal to B0. **D** When the RF pulse is switched off, protons return to their thermal equilibrium configuration ($M_Z>0$), undergoing transverse and longitudinal relaxation. The energy emitted creates an NMR signal, which is spatially encoded using magnetic field gradients for 3D image reconstruction. T_1 and T_2 properties are encoded in the pixel intensity of an MRI image. (*own representation, information derived from Grover et al., 2015 & Minhas et al., 2022 (93, 94).)*

In MRI, T_1 and T_2 relaxation describe the decay of magnetic signals from ^1H in tissues. T_1 relaxation refers to the time it takes for the protons to return to their original longitudinal orientation after the RF pulse is switched off and is related to ^1H density and the surrounding tissue microstructure. T_2 relaxation refers to the decay of transverse magnetization due to proton spin dephasing, mainly related to water diffusion and tissue molecular motion. In conventional weighted MRI, T_1 and T_2 properties are encoded in the signal intensity of an MRI image and are used to characterize tissue types and pathological tissue alterations. T_1 is defined as the time (in ms) after which 63% of the original longitudinal magnetization has recovered, while T_2 is defined as the time (in ms) at which the transverse magnetization has decreased by 63%. In T_1-weighted MRI images, tissues with longer T_1 values, such as the cerebrospinal fluid (CSF), produce a weaker signal compared to tissues with shorter T_1 values, such as white matter. As a result, the CSF appears black, while the white matter appears white. In T_2-weighted MRI images, the situation is reversed. Here, the CSF appears lighter due to its long T_2 value, while the brain parenchyma appears darker due to its short T_2 value compared to the CSF (93-95). Aside from that, MRI can distinguish between white and grey matter, facilitating the diagnosis and monitoring of vascular, neoplastic, infectious, neurodegenerative, and neuroinflammatory diseases of the CNS.

There is a large number of MRI sequences that use a variety of techniques to visualize different tissue properties. The spin-echo sequence is a basic MRI sequence and always consists of a 90° pulse and at least one 180° pulse. Furthermore, varying the time between two RF pulses (TR = repetition time) and the time between the RF pulse and the signal reception (TE = echo time) influences T_1 relaxation. A short TR results in incomplete recovery of longitudinal magnetization in tissues with high water content before the next RF pulse is delivered. This will result in T_1 differences between tissues, which can be displayed as SI differences in the T_1-weighted image (94, 95).

GBCAs are used in contrast-enhanced MRI due to their ability to improve the distinguishability of body structures. The arrangement of the seven unpaired electrons in the outermost shell of the Gd atom leads to the formation of a strong local magnetic moment that interacts with the magnetic field inside the MRI scanner. This interaction leads to an increase in the relaxation rate of surrounding ^1H protons, thus a shortening of the T_1 and T_2 relaxation time. This results in an indirect focal signal enhancement in conventional $T_{1/2}$-weighted images. However, at approved clinical GBCA doses the T_1 effect generally predominates (2, 95).

Rather than relying on the effect of T_1 and T_2 on tissue contrasts in the conventional weighted image, relaxation times can be quantified using advanced MRI relaxometry (96). Relaxometry includes various quantitative MRI techniques that measure relaxation variables such as absolute T_1 and T_2. In T_1 relaxometry, also known as T_1 mapping, the absolute T_1 time of a given tissue is calculated and plotted on a quantitative parametric map displaying voxel-based numerical values (96). T_1 maps can be acquired using inversion recovery or saturation recovery techniques. Multiple images are acquired rapidly to measure T_1 along the relaxation curve and the absolute T_1 value is calculated in a fitting model (97). The saturation recovery sequence performed in this study is called “rapid acquisition with relaxation enhancement at variable TR” (RARE-VTR), where TR is varied to sample the longitudinal magnetization recovery.

The common MRI scanners in clinical practice apply field strengths of 1.5 or 3.0 Tesla. Contrary to that, small animal scanners in preclinical MRI operate at higher field strengths in a range of 4.7 to 11.7 Tesla, of which 7 Tesla magnets are the ones most commonly used (98). The benefits of employing scanners with higher field strength include improved signal-to-noise ratio (SNR), higher spatial resolution, and improved quantification capabilities. The total measurement time can be reduced at the expense of improved SNR. Disadvantages include increased image artifacts and magnetic field instability (93, 98). The use of preclinical imaging techniques in rodent models of CNS diseases offers great potential for monitoring disease progression and assessing underlying histopathological processes in brain tissue, providing important information transferable to clinical practice (99). The lack of invasiveness of MRI allows for the repeated longitudinal evaluation of individual disease activity and Gd retention patterns in a reduced number of animals (100, 101).

In this study, coronal whole-brain MR images were obtained on a 7 Tesla small-animal scanner (Bruker PharmaScan, Ettlingen, Germany) at baseline (day 12/13) and three consecutive time points p.f.i. of linear gadopentetate or macrocyclic gadobutrol as described above. Scans were acquired utilizing a 72 mm linear volume coil for excitation (RAPID Biomedical GmbH, Rimpar, Germany) in conjunction with a head surface coil (Bruker, Ettlingen, Germany), running ParaVision 5.1 software. A 2-dimensional T_1-weighted, a T_2-weighted, and a T_1map-RARE-VTR sequence were acquired. All MRI sequence parameters are detailed in Table 2. During image acquisition, EAE and HC mice were continuously anesthetized (1.0% to 1.5% isoflurane in 30% O_2 and 70% N_2O). Artifacts from breathing and movement were minimized by fixation of the mouse head to the surface coil. A pressure-sensitive pad was placed on the chest to monitor respiration and the depth of anesthesia was adjusted with isoflurane if needed. Constant body temperature was maintained by placing a heating device underneath the mouse’s body.

The analysis of cerebellar Gd retention was principally done using the T_1map-RARE-VTR sequence, extracting absolute T_1 relaxation times. MRI analysis was performed by blinded registration of MRI data to the Allen mouse brain atlas (ABA), a published standard mouse brain atlas. The registration was done utilizing the in-house developed MATLAB toolbox ANTx (Atlas Normalization Toolbox using Elastix; https://github.com/ChariteExpMri/antx2) (102). Structures of individual MR images were matched with single ABA structures using back-transformed atlas masks and region-specific T_1 relaxation times were determined. For animals that exhibited ventricular enlargement due to neuroinflammation (103), adjustments were made to the atlas transformation by subtracting individual ventricle masks, segmented on T_2-weighted images, using Analyze 10.0 software (AnalyzeDirect, Inc., USA). To record how T_1 values (in ms) differed between baseline MRI and MRI at the respective day p.f.i. of GBCAs, the T_1 relaxation time change (%) was calculated (T_1 change = ($T_{\mathbf{1}(\text{p.i.of GBCA})}$ – $T_{\mathbf{1}(\text{baseline})}$)/$T_{\mathbf{1}(\text{baseline})}$*100).

Table 2: Parameters of 2-dimensional MRI sequences

MRI parameters [unit]	**T_1-weighted RARE**	**T_2-weighted RARE**	**T_1map RARE-VTR**
echo time [ms]	11.5	36	9.83
repetition time [ms]	975	4200	8 TRs (255 to 7000)
rare factor	2	8	2
number of average	4	4	/
field of view [mm^2]	19.2	19.2	19.2
matrix	192x192	192x192	128x128
number of slices	32	32	10
slice thickness [mm]	0.5	0.5	1.0
scan time [min:s]	6:14	5:20	17:13

Note: total scan time per animal: 28 min 47 sec; RARE= rapid acquisition with relaxation enhance-ment, TR= repetition time, VTR= variable repetition time. *(MRI parameters for the T_1map RARE-VTR sequence are derived from the study by Anderhalten et al., 2022 (81), while parameters for T_1- and T_2-weighted RARE sequences were not published yet.)*

2.4 Sacrifice of mice and preparation of brain and blood samples

L. Anderhalten sacrificed all mice and prepared blood samples and brain tissue slices.

Animals were sacrificed under deep anesthesia with 1ml of a Xylazin/Ketamine mixture (20 mg/ml Xylazin, 50 mg/ml Ketamine in 0,9 % NaCl) when their interdigital reflex had ceased, which was checked several times with tweezers. Mice were then sternotomized with small scissors and blood was collected from the mouse chest after transection of the inferior vena cava. Blood samples were enriched with ethylenediaminetetraacetic acid (EDTA, 1,5 mmol/ml) and frozen at -80°C. Subsequently, mice were transcardially perfused with 40-50 ml phosphate-buffered saline (PBS) at a steady speed of 40 rpm using a peristaltic pump (U/min; Ismatec ISM444B-115V Analog Peristaltic Pump). A 21-gauge needle (Sterican cannula, 0.80 x 40 mm, B. Braun Melsungen AG, Germany) was attached to the efferent tube of the pump and gently inserted into the left ventricle. The aim of perfusion was to rid the mouse body of intravascular blood to prevent later signal artifacts caused by blood-containing elements such as Fe and phosphorus (P). Brains were extracted and fixed in 4% paraformaldehyde (PFA) at 4 °C for 24h, subsequently undergoing a 48h dehydration procedure in 30% sucrose. Thereafter, brains were embedded in Tissue Tek O.C.T. Compound (Sakura Finetek, USA) and frozen in 2-methyl butane at -70 to -80 °C. For further histological assessment and analysis of elemental distribution by LA-ICP-MS, brains were coronally cut into 10 µm-thick cryosections and stored at -80 °C.

2.5 Hematoxylin and eosin staining

The H&E staining was performed by L. Anderhalten.

The hematoxylin and eosin (H&E) staining is a common routine staining method used to differentiate tissue types and identify pathological changes in tissue morphology. Hematoxylin is a natural dye and stains all basophilic structures blue, e.g. DNA, nuclei, and ribosomes. Contrary to that, eosin is a synthetic dye staining acidophilic structures pink, e.g. proteins, mitochondria, cytoplasm, and extracellular matrix components (104). H&E staining was performed on consecutive cerebellar sections of those ablated using LA-ICP-MS for the localization of cerebellar ROIs and assessment of inflammation within EAE brains. 10 µm-thick coronal cryosections of EAE and HC cerebellum were thawed and dried at room temperature for 30 min. After a 10 min incubation phase with 4% PFA, slides were rinsed with distilled water and subsequently submerged in hematoxylin solution for 10 min. This was followed by two short washing steps in running tap water and distilled water. Slides were then immersed in eosin solution for 45 seconds, washed with tap water, and incubated in an ascending ethanol series for dehydration of the tissue (70, 80, 95, and 100 % ethanol; 5 min each). Subsequently, slides were transferred to Neo-Clear solution for 20 min and mounted in Neo-mount (Merck, Darmstadt, Germany) using glass coverslips. Image acquisition was performed on a Keyence Fluorescence Microscope (BZ-X800, Germany) using the bright field mode at 2x and 10x magnification.

2.6 Inductively coupled plasma mass spectrometry

ICP-MS measurements were carried out by J. Saatz and H. Traub. Sample preparation and subsequent analysis were performed by L. Anderhalten.

Inductively coupled plasma mass spectrometry (ICP-MS) is an analytical technique used for multi-element detection of isotope abundance ratios and trace element concentrations with high sensitivity and accuracy. The ability to quantify multiple elements and isotopes over a range of ten orders of magnitude makes ICP-MS an excellent method to measure various analytes (105). Metals and also some non-metals like P and sulfur (S) can be assessed in clinical samples, metal-containing biomolecules, nanomaterials, synthetic drugs, and many others (106). It has evolved into a tool for the determination of toxic element effects and monitoring of environmental, occupational, or medical exposure (107). ICP-MS is also a suitable method for Gd quantification in human body tissues like the bones (108, 109), brain (29-31, 33, 110), and blood (27) and has been applied in various rodent studies as a valuable tool for Gd detection (25, 27, 42, 45, 49, 51, 80, 111). Solid samples such as body tissues have to be digested and diluted before ICP-MS measurement.

ICP-MS employs the interplay of strong magnetic fields (generated by RF passing through a copper coil) with the tangential flow of a carrier gas, typically argon, flowing through a concentric quartz torch (Figure 6). This sustains a hot plasma that vaporizes and atomizes samples, generating element cations. The plasma is maintained by a large supply of argon and produces high ion yields, resulting in high sensitivity. Following ionization, the ions are transferred through a vacuum sampling interface into the mass spectrometer and guided by a set of ion lenses in direction of the mass separation device. Here, neutral particles and light are eliminated before the ion beam passes through a mass analyzer that isolates specific isotopes based on their mass-to-charge ratios for subsequent detection (106). Diverse types of mass analyzers exist, relying on distinct principles to achieve mass separation: quadruple mass filters, magnetic sector-field (SF) systems, and time-of-flight analyzers. The high sensitivity and mass resolution of an SF mass spectrometer, like the one used in this study, allows for precise quantification of low concentrations, independent of the nature of sample matrix composition, and for the determination of precise isotope ratios (112).

In our study, blood samples were assessed for Gd content (µg/g blood) using ICP-MS (*n*=2/group and time point of sacrifice) to evaluate if the clearance of Gd from the blood of GBCA-treated animals was effective. Prior to ICP-MS measurements, blood samples were thawed and digested for cell disruption. First, 100 mg of each blood sample was incubated overnight with 0.5 ml sub-boiled nitric acid (65% HNO_3). Utilizing a high-pressure asher (HPA-S, Anton Paar GmbH, Graz, Austria), blood samples were then decomposed at 300 °C and 100 bar in quartz vessels for 3h. After digestion, samples were diluted to a volume of 5 ml in MilliQ water. Element standard solutions were used for the preparation of calibration standards for the ICP-MS analysis. Blood samples from an untreated age- and sex-matched mouse served as a negative control.

Further, chronic hippocampal slices were assessed for Gd content after 48h incubation with gadopentetate or gadobutrol at 10 or 50 mM +/- TNFα respectively (according to the protocol described in section 2.11). Untreated chronic slices served as negative controls. After treatment, membranes were transferred to fresh culture medium and then fixed in 4% PFA for 1h to enable slice removal from the membranes of cell culture inserts with a brush. No further washing steps were conducted. 18 to 20 isolated tissue slices were pooled per condition, yielding 2.52 ± 0.19 mg each, and further digested overnight in 0.5 ml pure sub-boiled HNO_3 and 25 µl of ultrapure hydrogen peroxide. For complete digestion, samples were heated to 95° C using a thermomixer (Eppendorf) for 2 hours. Digested solutions were filtered and diluted to a volume of 15 ml in MilliQ water. An external calibration with lutetium (Lu) as an internal standard was carried out for quantification. For this purpose, 10 ng/g Lu was added to the calibration standards and samples to correct the instrumental drift during the series of measurements. The blank correction was made with acid blanks (HNO_3 + hydrogen peroxide). The limit of quantification for Gd was 0.16 ng/g.

Measurements were acquired using an Element 2 ICP SF mass spectrometer (Thermo Fisher Scientific, Bremen, Germany). Instrumental parameters of the ICP-MS system for Gd detection in blood samples and chronic hippocampal slices are displayed in Table 3.

Table 3: Instrumental parameters of the ICP-MS system

ICP-MS parameters [unit]	**Blood samples**	**Chronic hippocampal slices**
RF plasma power [W]	1250	1250
Plasma gas flow (Ar) [L min^{-1}]	16	16
Sample gas flow (Ar) [L min^{-1}]	1.215	1.180
Auxiliary gas flow (Ar) [L min^{-1}]	1.05	0.95
Mass resolution ($m/\Delta m$)	4000 (MR)	4000 (MR)
Detected isotopes	^{55}Mn, ^{115}In (internal standard), ^{155}Gd, ^{156}Gd, ^{157}Gd, ^{158}Gd ,^{160}Gd	^{158}Gd ,^{160}Gd, ^{175}Lu (internal standard), (additionally ^{153}Eu)

Note: MR= medium resolution, ^{55}Mn= manganese, ^{175}Lu= lutetium, ^{153}Eu= europium. *(The ICP-MS parameters for blood samples are derived from the study by Anderhalten et al., 2022 (81), while those for hippocampal slices were not published yet.)*

2.7 Laser ablation inductively coupled plasma mass spectrometry

LA-ICP-MS measurements were conducted in collaboration with J. Saatz and H. Traub. Sample preparation and consequent analysis were done by L. Anderhalten.

Laser ablation inductively coupled plasma mass spectrometry (LA-ICP-MS) is a widely used technique for analyzing elements and isotopes with high sensitivity and spatial resolution in the micrometer range (112). It allows direct analysis of biological samples and solid materials with minimal preparation. LA-ICP-MS is capable of quantifying elemental distributions, which is one of its key features and has recently been used to determine the distribution of retained Gd in tissue samples of human (33, 113) and rodent brains (25, 26, 28, 114). The laser ablation process involves a focused laser beam that ablates material from the tissue sample surface and transports it to the ICP source (115) (as illustrated in Figure 6). Typically, the inert gas helium is used as an aerosol carrier. The measured SIs of the ions can be calibrated and translated into concentrations per pixel (115). Calibration and standardization are important for precise detection, and usually involve the compensation of signal drifts during long ablation times and the preparation of matrix-matched standards for external calibration (106).

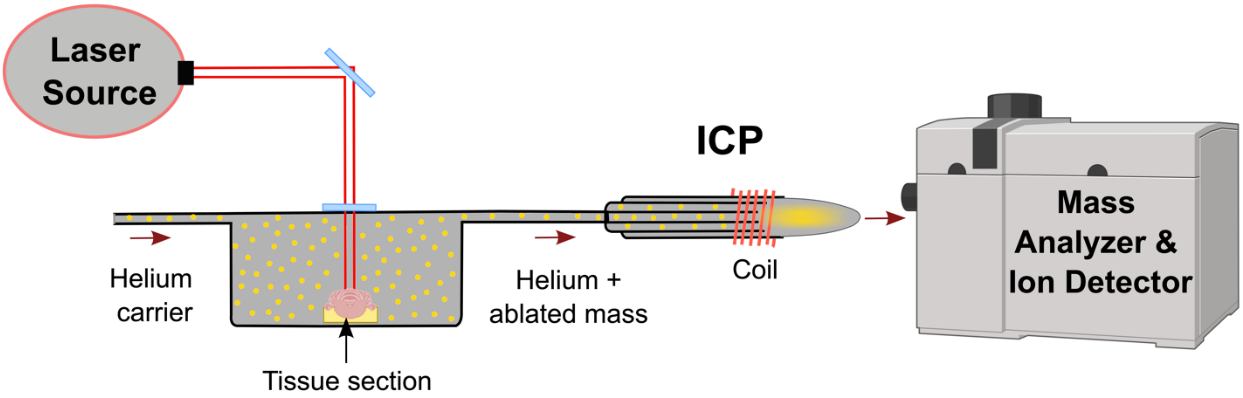

Figure 6: Schematic illustration of the LA-ICP-MS system with helium gas as aerosol carrier *(own representation)*

We aimed to depict the distribution of Gd within 10 µm-thick cryosections of inflamed and non-inflamed cerebellum and to identify other endogenous (non-)metals that may be affected by inflammation and Gd deposition. LA-ICP-MS analysis was carried out on a commercial LA system equipped with an Nd:YAG laser at 213 nm and a two-volume sample chamber (NWR-213, ESI, Bozeman, MT, USA). Coupled with this was a SF ICP-MS (Element XR, Thermo Fisher Scientific, Bremen, Germany), which was tuned daily for signal stability (relative standard deviation; RSD < 5 %), oxide ratio (ThO/Th < 1 %), and maximum ion intensity using a glass slide. The laser energy was fine-tuned to ensure the complete ablation of the tissue section with each laser shot, while preserving the integrity of neighboring regions. Instrumental parameters of the ICP-MS- and LA-system are specified below (Table 4).

LA-ICP-MS data was visualized using Origin 2018 software (OriginLab Corporation, Northampton, MA). The calibration was performed by measuring agarose gel standards spiked with distinct amounts of analytes cast on glass slides (Roth, Karlsruhe, Germany; analyte contents 0-310 fg/pixel) (116). Ten different isotopes (see Table 4) were detected as counts per second (CPS). Calibration of the isotopes ^{66}Zn and ^{158}Gd was accomplished by translation of the measured intensity (in CPS) for each pixel into fg/pixel. In a semi-quantitative approach, ^{66}Zn and ^{158}Gd levels (fg/pixel) were converted into molar values (µM) with one volumetric pixel corresponding to a brain volume of 80 µm x 22 µm x 10 µm (1.76 x 10^{-11} l). Due to the high ^{57}Fe content in the agarose used for the preparation of the calibration standards, no suitable standards could be prepared for ^{57}Fe in a relevant concentration range. However, measured ^{57}Fe intensities are proportional to the ^{57}Fe content in the samples, and drift correction allows brain sections to be compared to each other. The analysis of ^{66}Zn and ^{158}Gd concentrations as well as ^{57}Fe intensities was performed manually on calibrated LA-ICP-MS images using ImageJ software (117). Regions of interest (ROIs) were the CN, DN, and the whole cerebellar slice (mean). Element concentrations were obtained by measuring each ROI three times in an independent and randomized manner - to increase the reliability of results – and taking the average of resulting values.

Table 4: Instrumental parameters of the LA-ICP-MS system

ICP-MS parameters [unit]		**LA-system parameters** [unit]	
RF plasma power [W]	1350	Wavelength [nm]	213
Plasma gas flow (Ar) [L min^{-1}]	16	Helium gas flow [L min^{-1}]	1
Sample gas flow (Ar) [L min^{-1}]	0.660	Laser energy [J cm^{-2}]	1.9
Auxiliary gas flow (Ar) [L min^{-1}]	1.05	Laser spot size [µm]	100
Mass resolution ($m/\Delta m$)	300 (LR)	Scan speed [µm s^{-1}]	100
Sample time [ms]	2	Repetition rate [Hz]	20
Scanning mode	Line by line	Line overlap [µm]	20
Detected isotopes	^{31}P, ^{34}S, ^{44}Ca, ^{55}Mn, ^{57}Fe,^{65}Cu, ^{66}Zn, ^{153}Eu,^{158}Gd, ^{160}Gd		

Note: LR= ow resolution, ^{34}S=sulfur, ^{55}Mn=manganese, ^{153}Eu=europium, other abbreviations on page 7. *(LA-ICP-MS parameters were in parts published by Anderhalten et al., 2022 (81). This table contains additional unpublished details.)*

2.8 MRI calibration in homogenized mouse brain tissue

MRI calibration and the following data analysis were conducted by L. Anderhalten.

We quantified to what actual extent the Gd levels assessed by LA-ICP-MS induce T_1 relaxation time shortening *in vitro* by performing MRI calibration using standards of gadopentetate and gadobutrol in homogenized mouse brain tissue. The paramagnetic efficacy of a GBCA to shorten T_1 is reflected by its T_1 relaxivity (r_1) (118). By comparing the calibrated T_1 values with T_1 measured in *in vivo* MRI for equal Gd concentrations, we aimed to identify any potential T_1 deviations and thereby elucidate potential interactions of Gd^{3+} with macromolecular or inorganic ligands within the brain tissue.

MRI calibration was conducted using brain tissue from eighteen 10-week-old female healthy SJL/J mice. Brains were isolated, flash-frozen in liquid nitrogen, and preserved at -80 °C. Thereafter, the brains were cryo-pulverized using the CP02 cryoPREP Automated Dry Pulverizer (Covaris Ltd, UK) and manually homogenized with 5 % fetal bovine serum (FBS). Either gadopentetate or gadobutrol was added to obtain

Gd concentrations from 20 to 100 µM (20, 40, 60, 80, 100 µM). For baseline acquisition, tissue samples without GBCA supplementation were prepared. Samples were transferred into 5 mm glass tubes for MRI and incubated for 30 minutes at 4 °C. Subsequently, the tubes were warmed up to body temperature (37 °C) and put into the dedicated phantom holder for NMR tubes. MRI scans were performed on a 7 T small-animal scanner (Bruker Biospec, Ettlingen, Germany), running ParaVision 6.1 software using an axial 2-dimensional T_1map RARE-VTR sequence (echo time = 9.83 ms, 8 TRs from 255 to 7000 ms, rare factor = 2, field of view = 26 mm^2, matrix = 128 x 128, number of slices = 3, slice thickness: 1 mm, scan time: 17 min and 13 s). For internal validation, MRI calibration was performed in water and FBS following the same protocol (119).

T_1 relaxation times were analyzed by applying rotund ROIs of standardized size to the center of each T_1map RARE-VTR image, and values from two consecutive MRI slices per condition were averaged. Thereafter, linear regression analysis was performed by graphing R_1 at different concentrations of gadopentetate and gadobutrol using the GraphPad Prism software (GraphPad, version 8.4.3, CA, USA). r_1 is reflected in the slope of R_1 regression lines (43, 119). We then calculated the relaxation rate '$R_1(\mathrm{GBCA}_{\mathrm{calibrated}})$' for both GBCAs from calibrated r_1 values and Gd concentrations obtained from LA-ICP-MS for the areas of CN, DN, and whole cerebellum ($R_1(GBCA_{\mathrm{calibrated}}) = r_1 \times C_{Gd} + R_1(0)$; $R_1 = 1/T_1$; C_{Gd} = Gd concentration; $R_1(0) = R_1$ *of baseline MRI*). Mean *in vivo* T_1 relaxation times were subtracted from calibrated T_1 relaxation times as reciprocal of R_1 ($\Delta T_1 = T_1(GBCA_{calibrated}) - T_1(GBCA_{in\ vivo})$). To investigate to what degree *in vivo* T_1 values deviated from calibrated values, the resulting difference ΔT_1 in relation to $T_1(\mathrm{GBCA}_{\mathrm{calibrated}})$ was further expressed as T_1 percentage deviation (displayed in Figure 13C).

2.9 Generation of organotypic hippocampal slice cultures

All steps to generate chronic brain slice cultures were carried out by L. Anderhalten.

The chronic murine organotypic hippocampal slice culture is an *ex vivo* model of brain tissue cultured on membranes for various periods. Chronic slice cultures offer advantages over other (e.g. single-cell) *in vitro* models, including the long-term viability of brain tissue under controlled conditions, the maintenance of *in vivo*-like three-dimensional tissue organization and the retention of synaptic function (120). This allows for the examination of treatment effects beyond a few hours and makes them a valuable tool to study cellular and molecular interactions of the hippocampus in a physiologically relevant context.

Prior to the generation of organotypic hippocampal slice cultures, all required equipment was autoclaved and additionally sterilized by UV-radiation for 30 min. SJL/J mouse pups (Janvier Labs, France) aged 7 to 10 days were sacrificed by decapitation with large scissors at the beginning of the experiment. The scalp was removed after skin disinfection with Ethanol 70% and the skull was placed in chilled cutting medium (MEM 1x with 1% L-Glutamine). Once transferred to the sterile bench, the skull was opened and both hippocampi were isolated and processed according to the steps specified in Figure 7. If necessary, hippocampal slices were examined under a light microscope before the membrane transfer (Millicell cell culture inserts, 0,4µm, MCHT06H48, Merck, Germany) to identify histologically intact exemplars. Well-preserved sections from a single pup were distributed across all membranes to achieve a randomization effect. The entire process of slice culture preparation never exceeded a time limit of 30 min. Slice cultures were natively incubated for 12-13 days at 37 °C and 5% CO2; the culture medium was changed every second day.

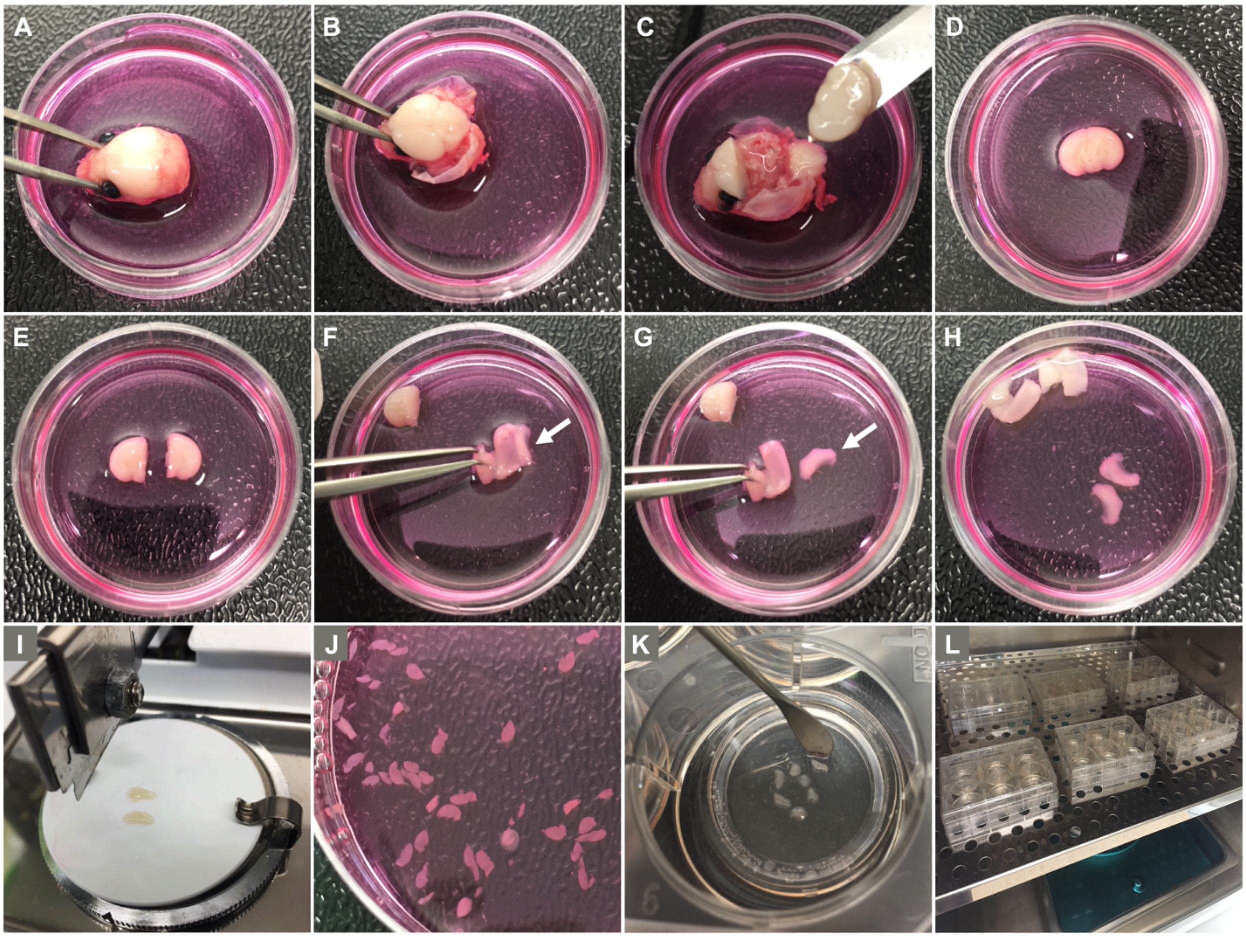

Figure 7: Sterile generation of hippocampal slice cultures. A Fixation of the mouse head with pointed forceps after skin removal**. B** Skullcap removal with scissors and spatula**. C** Coronal incision of the brain separating it into three parts (front: anterior part of cerebral cortex, cerebral nuclei; middle: dorsal part of

cerebral cortex, mesencephalon, diencephalon, hippocampus; back: cerebellum, pons, medulla). **D** Transfer of the middle part to sterile chilled cutting medium with cerebellar intersecting plane facing upward. **E** Sagittal separation of middle brain part with a sterile scalpel. **F+G** Fixation of mesencephalon with arcuate forceps; isolation of right hippocampus by gentle scooping movement with a spatula. White arrows indicate the hippocampus. **H** Isolation of left hippocampus. **I** Hippocampal transfer to cutting disc; slicing to 350µm-thick tissue slices (McIlwain Tissue Chopper). **J** Transfer of slices to chilled cutting medium. **K** Transfer of well-preserved slices to membrane inserts in 6-well plates. **L** Incubation at 37 °C with 5% CO_2. *(own representation)*

2.10 Establishment of optimal *ex vivo* culture conditions

All steps of the establishment of the ex vivo model were performed by L. Anderhalten.

Before being able to examine the potential cytotoxic effect of GBCAs on neuronal tissue, suitable culture conditions and media compositions were determined to ensure optimal long-term slice survival. During the first month of culture establishment, a slightly modified version of the medium by Gimsa *et al*. (121) was used, but slice survival was not satisfactory. Hence, several slice culture media published during the last years were compared (detailed compositions are displayed in Table 5). If ingredients contained in the published composition were only available in modified variants or from other manufacturers, the medium was referred to as ‘modified’ (Table 5). All media were sterilely filtrated before use (121-126). An assessment of the medium-dependent slice survival was done by visual inspection and calculation of the cell death rate within the dentate gyrus (DG) using propidium iodide (PI) staining and subsequent fluorescence microscopy (Keyence Fluorescence Microscope BZ-X800, Germany) (PI staining is explained in 2.11, image acquisition and analysis corresponds to the protocol detailed in the original publication (81)). The slices were considered viable when becoming transparent, flat, and well attached to the membrane, as described by Humpel (120). Dead tissue slices could be visually identified as they became white and swollen.

Repeated establishment experiments showed that a modified version of the Opitz-Araya medium (125) was best suited for the long-term culture of SJL/J hippocampi. Under these conditions, the hippocampal architecture was maintained for over two weeks and the neuronal survival in control slices was optimal. A stable cell death rate was established for the DG region in negative control slices (50 ng/ml of TNFα vs. no TNFα, 2.35 ± 3.75 % vs. 0.30 ± 0.35 %) and positive control slices treated with N-methyl-D-aspartic acid (NMDA, 50 µM) for 4 hours (34.02 ± 9.96 % vs. 20.59 ± 7.53 %) (see 2.11).

Table 5: Determination of suitable culture media

Name of culture medium	Ingredients	Starting conc.	Final conc.	Add for 50ml
Gimsa medium (modified) (121)	MEM	1 x	50 %	25 ml
	Horse serum heat inactivated	1 x	25 %	12.5 ml
	HBSS	1 x	25 %	12.5 ml
	$NaHCO_3$	890 mM	5.2 mM	292.1 µl
	Insulin-Transferrin-Selenium	100 x	0,1 x	50 µl
	Ascorbic acid	1 mg/ml	0.8 µg/ml	40 µl
	L-Glutamine	200 mM	2 %	1 ml
	Glucose	20 %	2.64 mg/ml	611.3 µl
	Pen/Strep	100 x	1 x	500 µl
Croft medium (modified) (122)	MEM	1 x	55.2 %	27.6 ml
	Horse serum heat inactivated	1 x	25 %	12.5 ml
	HEPES	1000 mM	26.6 mM	1.33 ml
	NaCl	1001 mM	19.3 mM	964 µl
	$NaHCO_3$	890 mM	5 mM	280.9 µl
	Ascorbic acid	5680 µM	511 µM	4.5 ml
	Glucose	1110 mM	40 mM	1.80 ml
	$CaCl_2$	1000 mM	2.7 mM	135 µl
	$MgSO_4$	1000 mM	2.5 mM	125 µl
	GlutaMAX	100 x	1 x	500 µl
	Insulin-Transferrin-Selenium	100 x	0.033 %	16.5 µl
	Pen/Strep	100 x	0.5 %	250 µl
Dionne medium (123)	Neurobasal Day 1:	1 x	85.6 %	42.8 ml
	Day 2+3:		90.6%	45.3 ml
	After Day 3:		95.6%	47.8 ml
	FBS Day 1:	1 x	10 %	5 ml
	Day 2+3:		5%	2.5 ml
	After Day 3:		0%	0 ml
	HEPES	1000 mM	10 mM	500 µl
	B-27	50 x	1 x	1 ml
	L-Glutamine	200 mM	0.4 mM	100 µl
	GlutaMAX	100 x	0.3 x	150 µl
	Pen/Strep	100 x	1 x	500 µl
Jang medium (serum-free) (124)	Neurobasal A	1 x	96 %	48 ml
	B-27	50 x	2 %	1 ml
	L-Glutamine	200 mM	2 mM	500 µl
	Pen/Strep	100 x	1 x	500 µl
Opitz-Araya medium (modified) (125)	MEM	1 x	73.8 %	36.9 ml
	Horse serum heat inactivated	1 x	20 %	10 ml
	HEPES buffer	1000 mM	30 mM	1.5 ml
	L-Glutamin	200 mM	1 mM	250 µl
	$CaCl_2$	1000 mM	1 mM	50 µl
	$MgSO_4$	1000 mM	2 mM	100 µl
	Insulin-Transferrin-Selenium	100 x	0.1 x	50 µl
	Ascorbic acid	25 %	0,004 %	2 µl
	Glucose	1110 mM	13 mM	586 µl
	$NaHCO_3$	890 mM	5.2 mM	292 µl
	Pen/Strep	100 x	0.5 %	250 µl
Wang medium (modified) (126)	MEM	1 x	50 %	25.0 ml
	HBSS	1 x	25 %	12.5 ml
	Horse Serum heat inactivated	1 x	25 %	12.5 ml
	HEPES buffer	1000 mM	13 mM	625 µl
	Pen/Strep	100 x	1 x	500 µl
	Glucose	1110 mM	35 mM	1.6 ml

(Note: Media ingredients and concentrations are based on references 121-126 cited in this thesis. Any modifications to the original medium due to e.g. ingredient availability are noted as 'modified'.)

2.11 *Ex vivo* assessment of the effects of GBCAs on neuronal viability

The assessment of GBCA effects on neuronal viability was conducted by L. Anderhalten.

On day 13, treatment with the inflammatory mediator TNF-alpha (TNFα at 50 ng/ml; mouse recombinant, lyophilized, Invitrogen, US) was initiated in one half of the slices. After 48h of inflammatory pre-conditioning with TNFα, the culture medium was changed on day 15 and TNFα was added again for another 48h. Furthermore, on day 15, GBCAs (either gadopentetate or gadobutrol) were added to the naive and TNFα-incubated cultures at 1 mM, 10 mM, or 50 mM, respectively, according to the schematic study design in Figure 8. To ensure substance penetration into the hippocampal tissue slices, 100 ml of substance-enriched culture medium was added to the top of each membrane. On day 16, NMDA at 50 µM was added as positive neurotoxicity control over a period of 4 h. It leads to neuronal damage due to the excitotoxic effect of excessive NMDA receptor activation (127). TNFα can potentiate neurotoxicity through the NMDA receptor by increasing extracellular glutamate levels via transporter inhibition (128). Treatment was terminated on day 17 after 48h incubation with GBCAs +/- TNFα and membranes were washed repeatedly in fresh culture medium.

For the assessment of GBCA-induced cell death, living slices were stained with PI at 10 µg/ml for 30 min at 37 °C. Thereafter slices were fixed in 4% PFA (1h), dehydrated in sucrose (30%, 2 days), and processed for cryosectioning. Frozen and embedded hippocampal slices were cut to a thickness of 20 µm, dried, and counterstained with 4′,6-Diamidin-2-phenylindol (DAPI) for identification of all cell nuclei (in addition to dead, PI-stained nuclei) using fluorescence microscopy (Keyence BZ-X800, Germany). Slice imaging using the BZ-X filters DAPI and TexasRed as well as the consequent image analysis are further detailed in the original publication (81). For IMC analysis of Gd content retained within hippocampal slices, 10 µm-thick cryosections were additionally prepared (Figure 8). The slice preparation required for Gd quantification using ICP-MS is detailed above (Methods, section 2.6).

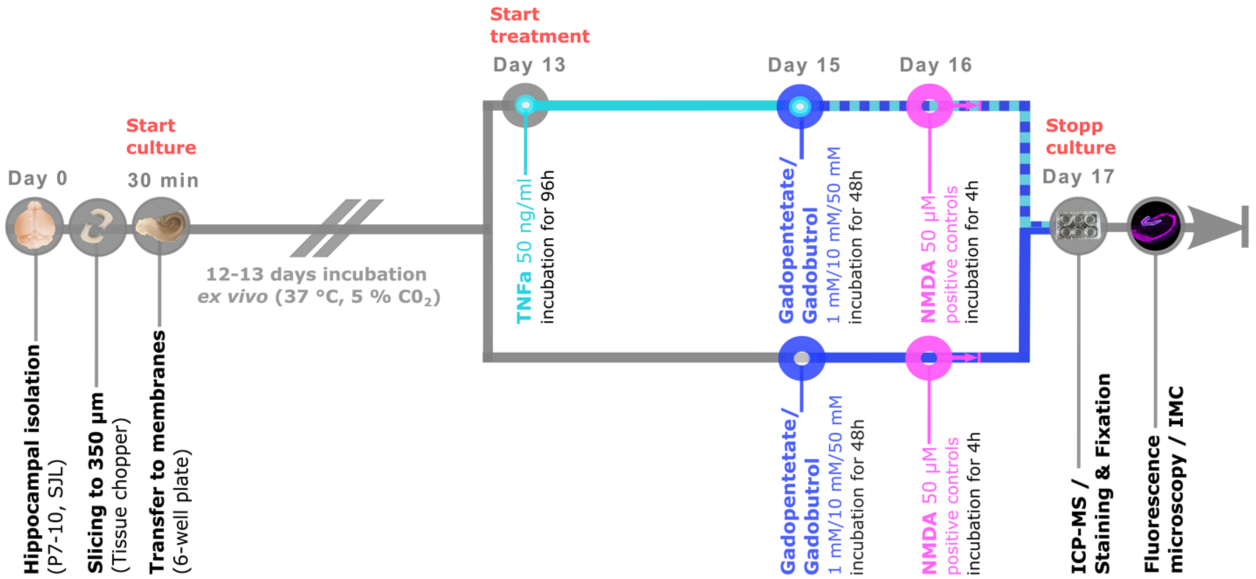

Figure 8: Experimental setup for assessment of Gd toxicity *ex vivo*. After slice preparation, chronic organotypic hippocampal cultures were natively incubated for 12 to 13 days. On day 13, one-half of the slices were treated with TNFα at 50 ng/ml (incubation time: 96 h). On day 15, incubation with GBCAs at 1, 10, or 50 mM was started (gadopentetate or gadobutrol for 48 h), while the treatment with TNFα was continued. In positive control slices only, incubation with NMDA for 4 h was executed on day 16. After the termination of the slice culture on day 17, living tissue slices were collected for the quantification of Gd retention by ICP-MS or stained with PI and fixed for the assessment of cell death by fluorescence microscopy. IMC was performed on fixed tissue slices to visualize the distribution of Gd retention. *(Modified from Anderhalten et al., 2022 (81) with kind permission by Wolters Kluwer Health, Inc.)*

2.12 Imaging mass cytometry

IMC images were acquired by D. Kunkel and Y. Rodriguez-Sillke. Slice preparation and subsequent image analysis were performed by L. Anderhalten.

Imaging mass cytometry (IMC) - the combination of an LA system with a low-dispersion sample chamber and a spatial resolution of 1 µm with ICP time-of-flight mass spectrometry - introduces a novel approach for conducting multiparametric tissue imaging at a single-cell level and beyond (129). IMC is a high-throughput technology that enables the simultaneous imaging and analysis of multiple molecular and cellular parameters in biological samples. The technique is based on the use of antibodies coupled to metal-chelating polymers carrying stable isotopes, primarily sourced from the lanthanide series. Thin tissue samples are stained with the conjugated antibodies on a glass slide using an immunohistochemical workflow, inserted into the ablation chamber, and scanned by a pulsed laser beam. Ablated particles are vaporized, atomized, finally ionized and analyzed based on their mass-to-charge ratio by ICP time-of-flight mass spectrometry. Metal isotopes linked to each spot of ablation are measured concurrently and correlated with the precise position of each individual spot. The resulting IMC image shows the ion count for each mass tag, indicating its abundance, and the gray-scale image provides anatomic information (129).

IMC can provide spatial information about the location of Gd accumulation sites within a brain sample. This may help to better understand the pathological processes visualized by Gd enhancement in MRI. In this study, however, IMC was performed to investigate whether the lack of GBCA-induced neurocytotoxicity at concentrations less than 50mM of gadopentetate was due to deficient or uneven penetration of the agents into the living tissue slices *ex vivo*. 10 µm-thick cryosections of hippocampal slices treated with 10 mM of gadopentetate or gadobutrol for 48h respectively were ablated; additional untreated hippocampal tissue served as a negative control.

Before tissue ablation, nucleic acids were labeled with Iridium-Cell-IDTM Intercalator according to the manufacturers' staining protocol for frozen sections (130) for the analysis of co-localization with elemental Gd. The imaging was done using a CyTOF2/Helios instrument coupled with a Hyperion Tissue Imager (Fluidigm, Canada), with the assistance of CyTOF software (version 7.0.8493). Calibration was performed as instructed by the manufacturer, and the laser power was fine-tuned for every sample to guarantee complete ablation of the slices. The ablation was conducted at a resolution of 1 µm and a frequency of 200 Hz, spanning a mass range of 75 to 209 Dalton. The Gd ion count was obtained for the DG region using the MCD Viewer software by applying 6 ROIs per DG (100 x100 µm). The resulting mean ion counts of two slices per treatment group were averaged, determining the retained Gd content in a semi-quantitative manner.

2.13 Statistical analysis

The statistical data analysis was done by L. Anderhalten and confirmed by the Institute of Biometry and Clinical Epidemiology at Charité – Universitätsmedizin Berlin.

Data analysis was performed using the Prism software (GraphPad, CA, USA; version 8.4.3). Data were tested for normal distribution by graphical evaluation in histograms and normality tests (Shapiro-Wilk test, D'Agostino & Pearson test, and Anderson-Darling test). Concerning every assessed variable, some subgroups failed to pass the normality assessment. Hence, data were analyzed by applying non-parametric tests. All data were expressed as geometric means ± standard deviations. P values < 0.05 indicated statistical significance with * implying $p < 0.05$, ** implying $p < 0.01$, *** implying $p < 0.001$, and **** implying $p < 0.0001$. No formal hypothesis testing was originally planned because the study of this thesis was intended as an exploratory pilot study.

To verify that retained Gd concentrations and neurotoxicity are promoted during neuroinflammation, data from inflammatory conditions (EAE animals *in vivo*, TNFα incubated slices *ex vivo*) was compared to naive control conditions (HC animals *in vivo*, naive slices *ex vivo*). Two group comparisons were carried out applying the Mann-Whitney U test; comparisons between more than two groups were performed using the Kruskal-Wallis test followed by Dunn's post hoc test for multiple rank comparisons. Non-parametrical correlations were accomplished using the Spearman rank correlation.

The central statistical aim was to quantify the degree of inflammation-promoted Gd retention by addressing T_1 time shortening in MRI *in vivo*. Hence, comparing MRI measures of EAE and HC mice, the Bonferroni correction was applied for multiple testing over three to four consecutive time points. In contrast, LA-ICP-MS, ICP-MS, and MRI calibration data as well as data obtained from the *ex vivo* trial were expressed in a descriptive way and no correction was performed. In addition, low sample sizes (LA-ICP-MS, ICP-MS, MRI calibration: *n*=2/group) did not allow any quantitative analyses. The aim here was to uncover any stochastic dominance and thus any effect of neuroinflammation. P-values should therefore be evaluated rather descriptively.

3 Essential Results

Partial results of this work were published in the study by Anderhalten et al. (81).

3.1 Clinical and histological signs of EAE

EAE mice (*n*=29) developed the first disease-related symptoms on days 8 to 10 post-immunization (Figure 9A). On days 12 to 13, they reached the peak of disease, showing maximal clinical disability (2.00 ± 0.51; mean EAE score on day 12). EAE mice further presented a relapsing-remitting course of disease until the end of the experiment on day 64 (Figure 9A). Comparing gadopentetate- and gadobutrol-treated EAE mice, no significant differences in EAE-score were detectable between mice sacrificed at day 1, 10, and 40 p.f.i. of GBCAs (Kruskal-Wallis test; *n*=4-5/group; p=0,7509).

The qualitative histological examination of H&E-stained cerebellar tissue was performed on consecutive cryosections of those used for the assessment of Gd retention by LA-ICP-MS. Bright field microscopy revealed typical lesions in EAE brains with sites of predilection in periventricular and cortical areas of the cerebellum as well as meningeal mononuclear infiltration (Figure 9B). In HC brains, no infiltration of mononuclear cells was detectable in any of the assessed cerebellar H&E-stained sections.

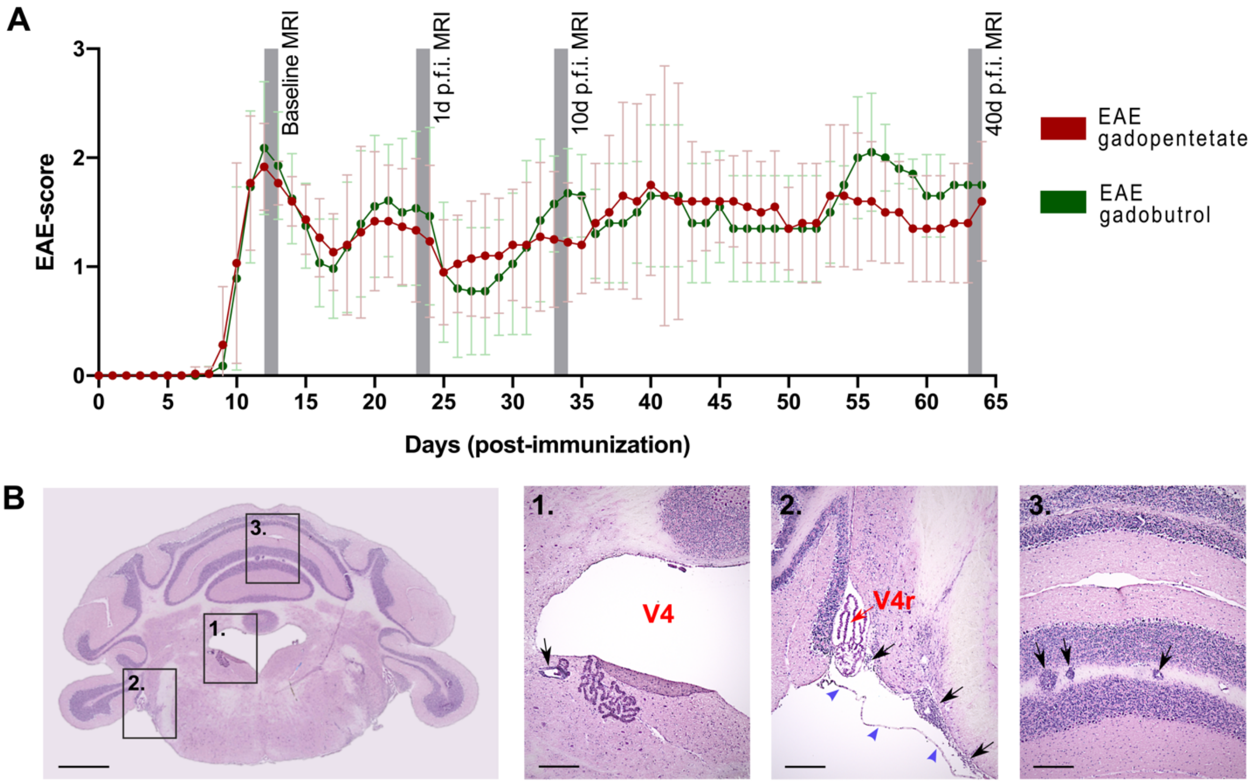

Figure 9: Clinical and histological assessment of EAE-related properties. A Demonstration of the EAE-score of EAE mice included in this study (red: gadopentetate-treated, green: gadobutrol-treated). **B**

Bright field image of H&E stained section of EAE cerebellum at 2x magnification, stitched (gadobutrol-treated, EAE-score: 1.5); at 10x: 1. section: periventricular EAE lesion with perivascular accumulation of mononuclear cells; 2. section: large meningeal infiltration of mononuclear cells; 3. section: three EAE lesions within a white matter convolution of the cerebellar cortex. Scale bars at 2x magnification: 1 mm, at 10x: 200 µm. V4= fourth ventricle; V4r= lateral recess of V4, additionally marked with red arrow. Black arrows indicate mononuclear cell infiltration. Blue arrowheads indicate meninges. *(Figure 9A is derived from Anderhalten et al., 2022 (81); Figure 9B: own representation.)*

3.2 T_1 relaxometry detects enhanced T_1 time shortening in EAE brains

The presentation of the following MRI and LA-ICP-MS results focuses in particular on the CN as a predilection site for Gd retention and on its long-term character, hence on day 40 p.f.i. of both tested GBCAs.

Among other cerebellar brain areas, T_1 relaxometry identified the CN as particular ROI, demonstrating relevant focal T_1 shortening after GBCA administration. The CN region is highlighted in Figure 10A. An initial qualitative assessment of cerebellar T_1maps of EAE and HC mice revealed obvious T_1 shortening, particularly within the CN, at day 1, 10, and 40 p.f.i. of gadopentetate compared to baseline scans. After gadobutrol injections, no qualitative differences between baseline scan and MRI p.f.i. were observed (Figure 10B).

The quantitative analysis of absolute T_1 relaxation times of the CN revealed that EAE mice generally demonstrated higher T_1 values compared to HC mice at baseline MRI (EAE vs. HC; pre gadopentetate, 2032.83 ± 142.27 ms vs. 1955.54 ± 94.50 ms; pre gadobutrol, 2024.69 ± 122.09 ms vs. 1964.52 ± 129.20 ms) (Figure 10C). Contrary to that, 24 h after the administration of both GBCAs, there was a strong trend for shorter T_1 times in EAE compared to HC mice (Figure 10C). After gadopentetate application, the trend for lower absolute T_1 values in the inflamed CN persisted over the observation period (EAE vs. HC; day 40 p.f.i. of gadopentetate, 1757.03 ± 96.04 ms vs. 1864.82 ± 84.14 ms), while it dissolved toward day 40 p.f.i. of gadobutrol (EAE vs. HC, 1920.10 ± 73.29 ms vs. 1881 ± 53.06 ms). Application of the Bonferroni correction over four consecutive time points for both GBCAs, respectively, revealed that observed differences in T_1 values between EAE and HC CN were not significant at any of the assessed time points (Figure 10C; data was not published yet). Furthermore, no statistically relevant correlations were found between EAE-score and absolute T_1 at baseline or MRI time points p.f.i. of both GBCAs, respectively (data is not shown).

The T_1 relaxation time change (in %) was calculated to analyze the shortening effect of GBCAs on T_1 relaxation comparing EAE and HC brains (Figure 10D). After the administration of gadopentetate, the decrease in T_1 was significantly stronger in EAE CN compared to HC. This difference remained significant until day 40 p.f.i. after Bonferroni correction (EAE vs. HC, -13.69 ± 4.53 % vs. -2.64 ± 4.31 %; p=0.0477). In contrast to this, after gadobutrol administration, initially significant differences in T_1 change between EAE and HC mice diminished toward day 40 p.f.i. (EAE vs. HC, -1.93 ± 3.96 % vs. -0.33 ± 2.89 %), indicating a continuous clearance of gadobutrol from the CNS (Figure 10D).

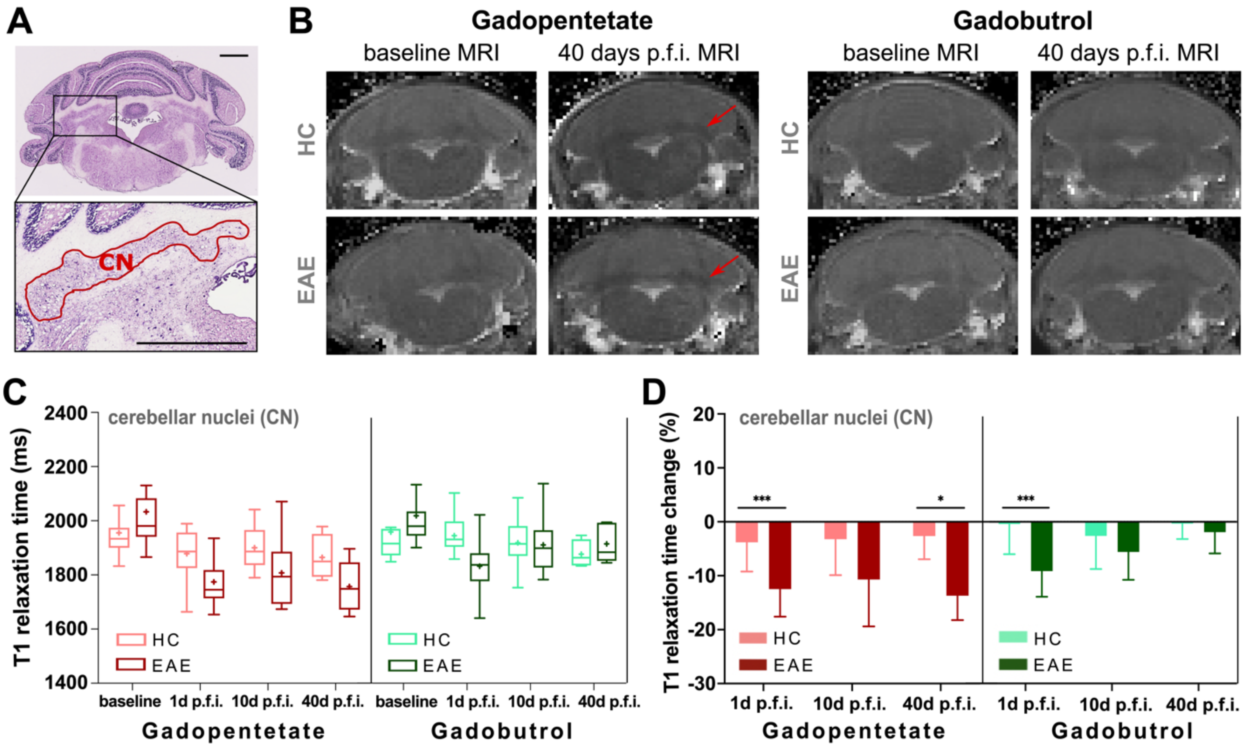

Figure 10: 7 Tesla MRI relaxometry of the CN region *in vivo*. A H&E bright field image of the cerebellum (2x magnification) and CN (10x). Scale bars: 1 mm. **B** Representative coronal MR images (T_1map RARE-VTR sequence) of the cerebellum of HC and EAE mice at baseline and 40 days p.f.i. of both GBCAs. Scans reveal a qualitative T_1 time shortening within the area of CN (red arrow) after gadopentetate administration. **C** Quantitative T_1 times (in ms) of the CN of EAE and HC mice at baseline and MRI time points p.f.i. of both GBCAs obtained by atlas registration. Data are displayed as Tukey plot, Box shows the first and third quantile, line shows the median, + shows the mean. **D** T_1 relaxation time change (in %) of the CN of EAE and HC animals over three consecutive time points p.f.i. of both tested GBCAs. Data are displayed as mean ± SD. *Bonferroni correction was applied for multiple testing over four (C) or three (D) consecutive time points. (Figure 10A, B and D are derived from Anderhalten et al., 2022 (81); Figure 10C: own representation, unpublished)*

3.3 LA-ICP-MS confirms augmented Gd retention in EAE cerebella

After GBCA administration, LA-ICP-MS of cerebellar mouse brain slices detected relevant differences in Gd distribution patterns between EAE and HC mice as well as between both tested GBCA types (Figure 11A). While in gadopentetate-treated HC brains, Gd retention was locally limited to the CN, EAE cerebella additionally demonstrated a relevant cortical Gd accumulation at all assessed time points. In addition to the medulla, particularly granular layers of the cerebellar cortex demonstrated high Gd retention until day 40 (41.24 ± 6.97 µM). Contrary to that, gadobutrol caused a rather diffuse Gd retention at low levels that concentrated in the periventricular areas and choroid plexus on days 1 and 10 p.f.i., but diminished almost completely toward day 40 (Figure 10A).

Semi-quantitative analysis of the ablated CN region (Figure 11B) revealed that Gd retention was augmented during neuroinflammation for both GBCAs tested, but to different extents and durations. After the administration of gadopentetate, Gd levels were generally 2-fold higher in EAE compared to HC CN and even increased toward day 40 p.f.i. of gadopentetate (EAE vs. HC, 55.06 ± 0.16 µM vs 30.44 ± 4.43 µM) (Figure 11C). In contrast, Gd retention was only transient after repeated administration of gadobutrol. While 24 h p.f.i., the CN of EAE mice contained 2- to 3-fold higher Gd levels compared to HC, differences decreased by day 40, where detected Gd levels were lower than 0.40 µM for both EAE and HC mice (EAE vs HC, 0.38 ± 0.08 µM vs 0.17 ± 0.03 µM) (Figure 11C).

Furthermore, mean Gd concentrations within the CN correlated significantly with mean T_1 change values obtained from *in vivo* MRI (r_s=-0.7972; p=0.0029) (Figure 11D).

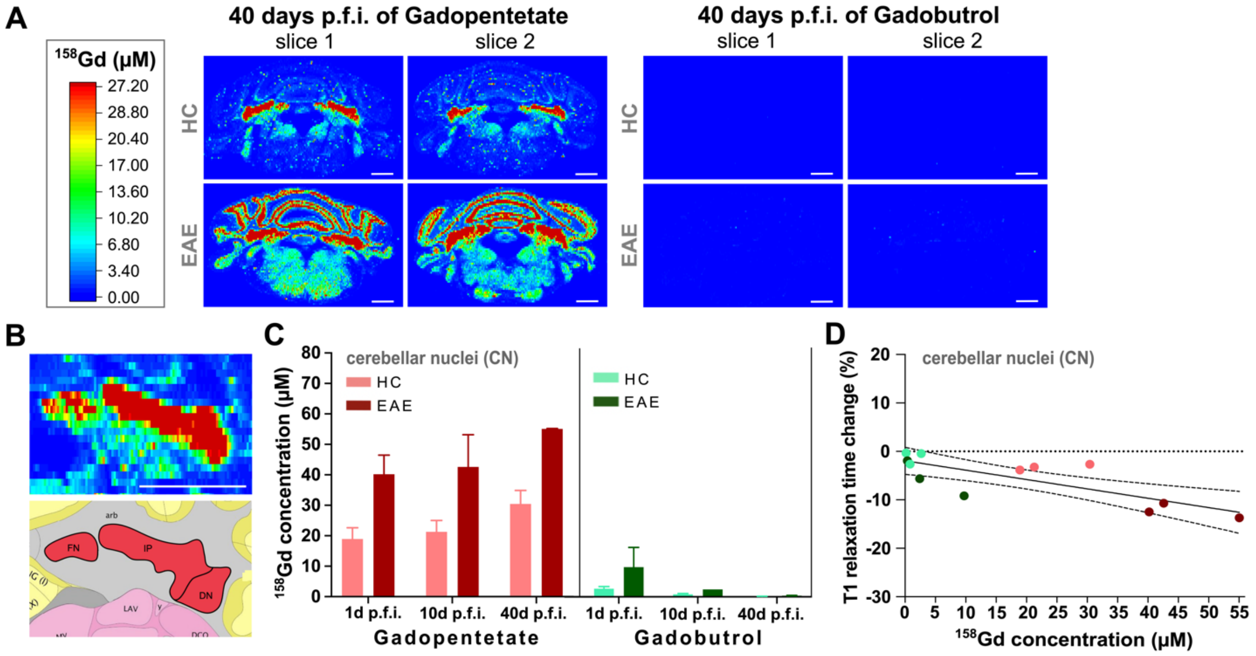

Figure 11: Analysis of cerebellar Gd retention using LA-ICP-MS. A LA-ICP-MS images display cerebellar Gd distribution for HC and EAE mice on day 40 after repeated gadopentetate or gadobutrol administration (in µM; n=2/group). **B** At the top: LA-ICP-MS section showing the CN; at the bottom: Allen brain atlas correlation image of the CN formation showing the fastigial nucleus (FN), interposed nucleus (IP), and dentate nucleus (DN) (from left to right; http://atlas.brain-map.org/atlas). **C** Analysis of Gd concentrations within the CN of HC and EAE mice over three consecutive time points p.f.i. of GBCAs (in µM; n=2/group). Data are displayed as mean ± SD. **D** Significant inverse correlation (*p=0.0029)* between Gd levels (CN, mean in µM) and T_1 change (CN, mean in %). Colors of data points correspond to groups displayed in C. *Scale bars: 1 mm. (Figure 11A and C are derived from the study by Anderhalten et al., 2022 (81); Figure 11C and D: own representation)*

3.4 LA-ICP-MS detects higher Zn levels within the CN of EAE mice

Most of the additionally examined isotopes displayed no relevant differences between EAE and HC brains. However, laser ablation images demonstrated qualitatively higher Zn concentrations in cerebellar sections of EAE animals compared to HC, regardless of the GBCA type administered. Concerning the distribution of Zn in cerebellar slices of EAE mice, particularly high levels of Zn were observed in the white matter around the CN and inside the cerebellar cortex (Figure 12A). Semi-quantification of Zn levels revealed that mean concentrations inside the CN were consistently about 1.7-fold higher in EAE compared to HC mice (range: 1.64-1.74-fold). While this ratio of zinc levels between inflamed and healthy CN remained similar until day 40 (EAE vs. HC; both GBCAs pooled, 319.46 ± 42.31 µM vs. 195.07 ± 47.62 µM), an overall declining trend in absolute Zn levels from day 1 to day 40 p.f.i. of GBCAs was observed in both EAE and HC mice (26 % decline in EAE mice vs. 22 % in HC) (Figure 12B).

The analysis of Fe tissue intensities in ablated cerebellar slices revealed high individual variability between HC and EAE mice. There was no significant correlation found between the EAE score of mice and cerebellar Fe content (data is not shown). However, in most of the cerebellar slices, high local Fe intensities overlapped with retained Gd within the area of CN (Figure 12C). Similar overlapping elemental distributions with Gd retention patterns inside the CN were observed for Cu and P, while Ca was distributed more homogeneously. Interestingly, the dissemination of P throughout the cerebellar section resembled the distribution of Zn and was particularly concentrated in the white matter. The highest Cu intensities were allocated to periventricular areas of the cerebellum (Figure 12C).

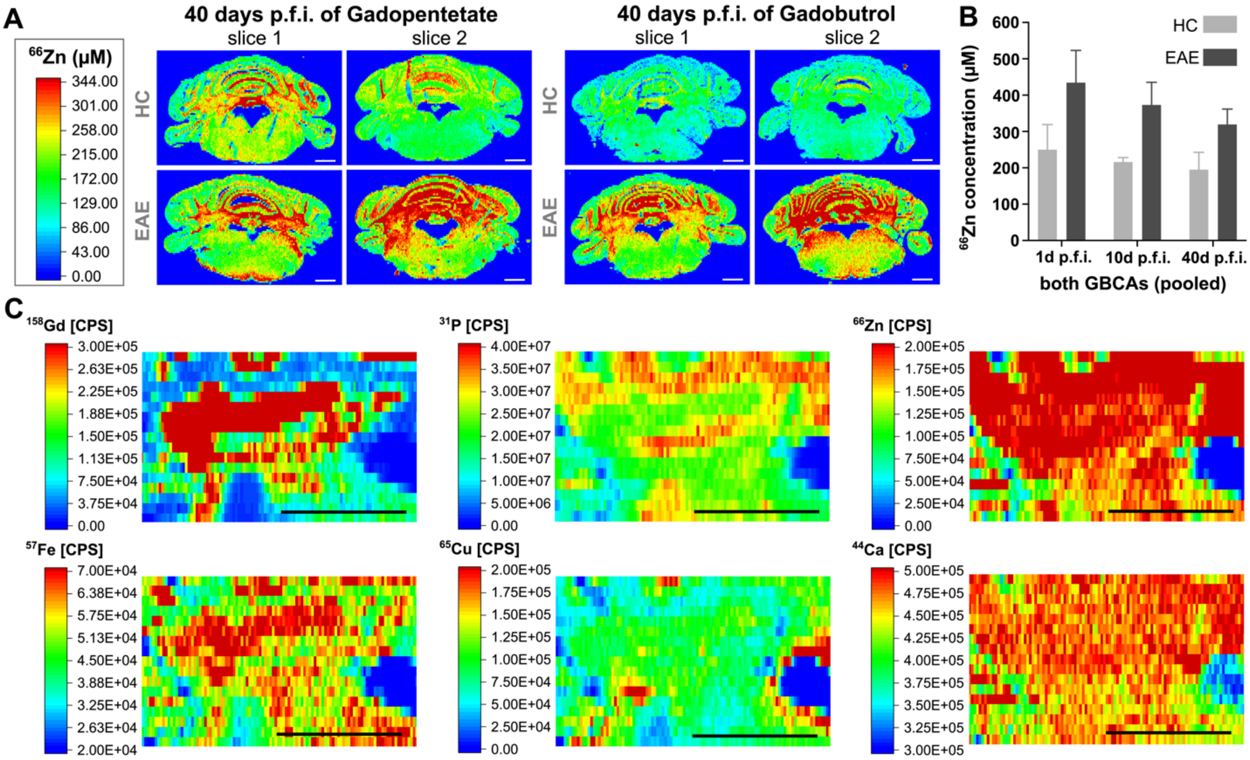

Figure 12: Analysis of the distribution of cerebellar elements using LA-ICP-MS. A LA-ICP-MS images display cerebellar Zn distribution for HC and EAE mice on day 40 p.f.i. of gadopentetate or gadobutrol (in µM; *n*=2/group). **B** Analysis of Zn concentrations within the CN of HC and EAE mice over three consecutive time points p.f.i. of GBCAs (in µM; *n*=2/group). Data are displayed as mean ± SD. **C** Distribution of assessed elements within the area of CN (EAE brain, 10 days p.f.i. of gadopentetate); all scales are displayed as ablation intensity (CPS) for better comparability. Top row: ^{158}Gd, ^{31}P, ^{66}Zn; bottom row: ^{57}Fe, ^{65}Cu, ^{44}Ca. *Scale bars: 1 mm. (Derived from Anderhalten et al., 2022 (81).)*

3.5 ICP-MS reveals enhanced Gd blood levels until day 40 p.f.i. of both GBCAs

ICP-MS detected elevated levels of Gd in all analyzed blood samples (day 1, 10, and 40 p.f.i.; both GBCAs) compared to the blood of an untreated age- and gender-matched control mouse (Table 6). In EAE blood, Gd concentrations were increased compared to HC at all time points (exception: day 10 p.f.i. of gadopentetate). 24h p.f.i. of gadopentetate, around 0.0048% of the injected cumulative dose of 20 mmol/kg BW were detected in the blood of EAE mice and 0.0015% in the case of HC mice (1.89 ± 0.08µg/g vs. 0.58µg/g, no SD as n=1). On the other hand, 24h p.f.i. of gadobutrol, around 0.0031% of the cumulative dose were traceable inside EAE blood, and 0.0028% in HC blood (1.20 ± 1.28 µg/g vs. 1.10 ± 1.04 µg/g). At day 40, the maximum detectable Gd blood levels still corresponded to 0.0019% of the initially applied cumulative dose (EAE mice, gadopentetate). The Gd contents of all individual blood samples are shown in Table 6.

Table 6: Analysis of Gd blood content using ICP-MS.

Time point (p.f.i. of GBCA)		**C_{Gd} post Gadopentetate**			**C_{Gd} post Gadobutrol**		
		sample 1	*sample 2*	*mean*	*sample 1*	*sample 2*	*mean*
1 day p.f.i.	**HC**	0.58	/	**0.58**	1.84	0.37	**1.10**
	EAE	1.95	1.84	**1.89**	2.11	0.29	**1.20**
10 days p.f.i.	**HC**	0.88	0.21	**0.54**	0.18	0.12	**0.15**
	EAE	0.42	0.07	**0.25**	1.36	0.24	**0.80**
40 days p.f.i.	**HC**	0.83	0.03	**0.43**	0.65	0.02	**0.34**
	EAE	0.84	0.65	**0.74**	0.77	0.11	**0.44**
naive control		**< 0.002**					

Note: Gd concentrations are given in µg/g; results are displayed as mean, *n*=2 per group; HC at day 1 p.f.i of gadopentetate: *n*=1 due to sample contamination. (*Data was partly visualized in the supplementary digital content by Anderhalten et al. (81); means only. This table contains additional unpublished details.)*

3.6 *In vivo* T_1 relaxometry underestimates shortening of cerebellar T_1 relaxation times after gadopentetate administration

Using *in vitro* T_1 relaxometry, we determined the ability (r_1) of gadopentetate and gadobutrol standards containing Gd concentrations of 20-100 µM to trigger T_1 shortening in water, FBS, and homogenized brain tissue (Figure 13A). Compared to mean r_1 values in water (gadopentetate vs. gadobutrol, 3.37 vs. 3.22 $mM^{-1}s^{-1}$), r_1 increased for both gadopentetate and gadobutrol in FBS (3.50 vs. 4.12 $mM^{-1}s^{-1}$) as well as in homogenized mouse brain (4.35 vs. 6.96 $mM^{-1}s^{-1}$; T_1, R_1 and r_1 values are detailed in Table 7), albeit to different extents. Tested GBCA standards demonstrated a good fit to the linear regression model (homogenized brain; gadopentetate, $R^2 = 0.97$; gadobutrol, $R^2 = 0.98$) as illustrated exemplarily in Figure 13B. This data has not been published yet.

Table 7: 7 Tesla MRI calibration for gadopentetate and gadobutrol in homogenized mouse brain

C_{Gd} (µM)	**Gadopentetate**			**Gadobutrol**		
	T_1	***R_1***	***r_1***	***T_1***	***R_1***	***r_1***
In brain: *0*	1966.30	0.51	**4.35**	2010.39	0.50	**6.96**
20	1823.80	0.55		1604.50	0.62	
40	1481.12	0.68		1221.78	0.82	
60	1333.60	0.75		1092.11	0.92	
80	1251.19	0.80		994.56	1.01	
100	1051.07	0.95		818.02	1.22	

Note: T_1 values are given in ms (mean, *n*=2), R_1 values in s^{-1} (mean, *n*=2), r_1 values defined by linear fitting of R_1 in relation to concentrations of Gd^{3+} (20 µM – 100 µM) are given in $mM^{-1} s^{-1}$. (*This data is unpublished. Table only contains calibration metrics in brain homogenate. T_1 and R_1 measures in H_2O and FBS are not shown; r_1 values are given in the text, respectively.)*

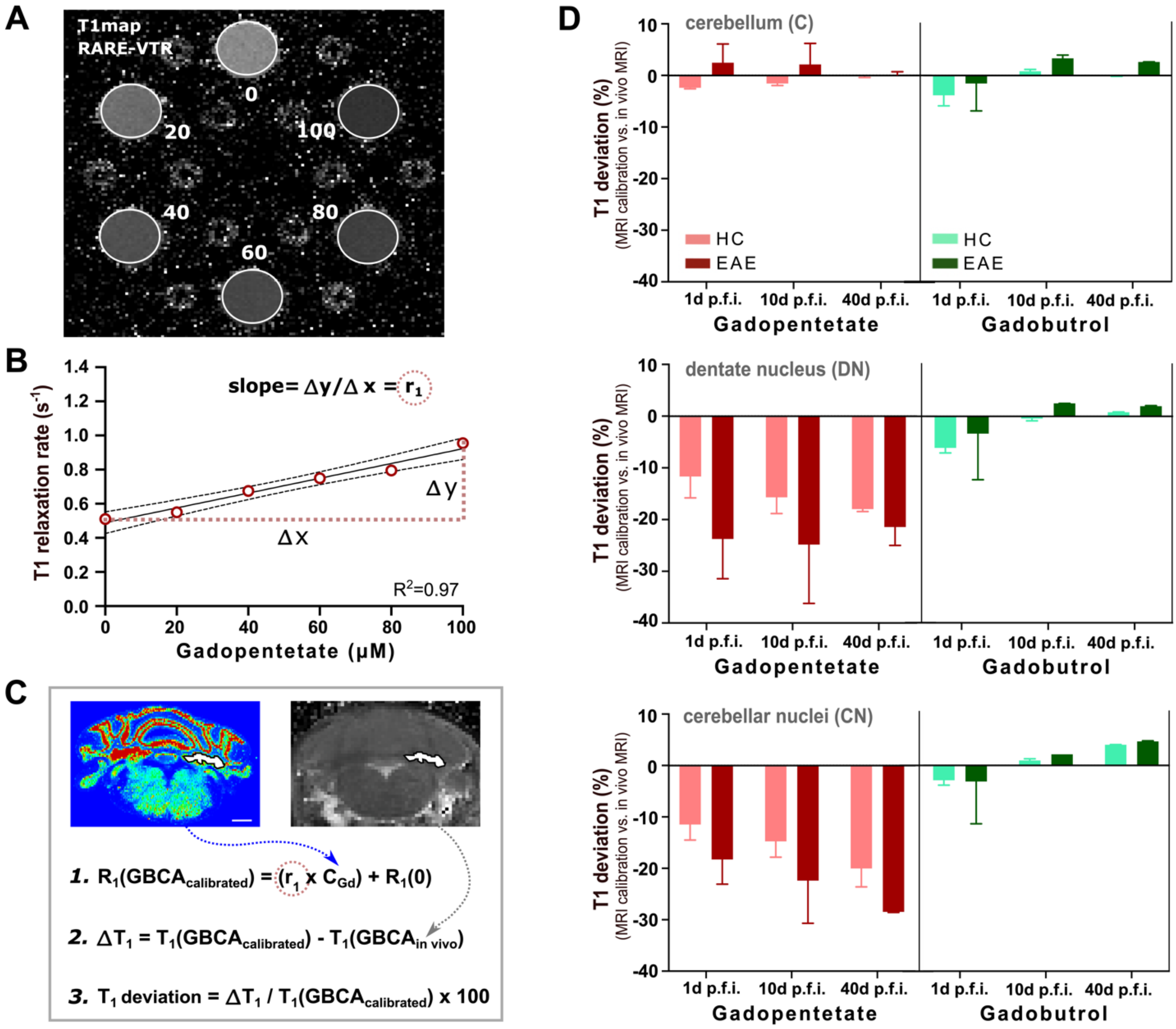

Figure 13: 7 Tesla MRI calibration *in vitro*. **A** T_1map image of simultaneously scanned NMR calibration tubes with increasing gadopentetate concentrations (20-100 µM). **B** Exemplary determination of the T_1-relaxivity (r_1) by linear fitting of longitudinal relaxation rates (R_1) in relation to increasing concentrations of gadopentetate. R_1 is the reciprocal value of T_1. **C** Illustration of the calculation of T_1 percentage deviation comparing the calibrated T_1 to T_1 values from *in vivo* MRI at equal Gd concentrations. Scale bar: 1 mm. **D** T_1 percentage deviation is displayed for the cerebellum, DN, and CN for both tested GBCAs (*n*=2 per group, mean ± SD). Within the CN and DN, T_1 values deviated negatively after gadopentetate administration. *(own representation)*

The computation of T_1 deviation (%) comparing calibrated T_1 to *in vivo* T_1 values at equal Gd concentrations was done for the three brain areas semi-quantitatively assessed by LA-ICP-MS: CN, DN, and the whole cerebellum (Figure 13C). Mean T_1 relaxation times measured *in vivo* inside the whole cerebellum deviated only slightly from calibrated values, which was consistent for both EAE and HC mice as well as both GBCA types over all three consecutive time points (Figure 13D). Interestingly, we observed a strong negative T_1 deviation for the area of CN and DN after gadopentetate administration only, indicating that absolute T_1 relaxation times measured *in vivo* were longer (less shortened) than the corresponding calibrated values. Thus, *in vivo* T_1 relaxometry underestimated the paramagnetic effect of retained Gd inside the CN and DN after gadopentetate administration. As shown in Figure 13D, T_1 underestimation within the CN and DN was more pronounced in EAE compared to HC mice (generally about 1.20-2.0-fold stronger in EAE mice), while it showed a stable or increasing trend until day 40 p.f.i. for both groups (EAE vs HC; CN, -28.47 ± 0.12 % vs -20.03 ± 3.59 %; DN, -21.43 ± 3.56 % vs -17.98 ± 0.47 %). Contrary to that, after gadobutrol application, the T_1 shortening effect of Gd accumulated within the CN and DN was slightly underestimated by *in vivo* MRI 24 hours p.f.i. for both EAE and HC mice (EAE vs HC; DN, -3.36 ± 8.92 % vs -6.12 ± 0.97 %; CN, -3.14 ± 8.20 % vs -2.90 ± 0.95 %), while at day 10 and 40 p.f.i. of gadobutrol T_1 only marginally deviated from calibrated values (Figure 13D). We merely conducted descriptive data analysis as the low LA-ICP-MS sample size of *n*=2/group did not allow for quantitative statistics. This data has not been published yet.

3.7 Gadopentetate induces neuronal cell death in chronic hippocampal slices

The neuronal viability after 48h treatment with GBCAs at 1, 10, and 50 mM, respectively, was assessed within the DG region of the hippocampus, as displayed in Figure 14A. The quantification of dead cells within this area revealed that gadopentetate exerted cytotoxic effects at a concentration of 50 mM, while for gadobutrol no toxicity was discovered at any of the tested concentrations (Figure 14B+C). The gadopentetate-induced cell death rate was significantly enhanced with simultaneous TNFα treatment at 50 ng/ml (TNFα vs. no TNFα, 3.15 ± 1.18 % vs. 2.17 ± 1.14 %, p=0.0345). In positive controls, the cell death rate was strongly increased by NMDA at 50 µM, and this effect was significantly augmented with TNFα treatment (34.34 ± 11.14 % vs. 19.70 ± 9.19 %, p=0.0002). As shown in Figure 14B and C, negative control slices demonstrated excellent neuronal survival, also under additional TNFα treatment (0.27 ± 0.45 % vs. 0.16 ± 0.49 %).

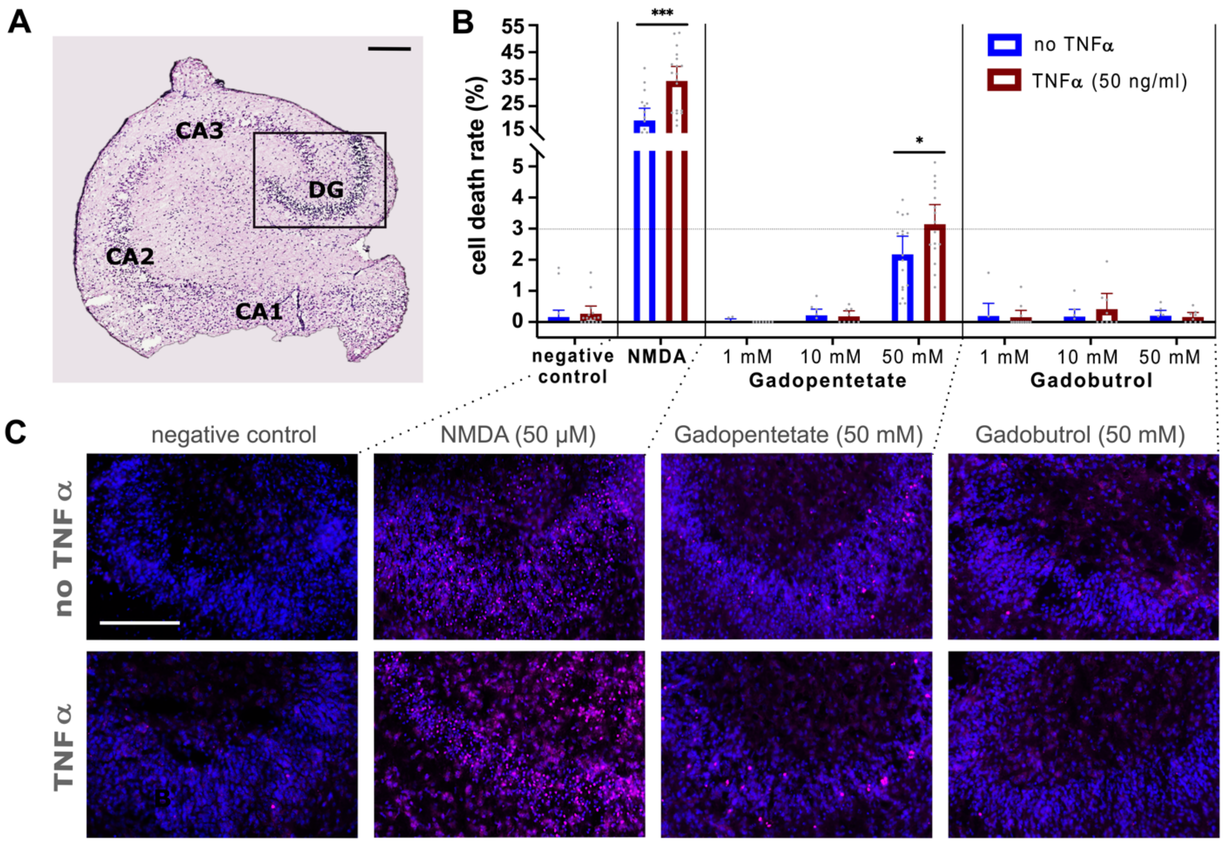

Figure 14: Toxicity assessment of GBCAs *ex vivo.* A H&E bright field image showing the hippocampal formation: dentate gyrus (DG), cornu ammonis subdivided into CA1, CA2, and CA3. **B** Demonstration of cell death rate (%) after slice culture incubation with GBCAs at 1, 10, and 50 mM ± TNFα. Positive control slices were treated with NMDA for neurotoxicity induction (*n*=8-22, mean ± SD). **C** Exemplary fluorescence images of the DG for the most relevant experimental conditions (negative control, NMDA, gadopentetate or gadobutrol at 50 mM). DAPI = all nuclei (blue), PI = dead nuclei (red). *Scale bars: 200 µm. (Figure 14A: own representation; Figure 14B-C are derived from the study by Anderhalten et al., 2022 (81).)*

3.8 IMC reveals homogeneous Gd retention in brain slices post-GBCA treatment

IMC measurements confirmed that both GBCAs had successfully penetrated the chronic hippocampal slices during *ex vivo* treatment at 10 mM for 48h. Semi-quantitative assessment of Gd content within the DG region revealed that the average ^{158}Gd ion count after gadopentetate treatment was 26-fold higher compared to slices treated with gadobutrol (6.07 ± 1.32 ^{158}Gd count vs. 0.23 ± 0.02 ^{158}Gd count). Comparing gadobutrol-treated to untreated control slices, the mean ^{158}Gd ion count was still 12-fold greater after gadobutrol incubation (0.23 ± 0.02 ^{158}Gd count vs. 0.02 ± 0.01 ^{158}Gd count) (Figure 15A). The distribution of retained Gd within the hippocampal slices, including the respective DG regions, was relatively homogeneous after incubation with both GBCAs (Figure 15B). ^{191,193}Ir was used to label nucleic acids and visualize the position of nuclei by IMC. In gadopentetate-treated slices, regions of high ^{158}Gd counts colocalized with the $^{191,\,193}$Ir signal (Figure 15B).

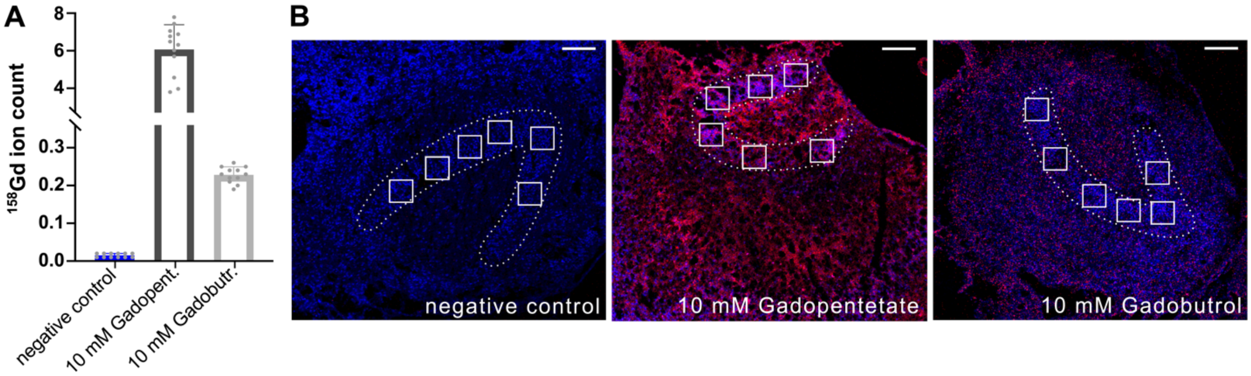

Figure 15: Assessment of Gd retention within the DG *ex vivo*. A Semi-quantification of ^{158}Gd ion count within DG region of hippocampal slices after gadopentetate or gadobutrol treatment at 10 mM and negative control slices (6 ROIs/DG, 2 slices/group; *n*=12). **B** IMC images of negative control slice and GBCA-treated slices. Blue: $^{191,\,193}$Ir ion count, red: ^{158}Gd ion count. Dashed lines mark DG region, white boxes mark ROIs for semi-quantification of ^{158}Gd ion count. Scale bars: 200 µm. *(Figure 15A: own representation; Figure 15B: modified from Anderhalten et al., 2022 (81) with kind permission by Wolters Kluwer Health, Inc.)*

3.9 ICP-MS quantifies Gd retention in chronic slices after GBCA treatment

Within digested solutions of hippocampal slices incubated with GBCAs at 10 and 50 mM for 48h, ICP-MS detected Gd concentrations between 81 and 612 µg/g, as shown in Table 8 (= approx. between 0.54 and 4.07 mM; 3-8 % of the originally applied GBCA dose). Gd levels were enhanced in slices treated with GBCA concentrations of 50 mM compared to 10 mM (+/- TNAα), suggesting a dose-dependent effect of retention. There was a trend for increased Gd levels after gadopentetate compared to gadobutrol treatment at 10 mM. After gadopentetate treatment, the cytotoxic Gd concentration - determined via computation of the neuronal cell death rate - corresponded to about 1.5 mM, i.e. 3% of the initially administered 50 mM. Control samples (+/- TNAα) yielded Gd concentrations below the limit of quantification (<0.16 ng/g) (Table 8). This data is unpublished.

Table 8: Analysis of Gd content within chronic hippocampal slices using ICP-MS.

C_{GBCA} (48 h)	C_{Gd} post Gadopentetate			C_{Gd} post Gadobutrol		
	-TNFa	*+TNFa*	*mean*	*-TNFa*	*+TNFa*	*mean*
10 mM	100.07	123.74	111.91	83.08	81.26	82.17
50 mM	248.40	200.92	224.66	611.70	228.34	534.19
untreated control	< detection limit (0.16 ng/g Gd)					

Note: C_{Gd}=Gd concentrations in µg/g, C_{GBCA}=GBCA concentrations in mM; *n*=1 per group. (*This data is unpublished.)*

4 Discussion

4.1 Summary of essential results

This thesis investigated inflammation-promoted cerebellar Gd retention profiles and kinetics using quantitative T_1 relaxometry and LA-ICP-MS after repeated administration of linear gadopentetate and macrocyclic gadobutrol in the EAE mouse model. In the presence of neuroinflammation, both GBCAs caused enhanced Gd retention in cerebellar structures, but gadopentetate to a greater absolute extent and duration. Gadobutrol was efficiently eliminated from the cerebellum over time in HC and EAE mice. In contrast, gadopentetate induced long-term retention of Gd until day 40 p.f.i., particularly within the CN of all mice. In EAE mice, Gd retention reached maximum concentrations of 55 µM and additionally extended to the cerebellar cortex. Within the CN, LA-ICP-MS revealed a spatial overlap between high local Gd levels and Zn and Fe distribution patterns. In addition, cerebellar Zn concentrations were consistently higher in EAE compared to HC brains. *In vivo* MRI underestimated the paramagnetic shortening effect of retained Gd on T_1 relaxation after gadopentetate administration over the entire observational period.

Using the *ex vivo* model of chronic organotypic hippocampal slice cultures, we further investigated potential neurotoxic effects of both GBCAs on living inflamed and naïve brain tissue. The application of gadopentetate at 50 mM resulted in about 1.5 mM Gd retention in the chronic slices *ex vivo*, which impaired neuronal viability inside the DG, particularly under inflammatory conditions. Despite the demonstration of Gd retention *ex vivo* through ICP-MS, no cytotoxic effects were observed after gadobutrol administration. IMC revealed that Gd was retained homogeneously in the tissue slices after treatment with both GBCA and colocalized with nucleic acids.

4.2 Interpretation of *in vivo* results on inflammation-promoted Gd retention

Using quantitative T_1 relaxometry *in vivo*, we showed that multiple i.v. injections of both GBCAs initially resulted in relevant cerebellar T_1 shortening, which was enhanced in EAE mice for both agents tested. In gadopentetate-treated mice, T_1 remained shortened until day 40 p.f.i., predominantly in the CN region (Figure 16), while it had declined to baseline values by that day in gadobutrol-treated mice. T_1 relaxometry studies investigating Gd retention after a controlled number of GBCA injections in neuroinflammatory compared to healthy conditions are generally lacking, and only a few recent studies conducted quantitative MRI investigating Gd retention inside the DN region of MS (71, 131), or cancer patients (132, 133). In line with our results, these studies reported that persistent T_1 shortening was mainly related to linear GBCAs, while after repeated macrocyclic GBCA administration, the observed T_1 decrease was non-permanent (71, 131-133).

Consistent with our previous findings (80), our LA-ICP-MS data further substantiate the augmented cerebellar accumulation of Gd in EAE compared to HC mice, thus corroborating the indications from our *in vivo* T_1 relaxometry results. Neuroinflammation favored the initial retention of both tested GBCAs to a comparable extent, however, gadopentetate mostly caused a higher and more stable Gd retention in EAE and HC brains than gadobutrol. Initial differences in retained Gd levels, comparing both GBCA types, were small when considering average cerebellar values 24h p.f.i., but pronounced for the CN region (including DN) in HC and EAE brains, respectively. Thereafter, both agents differed considerably in their Gd retention kinetics over time. After gadopentetate application, we found evidence of long-term Gd accumulation within the CN of EAE brains, and less pronounced in HC (Figure 16). In both HC and EAE CN, Gd levels increased over the observation period with maximum levels detectable in EAE mice on day 40 p.f.i. In contrast, gadobutrol was successfully cleared from the cerebellum by that day. This agrees with the premise that Gd deposition is primarily related to the lower intrinsic kinetic and thermodynamic stability of linear GBCAs (1). Speciation analyses of rodent brains revealed that the dissociation of GBCAs *in vivo* results in the formation of insoluble and soluble Gd deposits (50, 51, 134). In contrast, macrocyclic GBCAs were reported to be retained transiently, mainly in their soluble intact chelate (24, 47), with clearance rates depending on specific intrinsic washout kinetics (44, 45) (Figure 16).

In healthy individuals, Gd retention was suggested to result from GBCA uptake from the bloodstream via the blood-CSF-barrier (BCB) into the CSF (89, 135) (Figure 16). Fenestrated BCB capillaries and lacking tight junctions between ependymal cells of the choroid plexus may allow the diffusion of GBCAs into the CSF (60). The GBCA-containing CSF may then reach the brain parenchyma via subarachnoid spaces and the glymphatic system, including perivascular spaces (11, 89, 136-139), or infiltrate brain areas in proximity to the ventricles via passive diffusion (89). Single i.v. applications of linear and macrocyclic agents resulted in an initial enrichment of both GBCA types in the CSF of healthy rats, which were equally and almost entirely cleared from the CSF within 24 h. At this early point, there was no relevant difference in mean cerebellar Gd content between gadopentetate- and gadobutrol-treated rats (135), aligning with our findings in mice.

During neuroinflammation, BBB permeability is enhanced (60, 80) and alterations of the choroid plexus occur (140-142). The breakdown of the BBB represents a major hallmark of MS and EAE neuropathology. We hypothesize that in the absence of BBB disruption, both GBCA types may initially reach the brain parenchyma more or less independently of their chemical structure (Figure 16), while the specific complex stability might rather influence subsequent GBCA elimination from the brain. We further suggest that increased BBB leakage may additionally amplify the uptake of GBCAs into the brain in EAE mice. This could explain the initially increased cerebellar accumulation of both linear gadopentetate and macrocyclic gadobutrol in EAE compared to HC mice.

As mentioned, we noticed that Gd levels in the CN of HC and EAE mice increased from day 10 to day 40 p.f.i. of gadopentetate. Similar delayed rising trends of Gd were observed in skin biopsies of patients with NSF, despite no additional GBCA was injected (41). Bones have been reported to retain Gd for over eight years, possibly due to transmetallation with available Ca^{2+} and binding to inorganic phosphates (108, 143). The delayed increment in CN Gd content could be due to the release of Gd^{3+} from storage sites such as the bones (4, 14, 108, 109). Our ICP-MS blood analyses support this theory since we found that Gd was detectable in all blood samples up to day 40 p.f.i. of both GBCAs. A recent study indicated that although Gd is continuously cleared from the plasma, it may accumulate in red blood cells over the long term, mainly after linear GBCA injections (27), potentially serving as a transport medium for Gd. We hypothesize that brain Gd levels may increase due to either Gd redistribution within the brain or the contribution of Gd stored in bones through mobilization into the bloodstream and extended recirculation throughout the body.

Neuroinflammation significantly affected the distribution patterns of cerebellar Gd retention following linear GBCA administration. In HC brains, the cerebellar Gd retention was locally limited to the CN until day 40 p.f.i. of gadopentetate, while in EAE brains, it permanently extended to cortical granular layers of the cerebellum (Figure 16). On the other hand, both HC and EAE brains demonstrated a rather diffuse and temporary Gd retention after gadobutrol administration. We propose that in EAE, inflammation-mediated cellular, biochemical, and structural tissue alterations, including modifications of extracellular matrix (ECM) components (144-148), may collectively influence the long-term retention of particularly kinetically less stable, linear GBCAs inside the CNS.

Recent evidence supports the theory of dissociation of linear GBCAs *in vivo* and subsequent transchelation of Gd^{3+} with endogenous macromolecules, resulting in parenchymal retention of Gd (24, 51, 80). The appearance of Gd deposits within various human body tissues suggests that Gd^{3+} may bind to macromolecular species ubiquitously distributed like albumin, ferritin (89), or citrate (149). Other potential targets of interest are glycosaminoglycan (GAG) structures found in the ECM or on the surface of cells as part of the glycocalyx (43, 119, 134, 149, 150). GAGs are negatively charged polysaccharides usually attached to core proteins, forming proteoglycans (151). Due to their high cation-binding capacities, they are promising macromolecular candidates with complexing abilities (119, 149). Alterations in GAG composition in brains of EAE mice (148) and in active demyelinating lesions of MS patients (152) indicate their pro-inflammatory role in neuroinflammation. They may amplify the inflammatory response by affecting the diffusion of soluble factors (153) and trafficking of leukocytes within the ECM (154). Sulfate groups present within GAGs could play a crucial role in the transchelation process with Gd^{3+}. The degree of sulfation seems to determine a GAG’s specific complexing ability, with increasing sulfate levels resulting in enhanced transchelation rates (149). Inflammation-induced changes in GAG sulfation on brain endothelial cells facilitated the binding and internalization of iron oxide nanoparticles (144). Thus, increased transchelation rates due to inflammation-induced modifications in GAG sulfation and GAG accumulation may be considered a possible contributor to inflammation-promoted Gd retention p.f.i. of gadopentetate, observed in our study.

Using LA-ICP-MS, we found that the CN were a predilection site for long-term Gd retention in HC and EAE brains after gadopentetate injection. Within this area, retained Gd overlapped spatially with the distribution patterns of Fe, Zn, Cu, and P. In addition, the Zn content in ablated EAE cerebella was generally higher compared to HC, regardless of the GBCA type administered. An imbalance of Zn in the brain may be involved in the development of MS and EAE, as it functions as a cofactor for several enzymes and proteins, such as matrix metalloproteinases (MMP) and the myelin basic protein. An elevated neuronal release of Zn may activate MMPs, leading to BBB leakage, demyelination, and neuronal damage in EAE (155, 156). We additionally observed that cerebellar Zn levels decreased in all brains over the observation period. In this context, previous studies reported on the depletion of Zn brain content after the administration of linear GBCAs, accompanied by zincuria (38, 42, 157). Zn ions seem to have the potential to destabilize linear complexes inducing transmetallation with Gd^{3+} in the presence of GAGs, forming Gd-GAG complexes (43, 119). The local presence of endogenous metals such as Zn within the brain may trigger transmetallation processes dose-dependently.

Thus, resulting from disseminated neuroinflammatory processes, increased Zn levels in EAE brains may promote Gd retention inside the CN and the cerebellar cortex.

The analytical technique of LA-ICP-MS cannot distinguish between intact GBCAs, free Gd^{3+}, and deposited Gd species. We have measured the ability of gadopentetate and gadobutrol to shorten T_1 relaxation times (= r_1) by conducting MRI calibration with GBCA standards in homogenized mouse brain tissue. By comparison to *in vivo* MRI, we aimed to capture the constellation of potential long-term Gd bindings in EAE and HC brains. The central concept is that r_1 is determined by the specific interaction of paramagnetic Gd^{3+} with ^1H. Higher r_1 values indicate a more efficient GBCA in shortening T_1 (43). Higher field strength, viscosity, and compound stability increase r_1 by promoting stronger interactions between Gd^{3+} and ^1H (2). It was further suggested that in MRI, signal enhancement after linear GBCA injection may be explained by the transchelation of Gd^{3+} with soluble macromolecules, resulting in increased r_1 values due to reduced rotational tumbling rates (2, 16, 43, 119, 158). Our study demonstrated that both GBCAs exhibited similar r_1 values in water, aligning with ranges previously reported in the literature (1, 119, 158). In FBS and brain homogenate, r_1 increased for both agents, likely due to higher solution viscosity and Gd^{3+} binding to endogenous macromolecules. The increase in r_1 observed after gadobutrol application suggests that it induces transchelation processes to some extent, which agrees with our *in vivo* T_1 relaxometry findings.

We found that within the CN, the T_1 shortening effect of retained Gd was largely underestimated through *in vivo* MRI until day 40 p.f.i. of gadopentetate, particularly in EAE mice. Contrary to that, gadobutrol only caused a mild underestimation of T_1 shortening on day 1 p.f.i. in both EAE and HC brains. Our findings suggest that after linear gadopentetate injection *in vivo,* Gd was partly retained in deposits that contribute little to T_1 shortening and that this type of deposit was more abundant in the EAE cerebellum. Within the CN, this underestimation even increased toward day 40 p.f.i. of gadopentetate in both EAE and HC mice, indicating that the portion of retained Gd marginally contributing to T_1 shortening increased over time. It has been suggested that the influence of inorganic $GdPO_4$ salts on T_1 shortening in MRI is potentially weak due to its low solubility (33, 40). Linear GBCAs may dissociate and precipitate *in vivo* forming insoluble Gd species in areas of high endogenous ion content, while macrocyclic GBCAs mainly stay intact (24, 50, 51, 134). After linear GBCA administration, insoluble deposits were found in the brain of patients (29, 31, 33) and rodents (51, 138, 159), e.g. within CN capillary walls (29, 33, 138) or neuronal nuclei in DN specimens (31). In rat brains, the largest portion of retained Gd was present in such deposits with spherical or spiky urchin-like appearance, mainly composed of $GdPO_4$ (51, 89). We hypothesize that the presence of such inorganic Gd deposits after gadopentetate administration triggers the T_1 underestimation observed in our study. During neuroinflammation, both insoluble precipitates and soluble macromolecular Gd deposits may be promoted, resulting in stronger long-term T_1 shortening in EAE and enhanced T_1 underestimation compared to HC mice (Figure 16). The granular layer of the cerebellar cortex is rich in inorganic phosphates (33), which may contribute to increased Gd retention within this area in gadopentetate-treated EAE brains. In contrast, gadobutrol induced only a transient T_1 decrease *in vivo* with minimal CN T_1 deviation. This may be attributed to subtle dissociation and transchelation processes, forming temporary Gd^{3+} bindings, or binding of the intact chelate, resulting in a prolonged residence time, particularly in EAE brains.

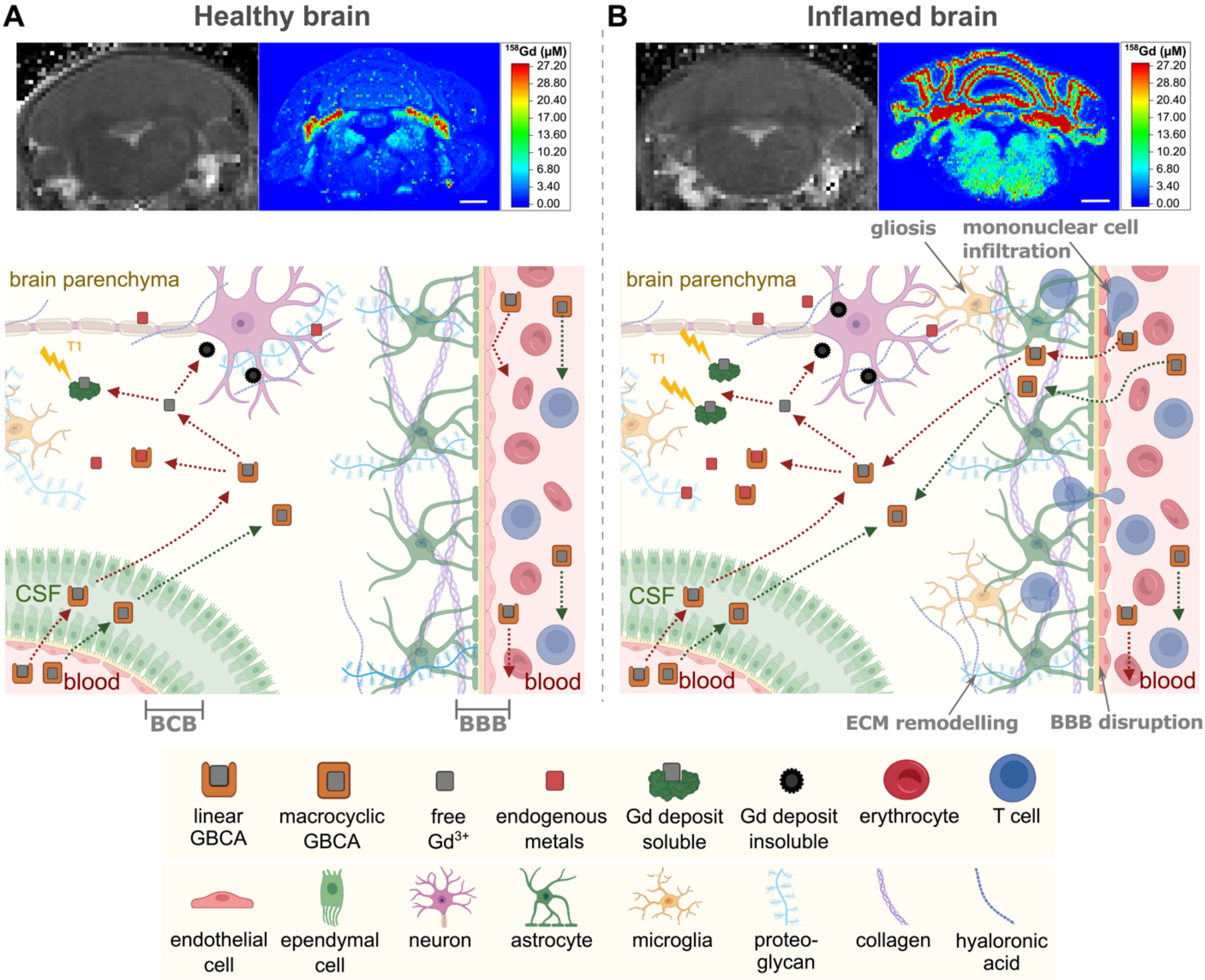

Figure 16: Discussion of essential *in vivo* results. A In the healthy CNS, gadopentetate administration caused long-term Gd retention inside the CN. In the presence of an intact BBB, GBCAs potentially enter the brain via the blood-CSF-barrier (BCB). Retained inside the brain, gadopentetate may dissociate in the

presence of endogenous metals such as Zn or Fe, releasing Gd^{3+}. Free Gd^{3+} then binds to macromolecules, forming soluble Gd species, or precipitates as insoluble Gd species. Gadobutrol was effectively cleared from the brain, likely as intact chelate. **B** In the inflamed brain, Gd retention was enhanced after the application of both GBCAs, reflected by shorter T_1 values *in vivo*. After gadopentetate administration, Gd retention extended beyond the CN to cortical areas of the cerebellum. Augmented precipitation of Gd^{3+} may explain enhanced T_1 underestimation in inflamed brains after gadopentetate injection. BBB disruption and endogenous metal changes may contribute to inflammation-promoted Gd retention. *(own representation)*

4.3 Interpretation of *ex vivo* results on GBCA toxicity during inflammation

We have established and utilized chronic hippocampal slice cultures to investigate the potential neurotoxic effect of GBCAs on living brain tissue without the influence of a BBB. Treatment of slice cultures with gadopentetate at 50 mM for 48h reduced the neuronal viability within the DG area, while gadobutrol treatment did not exert cytotoxic effects at any of the tested concentrations. Consistent with our results, treatment of neuronal cell lines with linear, potentially dissociating GBCAs in the mM range resulted in dose-dependent cell death (160, 161). This was accompanied by a decrease in mitochondrial oxidative capacity, membrane potential, and integrity (160) as well as an increase in mitochondrial Bax/Bcl-2 protein ratios (161). As a rare-earth lanthanide metal, Gd^{3+} has been implicated in neurotoxicity primarily through its effects on Ca^{2+} homeostasis and mitochondrial function (162). *In vitro* studies suggest that Gd^{3+} may cross cellular membranes through mechanisms not yet fully understood, leading to the accumulation of intracellular Ca^{2+} (163) and reactive oxygen species (ROS) (163, 164). The competition of Gd^{3+} with Ca^{2+} may induce blockage of voltage-dependent Ca^{2+} channels and Ca^{2+}-dependent enzymes, affecting mechanisms such as neural transmission (37). Under physiological conditions, mitochondrial ATP production generates low levels of ROS, which antioxidant cellular systems effectively neutralize (165). Metal-dependent inhibition of mitochondrial metabolic activity may induce abnormal ROS accumulation, leading to the opening of mitochondrial permeability transition pores (166), cytochrome c release, and caspase-3 activation (164). Based on this, GBCA toxicity primarily involves the induction of apoptotic pathways through mitochondria-related signaling (160, 161, 163, 164). However, the additional involvement of necrotic pathways may be considered.

TNFα is a pleiotropic inflammatory cytokine that plays a pivotal role in MS and EAE pathogenesis (167) and is frequently employed in *in vitro* models of inflammation (144). In this study, we used TNFα to induce a pro-inflammatory milieu within living brain tissue *ex vivo*. Slice culture incubation with TNFα at 50ng/ml further diminished the neuronal viability during treatment with gadopentetate at 50 mM. We believe, that an arising pro-inflammatory environment may influence Gd-induced neurotoxicity, contributing to the elevated neuronal cell death rate observed *ex vivo*. TNFα may enhance GBCA toxicity by promoting pathways associated with cell death as part of its immunomodulatory function (167, 168), or by reducing the chelate stability due to disturbances in the endogenous metal homeostasis (169) (i.e. Ca^{2+} or Zn (81)). Inflammatory modifications affecting structural and cell-associated macromolecules (144-148) could facilitate the binding of Gd^{3+} to the surface of neurons. This may enhance a potential cellular uptake of Gd^{3+} or Gd species (31, 144). Increased formation of insoluble Gd species within (31) brain cells or intercellular spaces may also impair relevant tissue functions through local space-occupying effects.

Our ICP-MS findings demonstrate that the Gd concentration causing neuronal cell death after gadopentetate administration was approximately 1.5 mM (3% of the initially applied 50 mM), indicating that the level of retained Gd associated with neurotoxicity in hippocampal slices was about 27-fold higher than the maximum Gd levels detected *in vivo* using LA-ICP-MS. Further, 50 mM of externally applied GBCAs resulted in increased Gd slice contents for both agents compared to 10 mM, indicating a dose-dependent slice penetration and retention. Due to the low sample size (*n*=1/group), ICP-MS data allow no statement on the quantitative effect of TNFα on Gd retention levels *ex vivo*. At a GBCA concentration of 10 mM, retained Gd levels in gadopentetate-treated slices were only about 1.4-fold higher compared to gadobutrol-treated ones, in contrast to 26-fold higher Gd counts detected by semi-quantitative IMC. Sample processing for IMC required washing procedures, which potentially leached intact gadobutrol residues from the slices. During ICP-MS preparation, the residues likely stayed inside the tissue, contributing to the detected Gd slice content. However, low Gd content remained after IMC washing steps, either due to incomplete washout, binding of intact gadobutrol to tissue structures, or dissociation of Gd^{3+} from the macrocyclic complex. After treatment with both GBCAs, Gd was retained homogenously within the brain slices. Gd colocalized with Ir-tagged nucleic acids inside the DG, but the IMC image resolution did not allow for a clear differentiation of intra- and extracellular locations of retained Gd.

The significance of these discoveries in living organisms remains uncertain. Among others, *Davies et al.* did not observe any histopathological signs of neurotoxicity in rats after serial i.v. injections of linear GBCAs (25, 28, 114, 150, 170). However, Radbruch *et al.* detected a decrease in nerve fiber density in the skin of mice after a single injection of particularly linear GBCAs (54) and Habermeyer *et al.* observed a transient reduction of the startle response in healthy rats after the application of linear gadodiamide (150). A substantial body of human studies indicates the absence of neurological impairment in patients following cumulative GBCA exposure (162). In MS patients, reports on the effects of GBCA use in terms of clinical outcome and disease severity remain conflicting (131, 171-174). While most studies found no correlation between linear GBCA injection and clinical worsening (171, 173, 174), few report on clinical signs such as lower verbal fluency (131, 172) and information-processing speed (131). No similar associations were found after exclusive macrocyclic GBCA use (131). Determining long-term risks associated with inflammation-promoted Gd retention in patients with chronic neuroinflammatory diseases like MS requires close evaluation of clinical disability, cognition, and behavior, in addition to histological analyses. Permanent Gd retention, mainly seen after linear GBCA injections, may have delayed consequences if exceeding a certain cumulative limit. In addition, investigating the mechanisms and consequences of enhanced and prolonged macrocyclic GBCA retention in neuroinflammation is crucial.

4.4 Quantitative T_1 relaxometry for monitoring of Gd retention

In MS, imaging parameters used in clinical practice often correlate poorly with clinical performance, challenging therapy efficiency and progression monitoring (175). Conventional MRI has certain limitations in assessing the heterogeneity of MS pathology, including SI inaccuracies and the need to normalize target structures by reference regions (22, 176). Quantitative MRI techniques may help resolve the clinical-radiological paradox in MS (175) by deciphering conventional MRI changes with the potential to deepen our comprehension of MS neuropathology and identify novel imaging biomarkers (177). In this context, T_1 relaxometry offers quantitative information on the micro- and macrostructural integrity of soft body tissues (177-179). It was also reported to be superior when analyzing Gd retention within the CNS (71, 132), however, most MRI studies cited in this thesis investigated Gd retention via semi-quantitative analysis of SI ratio changes in unenhanced T_1-weighted scans of patients with MS (16, 72, 73, 77, 172) or without (15, 16, 18, 21, 48) as well as in rodents (22, 26, 49, 176). Despite their potential, quantitative MRI techniques are not regularly used in clinical practice yet (180).

The main drivers of T_1 changes in brain MRI of MS patients include water, macromolecules such as myelin, and Fe content (180). A decrease in T_1 implies reduced water content, Fe accumulation, and augmented macromolecular density, while an increase implies the opposite (177, 180). Fe accumulation has been detected inside the DN and other gray matter regions of MS brains, correlating with disease severity (181). Our study was unable to confirm this association, possibly due to incomplete perfusion of the mouse body during sacrifice, resulting in residual Fe-rich blood within brains and subsequent inaccuracies in Fe intensity. MS pathology was further linked to increased T_1 values in focal demyelinating lesions (177, 182) and broader disease processes affecting normal-appearing white and grey matter (183). Our study compared T_1 values of HC cerebella to EAE during peak disability (MRI baseline), revealing slightly higher T_1 in EAE, likely attributable to neuroinflammatory processes. However, the administration of GBCAs led to relevant shortening of T_1 in both HC and EAE brains, with a more pronounced effect in EAE. In the brains of MS patients, T_1 shortening correlated dose-dependently with previous linear GBCA injections, but not with disease duration or clinical severity (EDSS) (71, 131). Consistently, cerebellar T_1 values of EAE mice in our study correlated significantly with retained Gd concentrations but not with the EAE score. Furthermore, Gd retention did not spatially coincide with focal demyelination in our study, as observed through LA-ICP-MS and consecutive H&E-stained brain sections, indicating that it may rather be linked to more disseminated inflammatory processes in EAE brains.

4.5 Limitations of the study

We used the well-established EAE mouse model to investigate Gd retention in the context of neuroinflammation, which recapitulates the main pathophysiological hallmarks of MS but does not reflect its entire spectrum of disease heterogeneity (85). The experimental design, including frequency and daily GBCA doses, differed significantly from the situation in clinical practice. However, rodent models have proven to be valuable in the investigation of Gd retention under controlled conditions (25, 26, 80, 114, 159), helping to eliminate sources of variation like heterogenous time points and types of GBCA applied (82). Another limiting factor is the missing inclusion of sham-immunized controls, allowing no differentiation between EAE-specific neuroinflammation and general inflammatory processes attributable to a reaction to the CFA adjuvants.

The sample size of 2 mice per group for LA-ICP-MS, ICP-MS, IMC, and *in vitro* MRI experiments did not allow for a quantitative, statistically valid conclusion on Gd retention during neuroinflammation, but our data demonstrated very consistent trends of increased retention levels in EAE compared to HC brains. The assessment of Gd retention in chronic hippocampal slices using IMC was compromised by inaccuracies arising from repeated washing steps. These steps potentially led to the removal of intact GBCA, resulting in an underestimation of total Gd content, especially after gadobutrol treatment. However, ICP-MS overcame the semi-quantitative and potentially imprecise character of IMC. Moreover, the limited local resolution of LA-ICP-MS hindered the visualization of EAE lesions, but we used adjacent H&E-stained cerebellar tissue sections for the localization of sites of mononuclear cell infiltration.

The presented study provides valuable information on the magnitude, distribution pattern, and long-term character of inflammation-promoted Gd deposits after repeated injection of linear gadopentetate and macrocyclic gadobutrol in mice. Observed differences in the permanency of retention of linear and macrocyclic GBCAs are translatable to the human situation as shown similarly in clinical trials using quantitative techniques for Gd detection (29-33). To increase the external validity of results, it will be of particular interest to examine the impact of neuroinflammation on Gd retention in longitudinal human studies.

4.6 Implications for clinical practice and future directions

The overarching future objective is to gain a comprehensive understanding of distinct histopathological substrates underlying MRI findings, providing biologically relevant insights into various disease aspects of MS. Moving forward, it is crucial to explore the mechanisms underpinning sustained GBCA enhancement and Gd retention, and closely examine transchelation processes involving GAG accumulation during inflammation. The rate of transchelation could potentially serve as an indicator of the activation state of the ECM during inflammation. Studying the dynamic binding of Gd^{3+} to ECM components could offer insights into inflammatory processes inside the body (184), advance understanding of ECM involvement in MS pathology, and help to identify new disease-related biomarkers. In this line, a recently utilized peptide-conjugated GBCA-based molecular MRI probe successfully targeted fibrin in EAE mouse brains. It detected fibrin accumulation in perivascular and subarachnoid spaces, which was associated with leucocyte infiltration and demyelination, and correlated with the clinical disability (185).

The translational potential of the quantification of Gd retention inside the CNS represents a considerable strength of *in vivo* T_1 relaxometry studies. We confirmed that T_1 shortening correlated significantly with retained Gd concentrations detected by LA-ICP-MS inside the cerebellum. Thus, T_1 mapping may offer a valuable tool for the longitudinal monitoring of Gd brain retention without the need for tissue assessments. Nevertheless, T_1 relaxometry may be limited in the detection of insoluble Gd deposits. We are currently utilizing electron paramagnetic resonance spectroscopy to further explore Gd bindings and their microenvironment. In addition, IMC measurements could help to elucidate whether Gd deposits colocalize with focal lesions or specific tissue-resident cells, immune cell infiltrates, or ECM components.

While consistent clinical correlates of Gd retention in humans are still lacking, the ongoing debate on potential GBCA toxicity highlights the limitations of single-cell experiments in fully characterizing the effects of GBCAs due to the absence of ECM components, vessels, and cellular interactions (160, 163). Instead, organotypic brain slices preserve the three-dimensional parenchymal architecture and function (120) of the tissue, as well as its responsiveness to inflammatory stimuli (186). Providing excellent long-term survival, it may serve as a platform for controlled and repeated substance testing, bridging the gap between cell lines and *in vivo* models. It enables several substance concentrations to be evaluated on tissue slices from a single mouse, reducing the number of experimental animals according to the 3R principle (88). Using this model, we are currently assessing changes in mitochondrial dynamics in 2 min. time lapses after incubation with linear and macrocyclic GBCAs. The transgenic mouse strain B6.Cg-Tg(Thy1-CFP/COX8A)S2Lich/J expresses the neuronal cyan fluorescent protein (CFP), coupled to a human cytochrome c oxidase subunit 8A, under control of the Thy1 promoter gene (187). CFP is specifically expressed in neuronal mitochondria, allowing for the detection of mitochondrial alterations using fluorescence microscopy. In a first approach, we observed that 50 mM of gadopentetate led to the rounding of mitochondria in surviving neurons, which moved at higher speed during additional TNFα treatment. Our preliminary results agree with the study by Malla *et al.* on oxidative stress-induced mitochondrial alterations in acute brain slices (188), indicating that abnormal ROS accumulation and mitochondrial dysfunction contribute to neuronal cell death after GBCA treatment.

5 Conclusion

This thesis investigates the impact of neuroinflammation on Gd brain retention and Gd-induced neurotoxicity after multiple administrations of linear gadopentetate and macrocyclic gadobutrol in the EAE mouse model and *ex vivo*. Our results indicate that inflammation facilitates the cerebellar long-term retention of Gd following gadopentetate administration. Gd retention after gadobutrol application was initially promoted by inflammation to a comparable relative extent, but overall was only transient. We suggest that BBB disruption during neuroinflammation allows an additional uptake of both GBCAs into the brain. Once retained, gadobutrol was continuously cleared from the parenchyma, while gadopentetate was not, most likely due to the formation of soluble and insoluble Gd species. Permanent cerebellar Gd deposition after gadopentetate application was restricted to the CN of HC brains, while in EAE cerebella, it extended to cortical areas. We speculate that local changes in endogenous metals and modifications in the composition and sulfation of macromolecules with chelating abilities contribute to this augmented and expanded long-term retention of Gd during neuroinflammation.

We believe that the persistence of Gd retention and the associated toxic potential depends on a GBCA's specific kinetic and thermodynamic stability, which may be affected by a pro-inflammatory environment. The fact that gadobutrol treatment did not cause relevant permanent Gd deposition or neurocytotoxic effects indicates that it mostly remained as intact chelate. As observed in this study, administration of gadopentetate can lead to the induction of cytotoxic effects, possibly due to dissociation and the formation of permanent Gd tissue bindings, particularly during inflammation. We also propose that recirculation and uptake of Gd^{3+} from the blood into the CNS may intensify brain Gd retention in the long term, potentially contributing to delayed neurotoxicity. Although the Gd retention levels measured *in vivo* were below the cytotoxic values determined *ex vivo*, we cannot exclude the possibility that multiple injections of particularly linear GBCAs in patients with neuroinflammatory conditions such as MS may lead to cumulative Gd deposits with deferred neurotoxic potential.

Reference list

1. Hao D, Ai T, Goerner F, Hu X, Runge VM, Tweedle M. MRI contrast agents: basic chemistry and safety. Journal of magnetic resonance imaging : JMRI. 2012;36(5):1060-71.
2. Lohrke J, Frenzel T, Endrikat J, Alves FC, Grist TM, Law M, Lee JM, Leiner T, Li KC, Nikolaou K, Prince MR, Schild HH, Weinreb JC, Yoshikawa K, Pietsch H. 25 Years of Contrast-Enhanced MRI: Developments, Current Challenges and Future Perspectives. Adv Ther. 2016;33(1):1-28.
3. Aime S, Caravan P. Biodistribution of gadolinium-based contrast agents, including gadolinium deposition. Journal of magnetic resonance imaging : JMRI. 2009;30(6):1259-67.
4. Murata N, Murata K, Gonzalez-Cuyar LF, Maravilla KR. Gadolinium tissue deposition in brain and bone. Magnetic resonance imaging. 2016;34(10):1359-65.
5. Matsumura T, Hayakawa M, Shimada F, Yabuki M, Dohanish S, Palkowitsch P, Yoshikawa K. Safety of gadopentetate dimeglumine after 120 million administrations over 25 years of clinical use. Magnetic resonance in medical sciences : MRMS : an official journal of Japan Society of Magnetic Resonance in Medicine. 2013;12(4):297-304.
6. Hunt CH, Hartman RP, Hesley GK. Frequency and severity of adverse effects of iodinated and gadolinium contrast materials: retrospective review of 456,930 doses. AJR Am J Roentgenol. 2009;193(4):1124-7.
7. Knopp MV, Balzer T, Esser M, Kashanian FK, Paul P, Niendorf HP. Assessment of utilization and pharmacovigilance based on spontaneous adverse event reporting of gadopentetate dimeglumine as a magnetic resonance contrast agent after 45 million administrations and 15 years of clinical use. Investigative radiology. 2006;41(6):491-9.
8. Rydahl C, Thomsen HS, Marckmann P. High prevalence of nephrogenic systemic fibrosis in chronic renal failure patients exposed to gadodiamide, a gadolinium-containing magnetic resonance contrast agent. Investigative radiology. 2008;43(2):141-4.
9. Grobner T. Gadolinium--a specific trigger for the development of nephrogenic fibrosing dermopathy and nephrogenic systemic fibrosis? Nephrology, dialysis, transplantation : official publication of the European Dialysis and Transplant Association - European Renal Association. 2006;21(4):1104-8.
10. Sieber MA, Lengsfeld P, Frenzel T, Golfier S, Schmitt-Willich H, Siegmund F, Walter J, Weinmann HJ, Pietsch H. Preclinical investigation to compare different gadolinium-based contrast agents regarding their propensity to release gadolinium in vivo and to trigger nephrogenic systemic fibrosis-like lesions. European radiology. 2008;18(10):2164-73.
11. Rasschaert M, Idée JM, Robert P, Fretellier N, Vives V, Violas X, Ballet S, Corot C. Moderate Renal Failure Accentuates T1 Signal Enhancement in the Deep Cerebellar Nuclei of Gadodiamide-Treated Rats. Investigative radiology. 2017;52(5):255-64.
12. Fretellier N, Idée JM, Dencausse A, Karroum O, Guerret S, Poveda N, Jestin G, Factor C, Raynal I, Zamia P, Port M, Corot C. Comparative in vivo dissociation of gadolinium chelates in renally impaired rats: a relaxometry study. Investigative radiology. 2011;46(5):292-300.
13. Do QN, Lenkinski RE, Tircso G, Kovacs Z. How the Chemical Properties of GBCAs Influence Their Safety Profiles In Vivo. Molecules. 2021;27(1).
14. Runge VM. Dechelation (Transmetalation): Consequences and Safety Concerns With the Linear Gadolinium-Based Contrast Agents, In View of Recent Health Care Rulings by the EMA (Europe), FDA (United States), and PMDA (Japan). Investigative radiology. 2018;53(10):571-8.
15. Kanda T, Ishii K, Kawaguchi H, Kitajima K, Takenaka D. High signal intensity in the dentate nucleus and globus pallidus on unenhanced T1-weighted MR images: relationship with increasing cumulative dose of a gadolinium-based contrast material. Radiology. 2014;270(3):834-41.
16. Errante Y, Cirimele V, Mallio CA, Di Lazzaro V, Zobel BB, Quattrocchi CC. Progressive increase of T1 signal intensity of the dentate nucleus on unenhanced magnetic resonance images is associated with cumulative doses of intravenously administered gadodiamide in patients with normal renal function, suggesting dechelation. Investigative radiology. 2014;49(10):685-90.
17. Quattrocchi CC, Mallio CA, Errante Y, Cirimele V, Carideo L, Ax A, Zobel BB. Gadodiamide and Dentate Nucleus T1 Hyperintensity in Patients With Meningioma Evaluated by Multiple Follow-Up Contrast-Enhanced Magnetic Resonance Examinations With No Systemic Interval Therapy. Investigative radiology. 2015;50(7):470-2.
18. Weberling LD, Kieslich PJ, Kickingereder P, Wick W, Bendszus M, Schlemmer HP, Radbruch A. Increased Signal Intensity in the Dentate Nucleus on Unenhanced T1-Weighted Images After Gadobenate Dimeglumine Administration. Investigative radiology. 2015;50(11):743-8.

19. Ramalho J, Castillo M, AlObaidy M, Nunes RH, Ramalho M, Dale BM, Semelka RC. High Signal Intensity in Globus Pallidus and Dentate Nucleus on Unenhanced T1-weighted MR Images: Evaluation of Two Linear Gadolinium-based Contrast Agents. Radiology. 2015;276(3):836-44.
20. Cao Y, Huang DQ, Shih G, Prince MR. Signal Change in the Dentate Nucleus on T1-Weighted MR Images After Multiple Administrations of Gadopentetate Dimeglumine Versus Gadobutrol. AJR Am J Roentgenol. 2016;206(2):414-9.
21. Kanda T, Osawa M, Oba H, Toyoda K, Kotoku J, Haruyama T, Takeshita K, Furui S. High Signal Intensity in Dentate Nucleus on Unenhanced T1-weighted MR Images: Association with Linear versus Macrocyclic Gadolinium Chelate Administration. Radiology. 2015;275(3):803-9.
22. Robert P, Lehericy S, Grand S, Violas X, Fretellier N, Idee JM, Ballet S, Corot C. T1-Weighted Hypersignal in the Deep Cerebellar Nuclei After Repeated Administrations of Gadolinium-Based Contrast Agents in Healthy Rats: Difference Between Linear and Macrocyclic Agents. Investigative radiology. 2015;50(8):473-80.
23. Robert P, Violas X, Grand S, Lehericy S, Idee JM, Ballet S, Corot C. Linear Gadolinium-Based Contrast Agents Are Associated With Brain Gadolinium Retention in Healthy Rats. Investigative radiology. 2016;51(2):73-82.
24. Frenzel T, Apte C, Jost G, Schockel L, Lohrke J, Pietsch H. Quantification and Assessment of the Chemical Form of Residual Gadolinium in the Brain After Repeated Administration of Gadolinium-Based Contrast Agents: Comparative Study in Rats. Investigative radiology. 2017;52(7):396-404.
25. Lohrke J, Frisk AL, Frenzel T, Schöckel L, Rosenbruch M, Jost G, Lenhard DC, Sieber MA, Nischwitz V, Küppers A, Pietsch H. Histology and Gadolinium Distribution in the Rodent Brain After the Administration of Cumulative High Doses of Linear and Macrocyclic Gadolinium-Based Contrast Agents. Investigative radiology. 2017;52(6):324-33.
26. Jost G, Frenzel T, Boyken J, Lohrke J, Nischwitz V, Pietsch H. Long-term Excretion of Gadolinium-based Contrast Agents: Linear versus Macrocyclic Agents in an Experimental Rat Model. Radiology. 2019;290(2):340-8.
27. Di Gregorio E, Furlan C, Atlante S, Stefania R, Gianolio E, Aime S. Gadolinium Retention in Erythrocytes and Leukocytes From Human and Murine Blood Upon Treatment With Gadolinium-Based Contrast Agents for Magnetic Resonance Imaging. Investigative radiology. 2020;55(1):30-7.
28. Davies J, Marino M, Smith APL, Crowder JM, Larsen M, Lowery L, Castle J, Hibberd MG, Evans PM. Repeat and single dose administration of gadodiamide to rats to investigate concentration and location of gadolinium and the cell ultrastructure. Scientific reports. 2021;11(1):13950.
29. McDonald RJ, McDonald JS, Kallmes DF, Jentoft ME, Murray DL, Thielen KR, Williamson EE, Eckel LJ. Intracranial Gadolinium Deposition after Contrast-enhanced MR Imaging. Radiology. 2015;275(3):772-82.
30. Kanda T, Fukusato T, Matsuda M, Toyoda K, Oba H, Kotoku J, Haruyama T, Kitajima K, Furui S. Gadolinium-based Contrast Agent Accumulates in the Brain Even in Subjects without Severe Renal Dysfunction: Evaluation of Autopsy Brain Specimens with Inductively Coupled Plasma Mass Spectroscopy. Radiology. 2015;276(1):228-32.
31. McDonald RJ, McDonald JS, Kallmes DF, Jentoft ME, Paolini MA, Murray DL, Williamson EE, Eckel LJ. Gadolinium Deposition in Human Brain Tissues after Contrast-enhanced MR Imaging in Adult Patients without Intracranial Abnormalities. Radiology. 2017;285(2):546-54.
32. Roberts DR, Welsh CA, LeBel DP, 2nd, Davis WC. Distribution map of gadolinium deposition within the cerebellum following GBCA administration. Neurology. 2017;88(12):1206-8.
33. Fingerhut S, Sperling M, Holling M, Niederstadt T, Allkemper T, Radbruch A, Heindel W, Paulus W, Jeibmann A, Karst U. Gadolinium-based contrast agents induce gadolinium deposits in cerebral vessel walls, while the neuropil is not affected: an autopsy study. Acta Neuropathol. 2018;136(1):127-38.
34. Frenzel T, Lengsfeld P, Schirmer H, Hutter J, Weinmann HJ. Stability of gadolinium-based magnetic resonance imaging contrast agents in human serum at 37 degrees C. Investigative radiology. 2008;43(12):817-28.
35. Port M, Idee JM, Medina C, Robic C, Sabatou M, Corot C. Efficiency, thermodynamic and kinetic stability of marketed gadolinium chelates and their possible clinical consequences: a critical review. Biometals: an international journal on the role of metal ions in biology, biochemistry, and medicine. 2008;21(4):469-90.
36. Radbruch A. Gadolinium Deposition in the Brain: We Need to Differentiate between Chelated and Dechelated Gadolinium. Radiology. 2018:180294.
37. Idée JM, Port M, Raynal I, Schaefer M, Le Greneur S, Corot C. Clinical and biological consequences of transmetallation induced by contrast agents for magnetic resonance imaging: a review. Fundam Clin Pharmacol. 2006;20(6):563-76.

38. Rasschaert M, Emerit A, Fretellier N, Factor C, Robert P, Idée JM, Corot C. Gadolinium Retention, Brain T1 Hyperintensity, and Endogenous Metals: A Comparative Study of Macrocyclic Versus Linear Gadolinium Chelates in Renally Sensitized Rats. Investigative radiology. 2018;53(6):328-37.
39. Telgmann L, Wehe CA, Kunnemeyer J, Bulter AC, Sperling M, Karst U. Speciation of Gd-based MRI contrast agents and potential products of transmetalation with iron ions or parenteral iron supplements. Analytical and bioanalytical chemistry. 2012;404(8):2133-41.
40. Laurent S, Elst LV, Copoix F, Muller RN. Stability of MRI paramagnetic contrast media: a proton relaxometric protocol for transmetallation assessment. Investigative radiology. 2001;36(2):115-22.
41. Thakral C, Abraham JL. Gadolinium-induced nephrogenic systemic fibrosis is associated with insoluble Gd deposits in tissues: in vivo transmetallation confirmed by microanalysis. J Cutan Pathol. 2009;36(12):1244-54.
42. Boyken J, Frenzel T, Lohrke J, Jost G, Schütz G, Pietsch H. Impact of Treatment With Chelating Agents Depends on the Stability of Administered GBCAs: A Comparative Study in Rats. Investigative radiology. 2019;54(2):76-82.
43. Werner P, Taupitz M, Schröder L, Schuenke P. An NMR relaxometry approach for quantitative investigation of the transchelation of gadolinium ions from GBCAs to a competing macromolecular chelator. Scientific reports. 2021;11(1):21731.
44. Bussi S, Coppo A, Botteron C, Fraimbault V, Fanizzi A, De Laurentiis E, Colombo Serra S, Kirchin MA, Tedoldi F, Maisano F. Differences in gadolinium retention after repeated injections of macrocyclic MR contrast agents to rats. Journal of magnetic resonance imaging : JMRI. 2018;47(3):746-52.
45. Bussi S, Coppo A, Celeste R, Fanizzi A, Fringuello Mingo A, Ferraris A, Botteron C, Kirchin MA, Tedoldi F, Maisano F. Macrocyclic MR contrast agents: evaluation of multiple-organ gadolinium retention in healthy rats. Insights Imaging. 2020;11(1):11.
46. Frenzel T, Ulbrich HF, Pietsch H. The Macrocyclic Gadolinium-Based Contrast Agents Gadobutrol and Gadoteridol Show Similar Elimination Kinetics From the Brain After Repeated Intravenous Injections in Rabbits. Investigative radiology. 2021;56(6):341-7.
47. Strzeminska I, Factor C, Robert P, Grindel AL, Comby PO, Szpunar J, Corot C, Lobinski R. Long-Term Evaluation of Gadolinium Retention in Rat Brain After Single Injection of a Clinically Relevant Dose of Gadolinium-Based Contrast Agents. Investigative radiology. 2020;55(3):138-43.
48. Radbruch A, Haase R, Kieslich PJ, Weberling LD, Kickingereder P, Wick W, Schlemmer HP, Bendszus M. No Signal Intensity Increase in the Dentate Nucleus on Unenhanced T1-weighted MR Images after More than 20 Serial Injections of Macrocyclic Gadolinium-based Contrast Agents. Radiology. 2017;282(3):699-707.
49. Robert P, Fingerhut S, Factor C, Vives V, Letien J, Sperling M, Rasschaert M, Santus R, Ballet S, Idee JM, Corot C, Karst U. One-year Retention of Gadolinium in the Brain: Comparison of Gadodiamide and Gadoterate Meglumine in a Rodent Model. Radiology. 2018:172746.
50. Strzeminska I, Factor C, Robert P, Szpunar J, Corot C, Lobinski R. Speciation Analysis of Gadolinium in the Water-Insoluble Rat Brain Fraction After Administration of Gadolinium-Based Contrast Agents. Investigative radiology. 2021;56(9):535-44.
51. Strzeminska I, Factor C, Jimenez-Lamana J, Lacomme S, Subirana MA, Le Coustumer P, Schaumlöffel D, Robert P, Szpunar J, Corot C, Lobinski R. Comprehensive Speciation Analysis of Residual Gadolinium in Deep Cerebellar Nuclei in Rats Repeatedly Administered With Gadoterate Meglumine or Gadodiamide. Investigative radiology. 2022.
52. Agency EM. EMA's final opinion confirms restrictions on use of linear gadolin- ium agents in body scan. . 2017:23.
53. Administration USFaD. FDA warns that gadolinium-based contrast agents (GBCAs) are retained in the body; requires new class warnings. December 19, 2017.
54. Radbruch A, Richter H, Bücker P, Berlandi J, Schänzer A, Deike-Hofmann K, Kleinschnitz C, Schlemmer HP, Forsting M, Paulus W, Martin LF, van Thriel C, Karst U, Jeibmann A. Is Small Fiber Neuropathy Induced by Gadolinium-Based Contrast Agents? Invest radiol. 2020;55(8):473-80.
55. Ramalho J, Ramalho M. Gadolinium Deposition and Chronic Toxicity. Magn Reson Imaging Clin N Am. 2017;25(4):765-78.
56. Chehabeddine L, Al Saleh T, Baalbaki M, Saleh E, Khoury SJ, Hannoun S. Cumulative administrations of gadolinium-based contrast agents: risks of accumulation and toxicity of linear vs macrocyclic agents. Critical reviews in toxicology. 2019;49(3):262-79.
57. Mey GM, Mahajan KR, DeSilva TM. Neurodegeneration in multiple sclerosis. WIREs Mech Dis. 2023;15(1):e1583.
58. Liu R, Du S, Zhao L, Jain S, Sahay K, Rizvanov A, Lezhnyova V, Khaibullin T, Martynova E, Khaiboullina S, Baranwal M. Autoreactive lymphocytes in multiple sclerosis: Pathogenesis and treatment target. Front Immunol. 2022;13:996469.

59. Engelhardt B, Comabella M, Chan A. Multiple sclerosis: Immunopathological heterogeneity and its implications. European journal of immunology. 2022;52(6):869-81.
60. Balasa R, Barcutean L, Mosora O, Manu D. Reviewing the Significance of Blood-Brain Barrier Disruption in Multiple Sclerosis Pathology and Treatment. Int J Mol Sci. 2021;22(16).
61. Spencer JI, Bell JS, DeLuca GC. Vascular pathology in multiple sclerosis: reframing pathogenesis around the blood-brain barrier. J Neurol Neurosurg Psychiatry. 2018;89(1):42-52.
62. Giorgio A, De Stefano N. Effective Utilization of MRI in the Diagnosis and Management of Multiple Sclerosis. Neurol Clin. 2018;36(1):27-34.
63. Thompson AJ, Banwell BL, Barkhof F, Carroll WM, Coetzee T, Comi G, Correale J, Fazekas F, Filippi M, Freedman MS. Diagnosis of multiple sclerosis: 2017 revisions of the McDonald criteria. The Lancet Neurology. 2018;17(2):162-73.
64. Tommasin S, Giannì C, De Giglio L, Pantano P. Neuroimaging Techniques to Assess Inflammation in Multiple Sclerosis. Neuroscience. 2019;403:4-16.
65. Absinta M, Sati P, Reich DS. Advanced MRI and staging of multiple sclerosis lesions. Nat Rev Neurol. 2016;12(6):358-68.
66. McDonald WI, Compston A, Edan G, Goodkin D, Hartung HP, Lublin FD, McFarland HF, Paty DW, Polman CH, Reingold SC, Sandberg-Wollheim M, Sibley W, Thompson A, van den Noort S, Weinshenker BY, Wolinsky JS. Recommended diagnostic criteria for multiple sclerosis: guidelines from the International Panel on the diagnosis of multiple sclerosis. Annals of neurology. 2001;50(1):121-7.
67. Polman CH, Reingold SC, Banwell B, Clanet M, Cohen JA, Filippi M, Fujihara K, Havrdova E, Hutchinson M, Kappos L, Lublin FD, Montalban X, O'Connor P, Sandberg-Wollheim M, Thompson AJ, Waubant E, Weinshenker B, Wolinsky JS. Diagnostic criteria for multiple sclerosis: 2010 revisions to the McDonald criteria. Annals of neurology. 2011;69(2):292-302.
68. Polman CH, Reingold SC, Edan G, Filippi M, Hartung HP, Kappos L, Lublin FD, Metz LM, McFarland HF, O'Connor PW, Sandberg-Wollheim M, Thompson AJ, Weinshenker BG, Wolinsky JS. Diagnostic criteria for multiple sclerosis: 2005 revisions to the "McDonald Criteria". Annals of neurology. 2005;58(6):840-6.
69. Wattjes MP, Ciccarelli O, Reich DS, Banwell B, de Stefano N, Enzinger C, Fazekas F, Filippi M, Frederiksen J, Gasperini C, Hacohen Y, Kappos L, Li DKB, Mankad K, Montalban X, Newsome SD, Oh J, Palace J, Rocca MA, Sastre-Garriga J, Tintoré M, Traboulsee A, Vrenken H, Yousry T, Barkhof F, Rovira À. 2021 MAGNIMS-CMSC-NAIMS consensus recommendations on the use of MRI in patients with multiple sclerosis. The Lancet Neurology. 2021;20(8):653-70.
70. Roccatagliata L, Vuolo L, Bonzano L, Pichiecchio A, Mancardi GL. Multiple sclerosis: hyperintense dentate nucleus on unenhanced T1-weighted MR images is associated with the secondary progressive subtype. Radiology. 2009;251(2):503-10.
71. Tedeschi E, Palma G, Canna A, Cocozza S, Russo C, Borrelli P, Lanzillo R, Angelini V, Postiglione E, Morra VB, Salvatore M, Brunetti A, Quarantelli M. In vivo dentate nucleus MRI relaxometry correlates with previous administration of Gadolinium-based contrast agents. European radiology. 2016;26(12):4577-84.
72. Schlemm L, Chien C, Bellmann-Strobl J, Dorr J, Wuerfel J, Brandt AU, Paul F, Scheel M. Gadopentetate but not gadobutrol accumulates in the dentate nucleus of multiple sclerosis patients. Multiple sclerosis (Houndmills, Basingstoke, England). 2017;23(7):963-72.
73. Malhotra A, LeSar B, Wu X, Durand D, Das N, Anzai Y, Sanelli P. Progressive T1 Shortening of the Dentate Nucleus in Patients With Multiple Sclerosis: Result of Multiple Administrations of Linear Gadolinium Contrast Agents Versus Intrinsic Disease. AJR Am J Roentgenol. 2018;211(5):1099-105.
74. Kang H, Hii M, Le M, Tam R, Riddehough A, Traboulsee A, Kolind S, Freedman MS, Li DKB. Gadolinium Deposition in Deep Brain Structures: Relationship with Dose and Ionization of Linear Gadolinium-Based Contrast Agents. AJNR American journal of neuroradiology. 2018;39(9):1597-603.
75. Eisele P, Szabo K, Ebert A, Radbruch A, Platten M, Schoenberg SO, Gass A. Diffusion-weighted imaging of the dentate nucleus after repeated application of gadolinium-based contrast agents in multiple sclerosis. Magnetic resonance imaging. 2019;58:1-5.
76. Stojanov DA, Aracki-Trenkic A, Vojinovic S, Benedeto-Stojanov D, Ljubisavljevic S. Increasing signal intensity within the dentate nucleus and globus pallidus on unenhanced T1W magnetic resonance images in patients with relapsing-remitting multiple sclerosis: correlation with cumulative dose of a macrocyclic gadolinium-based contrast agent, gadobutrol. European radiology. 2016;26(3):807-15.
77. Splendiani A, Perri M, Marsecano C, Vellucci V, Michelini G, Barile A, Di Cesare E. Effects of serial macrocyclic-based contrast materials gadoterate meglumine and gadobutrol administrations on gadolinium-related dentate nuclei signal increases in unenhanced T1-weighted brain: a retrospective study in 158 multiple sclerosis (MS) patients. Radiol Med. 2018;123(2):125-34.

78. Agris J, Pietsch H, Balzer T. What Evidence Is There That Gadobutrol Causes Increasing Signal Intensity within the Dentate Nucleus and Globus Pallidus on Unenhanced T1W MRI in Patients with RRMS? European radiology. 2016;26(3):816-7.
79. Jaulent P, Hannoun S, Kocevar G, Rollot F, Durand-Dubief F, Vukusic S, Brisset JC, Sappey-Marinier D, Cotton F. Weekly enhanced T1-weighted MRI with Gadobutrol injections in MS patients: Is there a signal intensity increase in the dentate nucleus and the globus pallidus? European journal of radiology. 2018;105:204-8.
80. Wang S, Hesse B, Roman M, Stier D, Castillo-Michel H, Cotte M, Suuronen JP, Lagrange A, Radbruch H, Paul F, Taupitz M, Schellenberger E, Sack I, Infante-Duarte C. Increased Retention of Gadolinium in the Inflamed Brain After Repeated Administration of Gadopentetate Dimeglumine: A Proof-of-Concept Study in Mice Combining ICP-MS and Micro- and Nano-SR-XRF. Investigative radiology. 2019;54(10):617-26.
81. Anderhalten L, Silva RV, Morr A, Wang S, Smorodchenko A, Saatz J, Traub H, Mueller S, Boehm-Sturm P, Rodriguez-Sillke Y, Kunkel D, Hahndorf J, Paul F, Taupitz M, Sack I, Infante-Duarte C. Different Impact of Gadopentetate and Gadobutrol on Inflammation-Promoted Retention and Toxicity of Gadolinium Within the Mouse Brain. Investigative radiology. 2022;57(10):677-88.
82. Constantinescu CS, Farooqi N, O'Brien K, Gran B. Experimental autoimmune encephalomyelitis (EAE) as a model for multiple sclerosis (MS). Br J Pharmacol. 2011;164(4):1079-106.
83. Robinson AP, Harp CT, Noronha A, Miller SD. The experimental autoimmune encephalomyelitis (EAE) model of MS: utility for understanding disease pathophysiology and treatment. Handb Clin Neurol. 2014;122:173-89.
84. Kipp M, Nyamoya S, Hochstrasser T, Amor S. Multiple sclerosis animal models: a clinical and histopathological perspective. Brain pathology (Zurich, Switzerland). 2017;27(2):123-37.
85. Procaccini C, De Rosa V, Pucino V, Formisano L, Matarese G. Animal models of Multiple Sclerosis. Eur J Pharmacol. 2015;759:182-91.
86. Glatigny S, Bettelli E. Experimental Autoimmune Encephalomyelitis (EAE) as Animal Models of Multiple Sclerosis (MS). Cold Spring Harb Perspect Med. 2018;8(11).
87. Miller SD, Karpus WJ, Davidson TS. Experimental autoimmune encephalomyelitis in the mouse. Curr Protoc Immunol. 2010;Chapter 15:15.1.1-.1.20.
88. Díaz L, Zambrano E, Flores ME, Contreras M, Crispín JC, Alemán G, Bravo C, Armenta A, Valdés VJ, Tovar A, Gamba G, Barrios-Payán J, Bobadilla NA. Ethical Considerations in Animal Research: The Principle of 3R's. Rev Invest Clin. 2020;73(4):199-209.
89. Rasschaert M, Weller RO, Schroeder JA, Brochhausen C, Idée JM. Retention of Gadolinium in Brain Parenchyma: Pathways for Speciation, Access, and Distribution. A Critical Review. Journal of magnetic resonance imaging : JMRI. 2020;52(5):1293-305.
90. Weidman EK, Dean KE, Rivera W, Loftus ML, Stokes TW, Min RJ. MRI safety: a report of current practice and advancements in patient preparation and screening. Clin Imaging. 2015;39(6):935-7.
91. Bloch F. Nuclear induction. Phys Rev. 1946;70(7–8):460–74.
92. Bloembergen N, Purcell EM, Pound RV. Relaxation effects in nuclear magnetic resonance absorption. Phys Rev. 1948;73(7):679–712.
93. Grover VP, Tognarelli JM, Crossey MM, Cox IJ, Taylor-Robinson SD, McPhail MJ. Magnetic Resonance Imaging: Principles and Techniques: Lessons for Clinicians. J Clin Exp Hepatol. 2015;5(3):246-55.
94. Minhas AS, Oliver R. Magnetic Resonance Imaging Basics. Adv Exp Med Biol. 2022;1380:47-82.
95. Ibrahim MA, Hazhirkarzar B, Dublin AB. Gadolinium Magnetic Resonance Imaging. StatPearls. Treasure Island (FL): StatPearls Publishing

Copyright © 2022, StatPearls Publishing LLC.; 2022.

96. Taylor AJ, Salerno M, Dharmakumar R, Jerosch-Herold M. T1 Mapping: Basic Techniques and Clinical Applications. JACC Cardiovasc Imaging. 2016;9(1):67-81.
97. Fernandes JL, Rochitte CE. T1 mapping: technique and applications. Magn Reson Imaging Clin N Am. 2015;23(1):25-34.
98. Denic A, Macura SI, Mishra P, Gamez JD, Rodriguez M, Pirko I. MRI in rodent models of brain disorders. Neurotherapeutics. 2011;8(1):3-18.
99. van de Looij Y, Vasung L, Sizonenko SV, Hüppi PS. MRI of animal models of developmental disorders and translation to human imaging. Current opinion in neurology. 2014;27(2):157-67.
100. Wachsmuth L, Mensen A, Barca C, Wiart M, Tristão-Pereira C, Busato A, Waiczies S, Himmelreich U, Millward JM, Reimann HM, Jelescu I, Marzola P, Pradier B, Viola A, Faber C. Contribution of preclinical MRI to responsible animal research: living up to the 3R principle. Magma. 2021;34(4):469-74.
101. Prescott MJ, Poirier C. The role of MRI in applying the 3Rs to non-human primate neuroscience. NeuroImage. 2021;225:117521.

102. Koch S, Mueller S, Foddis M, Bienert T, von Elverfeldt D, Knab F, Farr TD, Bernard R, Dopatka M, Rex A, Dirnagl U, Harms C, Boehm-Sturm P. Atlas registration for edema-corrected MRI lesion volume in mouse stroke models. J Cereb Blood Flow Metab. 2019;39(2):313-23.
103. Millward JM, Ramos Delgado P, Smorodchenko A, Boehmert L, Periquito J, Reimann HM, Prinz C, Els A, Scheel M, Bellmann-Strobl J, Waiczies H, Wuerfel J, Infante-Duarte C, Chien C, Kuchling J, Pohlmann A, Zipp F, Paul F, Niendorf T, Waiczies S. Transient enlargement of brain ventricles during relapsing-remitting multiple sclerosis and experimental autoimmune encephalomyelitis. JCI Insight. 2020;5(21).
104. Fischer AH, Jacobson KA, Rose J, Zeller R. Hematoxylin and eosin staining of tissue and cell sections. CSH Protoc. 2008;2008:pdb.prot4986.
105. Pröfrock D, Prange A. Inductively coupled plasma-mass spectrometry (ICP-MS) for quantitative analysis in environmental and life sciences: a review of challenges, solutions, and trends. Appl Spectrosc. 2012;66(8):843-68.
106. Clases D, Gonzalez de Vega R. Facets of ICP-MS and their potential in the medical sciences-Part 1: fundamentals, stand-alone and hyphenated techniques. Analytical and bioanalytical chemistry. 2022;414(25):7337-61.
107. Rodushkin I, Engström E, Baxter DC. Isotopic analyses by ICP-MS in clinical samples. Analytical and bioanalytical chemistry. 2013;405(9):2785-97.
108. Darrah TH, Prutsman-Pfeiffer JJ, Poreda RJ, Ellen Campbell M, Hauschka PV, Hannigan RE. Incorporation of excess gadolinium into human bone from medical contrast agents. Metallomics. 2009;1(6):479-88.
109. White GW, Gibby WA, Tweedle MF. Comparison of Gd(DTPA-BMA) (Omniscan) versus Gd(HP-DO3A) (ProHance) relative to gadolinium retention in human bone tissue by inductively coupled plasma mass spectroscopy. Investigative radiology. 2006;41(3):272-8.
110. Roberts DR, Lindhorst SM, Welsh CT, Maravilla KR, Herring MN, Braun KA, Thiers BH, Davis WC. High Levels of Gadolinium Deposition in the Skin of a Patient With Normal Renal Function. Investigative radiology. 2016;51(5):280-9.
111. Sato T, Ito K, Tamada T, Kanki A, Watanabe S, Nishimura H, Tanimoto D, Higashi H, Yamamoto A. Tissue gadolinium deposition in renally impaired rats exposed to different gadolinium-based MRI contrast agents: evaluation with inductively coupled plasma mass spectrometry (ICP-MS). Magnetic resonance imaging. 2013;31(8):1412-7.
112. Koch J, Günther D. Review of the state-of-the-art of laser ablation inductively coupled plasma mass spectrometry. Appl Spectrosc. 2011;65(5):155-62.
113. Fingerhut S, Niehoff AC, Sperling M, Jeibmann A, Paulus W, Niederstadt T, Allkemper T, Heindel W, Holling M, Karst U. Spatially resolved quantification of gadolinium deposited in the brain of a patient treated with gadolinium-based contrast agents. J Trace Elem Med Biol. 2018;45:125-30.
114. El Hamrani D, Vives V, Buchholz R, Même W, Factor C, Fingerhut S, Sperling M, Karst U, Robert P, Même S. Effect of Long-Term Retention of Gadolinium on Metabolism of Deep Cerebellar Nuclei After Repeated Injections of Gadodiamide in Rats. Investigative radiology. 2020;55(2):120-8.
115. Barbosa LD, Sussulini A. Recent advances in LA-ICP-MS for biomedical applications. Biomedical Spectroscopy and Imaging. 2019;8:47-54.
116. Stärk HJ, Wennrich R. A new approach for calibration of laser ablation inductively coupled plasma mass spectrometry using thin layers of spiked agarose gels as references. Analytical and bioanalytical chemistry. 2011;399(6):2211-7.
117. Schneider CA, Rasband WS, Eliceiri KW. NIH Image to ImageJ: 25 years of image analysis. Nat Methods. 2012;9(7):671-5.
118. Pintaske J, Martirosian P, Graf H, Erb G, Lodemann KP, Claussen CD, Schick F. Relaxivity of Gadopentetate Dimeglumine (Magnevist), Gadobutrol (Gadovist), and Gadobenate Dimeglumine (MultiHance) in human blood plasma at 0.2, 1.5, 3 Tesla. Investigative radiology. 2006;41(3):213-21.
119. Taupitz M, Stolzenburg N, Ebert M, Schnorr J, Hauptmann R, Kratz H, Hamm B, Wagner S. Gadolinium-containing magnetic resonance contrast media: investigation on the possible transchelation of Gd^{3+} to the glycosaminoglycan heparin. Contrast Media Mol Imaging. 2013;8(2):108-16.
120. Humpel C. Organotypic Brain Slice Cultures. Curr Protoc Immunol. 2018;123(1):e59.
121. Gimsa U, Peter SV, Lehmann K, Bechmann I, Nitsch R. Axonal damage induced by invading T cells in organotypic central nervous system tissue in vitro: involvement of microglial cells. Brain pathology (Zurich, Switzerland). 2000;10(3):365-77.
122. Croft CL, Noble W. Preparation of organotypic brain slice cultures for the study of Alzheimer's disease. F1000Res. 2018;7:592.
123. Dionne KR, Tyler KL. Slice culture modeling of central nervous system (CNS) viral infection. Methods Mol Biol. 2013;1078:97-117.

124. Jang S, Kim H, Kim HJ, Lee SK, Kim EW, Namkoong K, Kim E. Long-Term Culture of Organotypic Hippocampal Slice from Old 3xTg-AD Mouse: An ex vivo Model of Alzheimer's Disease. Psychiatry Investig. 2018;15(2):205-13.
125. Opitz-Araya X, Barria A. Organotypic hippocampal slice cultures. J Vis Exp. 2011(48).
126. Wang Q, Andreasson K. The organotypic hippocampal slice culture model for examining neuronal injury. J Vis Exp. 2010(44).
127. Molz S, Tharine DC, Decker H, Tasca CI. GMP prevents excitotoxicity mediated by NMDA receptor activation but not by reversal activity of glutamate transporters in rat hippocampal slices. Brain Res. 2008;1231:113-20.
128. Zou JY, Crews FT. TNF alpha potentiates glutamate neurotoxicity by inhibiting glutamate uptake in organotypic brain slice cultures: neuroprotection by NF kappa B inhibition. Brain Res. 2005;1034(1-2):11-24.
129. Chang Q, Ornatsky OI, Siddiqui I, Loboda A, Baranov VI, Hedley DW. Imaging Mass Cytometry. Cytometry A. 2017;91(2):160-9.
130. Fluidigm. Imaging Mass Cytometry Staining Protocol for Frozen Tissue Sections.
131. Forslin Y, Martola J, Bergendal Å, Fredrikson S, Wiberg MK, Granberg T. Gadolinium Retention in the Brain: An MRI Relaxometry Study of Linear and Macrocyclic Gadolinium-Based Contrast Agents in Multiple Sclerosis. AJNR American journal of neuroradiology. 2019;40(8):1265-73.
132. Deike-Hofmann K, Reuter J, Haase R, Kuder T, Paech D, Bickelhaupt S, Forsting M, Schlemmer HP, Heußel CP, Radbruch A. No Changes in T1 Relaxometry After a Mean of 11 Administrations of Gadobutrol. Investigative radiology. 2020;55(6):381-6.
133. Müller A, Jurcoane A, Mädler B, Ditter P, Schild H, Hattingen E. Brain relaxometry after macrocyclic Gd-based contrast agent. Clinical neuroradiology. 2017;27(4):459-68.
134. Gianolio E, Bardini P, Arena F, Stefania R, Di Gregorio E, Iani R, Aime S. Gadolinium Retention in the Rat Brain: Assessment of the Amounts of Insoluble Gadolinium-containing Species and Intact Gadolinium Complexes after Repeated Administration of Gadolinium-based Contrast Agents. Radiology. 2017;285(3):839-49.
135. Jost G, Frenzel T, Lohrke J, Lenhard DC, Naganawa S, Pietsch H. Penetration and distribution of gadolinium-based contrast agents into the cerebrospinal fluid in healthy rats: a potential pathway of entry into the brain tissue. European radiology. 2017;27(7):2877-85.
136. Taoka T, Naganawa S. Gadolinium-based Contrast Media, Cerebrospinal Fluid and the Glymphatic System: Possible Mechanisms for the Deposition of Gadolinium in the Brain. Magnetic resonance in medical sciences : MRMS : an official journal of Japan Society of Magnetic Resonance in Medicine. 2018;17(2):111-9.
137. Nehra AK, McDonald RJ, Bluhm AM, Gunderson TM, Murray DL, Jannetto PJ, Kallmes DF, Eckel LJ, McDonald JS. Accumulation of Gadolinium in Human Cerebrospinal Fluid after Gadobutrol-enhanced MR Imaging: A Prospective Observational Cohort Study. Radiology. 2018;288(2):416-23.
138. Rasschaert M, Schroeder JA, Wu TD, Marco S, Emerit A, Siegmund H, Fischer C, Fretellier N, Idée JM, Corot C, Brochhausen C, Guerquin-Kern JL. Multimodal Imaging Study of Gadolinium Presence in Rat Cerebellum: Differences Between Gd Chelates, Presence in the Virchow-Robin Space, Association With Lipofuscin, and Hypotheses About Distribution Pathway. Investigative radiology. 2018;53(9):518-28.
139. Öner AY, Barutcu B, Aykol Ş, Tali ET. Intrathecal Contrast-Enhanced Magnetic Resonance Imaging-Related Brain Signal Changes: Residual Gadolinium Deposition? Investigative radiology. 2017;52(4):195-7.
140. Millward JM, Schnorr J, Taupitz M, Wagner S, Wuerfel JT, Infante-Duarte C. Iron oxide magnetic nanoparticles highlight early involvement of the choroid plexus in central nervous system inflammation. ASN neuro. 2013;5(1):e00110.
141. Solár P, Zamani A, Kubíčková L, Dubový P, Joukal M. Choroid plexus and the blood-cerebrospinal fluid barrier in disease. Fluids and barriers of the CNS. 2020;17(1):35.
142. Engelhardt B, Wolburg-Buchholz K, Wolburg H. Involvement of the choroid plexus in central nervous system inflammation. Microsc Res Tech. 2001;52(1):112-29.
143. Ramalho J, Semelka RC, Ramalho M, Nunes RH, AlObaidy M, Castillo M. Gadolinium-Based Contrast Agent Accumulation and Toxicity: An Update. AJNR American journal of neuroradiology. 2016;37(7):1192-8.
144. Berndt D, Millward JM, Schnorr J, Taupitz M, Stangl V, Paul F, Wagner S, Wuerfel JT, Sack I, Ludwig A, Infante-Duarte C. Inflammation-induced brain endothelial activation leads to uptake of electrostatically stabilized iron oxide nanoparticles via sulfated glycosaminoglycans. Nanomedicine : nanotechnology, biology, and medicine. 2017;13(4):1411-21.

145. Millward JM, Ariza de Schellenberger A, Berndt D, Hanke-Vela L, Schellenberger E, Waiczies S, Taupitz M, Kobayashi Y, Wagner S, Infante-Duarte C. Application of Europium-Doped Very Small Iron Oxide Nanoparticles to Visualize Neuroinflammation with MRI and Fluorescence Microscopy. Neuroscience. 2017.
146. Wang S, Millward JM, Hanke-Vela L, Malla B, Pilch K, Gil-Infante A, Waiczies S, Mueller S, Boehm-Sturm P, Guo J, Sack I, Infante-Duarte C. MR Elastography-Based Assessment of Matrix Remodeling at Lesion Sites Associated With Clinical Severity in a Model of Multiple Sclerosis. Frontiers in neurology. 2019;10:1382.
147. Silva RV, Morr AS, Mueller S, Koch SP, Boehm-Sturm P, Rodriguez-Sillke Y, Kunkel D, Tzschätzsch H, Kühl AA, Schnorr J, Taupitz M, Sack I, Infante-Duarte C. Contribution of Tissue Inflammation and Blood-Brain Barrier Disruption to Brain Softening in a Mouse Model of Multiple Sclerosis. Front Neurosci. 2021;15:701308.
148. Silva RV, Biskup K, Zabala-Jouvin JK, Batzdorf CS, Stellmach C, Morr AS, Sack I, Ludwig A, Blanchard V, Infante-Duarte C. Brain inflammation induces alterations in glycosaminoglycan metabolism and subsequent changes in CS-4S and hyaluronic acid. Int J Biol Macromol. 2023;230:123214.
149. Werner P, Schuenke P, Krylova O, Nikolenko H, Taupitz M, Schröder L. Investigating the Role of Sulfate Groups for the Binding of Gd(3+) Ions to Glycosaminoglycans with NMR Relaxometry. ChemMedChem. 2022;17(13):e202100764.
150. Habermeyer J, Boyken J, Harrer J, Canneva F, Ratz V, Moceri S, Admard J, Casadei N, Jost G, Bäuerle T, Frenzel T, Schmitz C, Schütz G, Pietsch H, von Hörsten S. Comprehensive phenotyping revealed transient startle response reduction and histopathological gadolinium localization to perineuronal nets after gadodiamide administration in rats. Scientific reports. 2020;10(1):22385.
151. Song Y, Zhang F, Linhardt RJ. Glycosaminoglycans. Adv Exp Med Biol. 2021;1325:103-16.
152. Sobel RA, Ahmed AS. White matter extracellular matrix chondroitin sulfate/dermatan sulfate proteoglycans in multiple sclerosis. J Neuropathol Exp Neurol. 2001;60(12):1198-207.
153. Smith PD, Coulson-Thomas VJ, Foscarin S, Kwok JC, Fawcett JW. "GAG-ing with the neuron": The role of glycosaminoglycan patterning in the central nervous system. Exp Neurol. 2015;274(Pt B):100-14.
154. Winkler CW, Foster SC, Matsumoto SG, Preston MA, Xing R, Bebo BF, Banine F, Berny-Lang MA, Itakura A, McCarty OJ, Sherman LS. Hyaluronan anchored to activated CD44 on central nervous system vascular endothelial cells promotes lymphocyte extravasation in experimental autoimmune encephalomyelitis. J Biol Chem. 2012;287(40):33237-51.
155. Bredholt M, Frederiksen JL. Zinc in Multiple Sclerosis: A Systematic Review and Meta-Analysis. ASN neuro. 2016;8(3).
156. Choi BY, Jung JW, Suh SW. The Emerging Role of Zinc in the Pathogenesis of Multiple Sclerosis. Int J Mol Sci. 2017;18(10).
157. Puttagunta NR, Gibby WA, Smith GT. Human in vivo comparative study of zinc and copper transmetallation after administration of magnetic resonance imaging contrast agents. Investigative radiology. 1996;31(12):739-42.
158. Rohrer M, Bauer H, Mintorovitch J, Requardt M, Weinmann HJ. Comparison of magnetic properties of MRI contrast media solutions at different magnetic field strengths. Investigative radiology. 2005;40(11):715-24.
159. McDonald RJ, McDonald JS, Dai D, Schroeder D, Jentoft ME, Murray DL, Kadirvel R, Eckel LJ, Kallmes DF. Comparison of Gadolinium Concentrations within Multiple Rat Organs after Intravenous Administration of Linear versus Macrocyclic Gadolinium Chelates. Radiology. 2017;285(2):536-45.
160. Bower DV, Richter JK, von Tengg-Kobligk H, Heverhagen JT, Runge VM. Gadolinium-Based MRI Contrast Agents Induce Mitochondrial Toxicity and Cell Death in Human Neurons, and Toxicity Increases With Reduced Kinetic Stability of the Agent. Investigative radiology. 2019;54(8):453-63.
161. Erdoğan MA, Apaydin M, Armagan G, Taskiran D. Evaluation of toxicity of gadolinium-based contrast agents on neuronal cells. Acta radiologica (Stockholm, Sweden : 1987). 2021;62(2):206-14.
162. Mallio CA, Rovira À, Parizel PM, Quattrocchi CC. Exposure to gadolinium and neurotoxicity: current status of preclinical and clinical studies. Neuroradiology. 2020;62(8):925-34.
163. Xia Q, Feng X, Huang H, Du L, Yang X, Wang K. Gadolinium-induced oxidative stress triggers endoplasmic reticulum stress in rat cortical neurons. J Neurochem. 2011;117(1):38-47.
164. Feng X, Xia Q, Yuan L, Yang X, Wang K. Impaired mitochondrial function and oxidative stress in rat cortical neurons: implications for gadolinium-induced neurotoxicity. Neurotoxicol. 2010;31(4):391-8.
165. Turrens JF. Mitochondrial formation of reactive oxygen species. J Physiol. 2003;552(Pt 2):335-44.
166. Milatovic D, Zaja-Milatovic S, Gupta RC, Yu Y, Aschner M. Oxidative damage and neurodegeneration in manganese-induced neurotoxicity. Toxicol Appl Pharmacol. 2009;240(2):219-25.

167. Fresegna D, Bullitta S, Musella A, Rizzo FR, De Vito F, Guadalupi L, Caioli S, Balletta S, Sanna K, Dolcetti E, Vanni V, Bruno A, Buttari F, Stampanoni Bassi M, Mandolesi G, Centonze D, Gentile A. Re-Examining the Role of TNF in MS Pathogenesis and Therapy. Cells. 2020;9(10).
168. Aktas O, Smorodchenko A, Brocke S, Infante-Duarte C, Schulze Topphoff U, Vogt J, Prozorovski T, Meier S, Osmanova V, Pohl E, Bechmann I, Nitsch R, Zipp F. Neuronal damage in autoimmune neuroinflammation mediated by the death ligand TRAIL. Neuron. 2005;46(3):421-32.
169. Tweedle MF, Wedeking P, Kumar K. Biodistribution of radiolabeled, formulated gadopentetate, gadoteridol, gadoterate, and gadodiamide in mice and rats. Invest radiol. 1995;30(6):372-80.
170. Smith AP, Marino M, Roberts J, Crowder JM, Castle J, Lowery L, Morton C, Hibberd MG, Evans PM. Clearance of Gadolinium from the Brain with No Pathologic Effect after Repeated Administration of Gadodiamide in Healthy Rats: An Analytical and Histologic Study. Radiology. 2017;282(3):743-51.
171. Cocozza S, Pontillo G, Lanzillo R, Russo C, Petracca M, Di Stasi M, Paolella C, Vola EA, Criscuolo C, Moccia M, Lamberti A, Monti S, Brescia Morra V, Elefante A, Palma G, Tedeschi E, Brunetti A. MRI features suggestive of gadolinium retention do not correlate with Expanded Disability Status Scale worsening in Multiple Sclerosis. Neuroradiology. 2019;61(2):155-62.
172. Forslin Y, Shams S, Hashim F, Aspelin P, Bergendal G, Martola J, Fredrikson S, Kristoffersen-Wiberg M, Granberg T. Retention of Gadolinium-Based Contrast Agents in Multiple Sclerosis: Retrospective Analysis of an 18-Year Longitudinal Study. American journal of neuroradiology. 2017;38(7):1311-6.
173. Ackermans N, Taylor C, Tam R, Carruthers R, Kolind S, Kang H, Freedman MS, Li DK, Traboulsee AL. Effect of different doses of gadolinium contrast agent on clinical outcomes in MS. Mult Scler J Exp Transl Clin. 2019;5(1):2055217318823796.
174. Zivadinov R, Bergsland N, Hagemeier J, Ramasamy DP, Dwyer MG, Schweser F, Kolb C, Weinstock-Guttman B, Hojnacki D. Cumulative gadodiamide administration leads to brain gadolinium deposition in early MS. Neurology. 2019;93(6):e611-e23.
175. Barkhof F. The clinico-radiological paradox in multiple sclerosis revisited. 2002;15(3):239-45.
176. Jost G, Lenhard DC, Sieber MA, Lohrke J, Frenzel T, Pietsch H. Signal Increase on Unenhanced T1-Weighted Images in the Rat Brain After Repeated, Extended Doses of Gadolinium-Based Contrast Agents: Comparison of Linear and Macrocyclic Agents. Investigative radiology. 2016;51(2):83-9.
177. Bonnier G, Roche A, Romascano D, Simioni S, Meskaldji D, Rotzinger D, Lin YC, Menegaz G, Schluep M, Du Pasquier R, Sumpf TJ, Frahm J, Thiran JP, Krueger G, Granziera C. Advanced MRI unravels the nature of tissue alterations in early multiple sclerosis. Ann Clin Transl Neurol. 2014;1(6):423-32.
178. Deoni SC. Quantitative relaxometry of the brain. Top Magn Reson Imaging. 2010;21(2):101-13.
179. Does MD. Inferring brain tissue composition and microstructure via MR relaxometry. NeuroImage. 2018;182:136-48.
180. Granziera C, Wuerfel J, Barkhof F, Calabrese M, De Stefano N, Enzinger C, Evangelou N, Filippi M, Geurts JJG, Reich DS, Rocca MA, Ropele S, Rovira À, Sati P, Toosy AT, Vrenken H, Gandini Wheeler-Kingshott CAM, Kappos L. Quantitative magnetic resonance imaging towards clinical application in multiple sclerosis. Brain. 2021;144(5):1296-311.
181. Du S, Sah SK, Zeng C, Wang J, Liu Y, Xiong H, Li Y. Iron deposition in the gray matter in patients with relapse-remitting multiple sclerosis: A longitudinal study using three-dimensional (3D)-enhanced T2*-weighted angiography (ESWAN). European journal of radiology. 2015;84(7):1325-32.
182. Kolb H, Absinta M, Beck ES, Ha SK, Song Y, Norato G, Cortese I, Sati P, Nair G, Reich DS. 7T MRI Differentiates Remyelinated from Demyelinated Multiple Sclerosis Lesions. Annals of neurology. 2021;90(4):612-26.
183. Vrenken H, Geurts JJ, Knol DL, van Dijk LN, Dattola V, Jasperse B, van Schijndel RA, Polman CH, Castelijns JA, Barkhof F, Pouwels PJ. Whole-brain T1 mapping in multiple sclerosis: global changes of normal-appearing gray and white matter. Radiology. 2006;240(3):811-20.
184. Leung AH, Jin J, Wang S, Lei H, Wong WT. Inflammation targeted Gd(3+)-based MRI contrast agents imaging tumor and rheumatoid arthritis models. Bioconjug Chem. 2014;25(6):1112-23.
185. Lohmeier J, Silva RV, Tietze A, Taupitz M, Kaneko T, Prüss H, Paul F, Infante-Duarte C, Hamm B, Caravan P, Makowski MR. Fibrin-targeting molecular MRI in inflammatory CNS disorders. Eur J Nucl Med Mol Imaging. 2022;49(11):3692-704.
186. Huuskonen J, Suuronen T, Miettinen R, van Groen T, Salminen A. A refined in vitro model to study inflammatory responses in organotypic membrane culture of postnatal rat hippocampal slices. Journal of neuroinflammation. 2005;2:25.
187. Misgeld T, Kerschensteiner M, Bareyre FM, Burgess RW, Lichtman JW. Imaging axonal transport of mitochondria in vivo. Nat Methods. 2007;4(7):559-61.
188. Malla B, Liotta A, Bros H, Ulshöfer R, Paul F, Hauser AE, Niesner R, Infante-Duarte C. Teriflunomide Preserves Neuronal Activity and Protects Mitochondria in Brain Slices Exposed to Oxidative Stress. Int J Mol Sci. 2022;23(3).

Statutory Declaration

"I, Lina C. Anderhalten, by personally signing this document in lieu of an oath, hereby affirm that I prepared the submitted dissertation on the topic '*Investigation of inflammation-promoted gadolinium retention within the central nervous system in the EAE mouse model and ex vivo - Untersuchung der durch Entzündung vermittelten Gadolinium-Retention im zentralen Nervensystem am EAE-Mausmodell und ex vivo'*, independently and without the support of third parties, and that I used no other sources and aids than those stated.

All parts which are based on the publications or presentations of other authors, either in letter or in spirit, are specified as such in accordance with the citing guidelines. The sections on methodology (in particular regarding practical work, laboratory regulations, statistical processing) and results (in particular regarding figures, charts, and tables) are exclusively my responsibility.

Furthermore, I declare that I have correctly marked all of the data, the analyses, and the conclusions generated from data obtained in collaboration with other persons and that I have correctly marked my own contribution and the contributions of other persons (cf. declaration of contribution). I have correctly marked all texts or parts of texts that were generated in collaboration with other persons.

My contributions to any publications to this dissertation correspond to those stated in the below joint declaration made together with the supervisor. All publications created within the scope of the dissertation comply with the guidelines of the ICMJE (International Committee of Medical Journal Editors; http://www.icmje.org) on authorship. In addition, I declare that I shall comply with the regulations of Charité – Universitätsmedizin Berlin on ensuring good scientific practice.

I declare that I have not yet submitted this dissertation in identical or similar form to another Faculty.

The significance of this statutory declaration and the consequences of a false statutory declaration under criminal law (Sections 156, 161 of the German Criminal Code) are known to me."

Date	Lina C. Anderhalten

Declaration of your own contribution to the publications

Lina C. Anderhalten contributed the following to the below-listed publication:

Anderhalten L, Silva RV, Morr A, Wang S, Smorodchenko A, Saatz J, Traub H, Mueller S, Boehm-Sturm P, Rodriguez-Sillke Y, Kunkel D, Hahndorf J, Paul F, Taupitz M, Sack I, Infante-Duarte C. **Different Impact of Gadopentetate and Gadobutrol on Inflammation-Promoted Retention and Toxicity of Gadolinium Within the Mouse Brain.** Investigative radiology. 2022;57(10):677-88.

Together with A. Morr, I prepared the animal experiment application that underlies this publication. I conceptualized the study design together with C. Infante-Duarte and S. Wang. For the *in vivo* part of the study, R. V. Silva and I performed the induction of active EAE in mice. Thereafter, I personally carried out all steps of mouse handling, including weighting, scoring, i.p. injections of glucose, and i.v. injections of GBCAs via the mouse tail vein. I independently acquired all *in vivo* MRI scans for this study, while the MRI data analysis involving ABA registration and ventricle mask subtraction was performed by S. Mueller. I was responsible for sacrificing the mice, isolating tissues, preparing brain sections, collecting blood samples, conducting histological stainings, and performing bright-field microscopy. Regarding the *ex vivo* part of the study, I designed the experimental setup with the assistance of A. Smorodchenko. I then carried out all subsequent establishment steps, which were the basis for the *ex vivo* data shown in this original publication *(Figure 2 and 6*). I independently conducted the *ex vivo* experiments, including fluorescence microscopy, presented in this study.

The execution of LA-ICP-MS, ICP-MS, and IMC measurements presented in this study was done through a collaborative effort with our partners H. Traub and J. Saatz (LA-ICP-MS/ICP-MS), as well as D. Kunkel and Y. Rodriguez-Sillke (IMC). The subsequent analysis of LA-ICP-MS, IMC, and microscopy image files was carried out by me. I also performed the statistical analysis of all data underlying this study, which was additionally validated by the Institute of Biometry and Clinical Epidemiology at Charité. I am further personally responsible for visualizing all data from the original publication in graphs and figures (*Figures 1-6, supplemental digital content Figures 1-3).*

I wrote the initial version of the manuscript, which was further enhanced by C. Infante-Duarte before the other co-authors contributed additional corrections or modifications. During the revision process, I addressed the peer-reviewer’s questions and, together with the other co-authors, improved the manuscript based on their comments.

Overall, I contributed to the conceptualization of the study, planning, and execution of experiments, analysis of data, the composition of all figures presented in the original publication, and preparation as well as revision of the manuscript.

Signature, date, and stamp of first supervising university professor / lecturer

Signature of doctoral candidate

Printing copy of the publication

SPECIAL ISSUE 2022-CONTRAST MEDIA

OPEN

Different Impact of Gadopentetate and Gadobutrol on Inflammation-Promoted Retention and Toxicity of Gadolinium Within the Mouse Brain

Lina Anderhalten, MD,[*] Rafaela V. Silva, MSc,[†] Anna Morr, MSc,[‡] Shuangqing Wang, MD,[*]*
*Alina Smorodchenko, MD,[§] Jessica Saatz, PhD,[||] Heike Traub, PhD,[||] Susanne Mueller, MSc,[¶**]*
*Philipp Boehm-Sturm, PhD,[¶**] Yasmina Rodriguez-Sillke, PhD,[††] Désirée Kunkel, PhD,[††]*
Julia Hahndorf, MSc,[‡] Friedemann Paul, MD,[*] Matthias Taupitz, MD,[‡]
Ingolf Sack, PhD,[‡] and Carmen Infante-Duarte, PhD[*]

Objectives: Using a murine model of multiple sclerosis, we previously showed that repeated administration of gadopentetate dimeglumine led to retention of gadolinium (Gd) within cerebellar structures and that this process was enhanced with inflammation. This study aimed to compare the kinetics and retention profiles of Gd in inflamed and healthy brains after application of the macrocyclic Gd-based contrast agent (GBCA) gadobutrol or the linear GBCA gadopentetate. Moreover, potential Gd-induced neurotoxicity was investigated in living hippocampal slices ex vivo.

Materials and Methods: Mice at peak of experimental autoimmune encephalomyelitis (EAE; n = 29) and healthy control mice (HC; n = 24) were exposed to a cumulative dose of 20 mmol/kg bodyweight of either gadopentetate dimeglumine or gadobutrol (8 injections of 2.5 mmol/kg over 10 days). Magnetic resonance imaging (7 T) was performed at baseline as well as at day 1, 10, and 40 post final injection (pfi) of GBCAs. Mice were sacrificed after magnetic resonance imaging and brain and blood Gd content was assessed by laser ablation-inductively coupled plasma (ICP)-mass spectrometry (MS) and ICP-MS, respectively. In addition, using chronic organotypic hippocampal slice cultures, Gd-induced neurotoxicity was addressed in living brain tissue ex vivo, both under control or inflammatory (tumor necrosis factor α [TNF-α] at 50 ng/μL) conditions.

Results: Neuroinflammation promoted a significant decrease in T1 relaxation times after multiple injections of both GBCAs as shown by quantitative T1 mapping of EAE brains compared with HC. This corresponded to higher Gd retention within the EAE brains at 1, 10, and 40 days pfi as determined by laser ablation-ICP-MS. In inflamed cerebellum, in particular in the deep cerebellar nuclei (CN), elevated Gd retention was observed until day 40 after last gadopentetate application (CN: EAE vs HC, 55.06 ± 0.16 μM vs 30.44 ± 4.43 μM). In contrast, gadobutrol application led to a rather diffuse Gd content in the inflamed brains, which strongly diminished until day 40 (CN: EAE vs HC, 0.38 ± 0.08 μM vs 0.17 ± 0.03 μM). The analysis of cytotoxic effects of both GBCAs using living brain tissue revealed an elevated cell death rate after incubation with gadopentetate but not gadobutrol at 50 mM. The cytotoxic effect due to gadopentetate increased in the presence of the inflammatory mediator TNF-α (with vs without TNF-α, 3.15% ± 1.18% vs 2.17% ± 1.14%; $P = 0.0345$).

Conclusions: In the EAE model, neuroinflammation promoted increased Gd retention in the brain for both GBCAs. Whereas in the inflamed brains, efficient clearance of macrocyclic gadobutrol during the investigated time period was observed, the Gd retention after application of linear gadopentetate persisted over the entire observational period. Gadopentetate but not gadubutrol appeared to be neurotoxic in an ex vivo paradigm of neuronal inflammation.

Key Words: cerebellar nuclei, experimental autoimmune encephalomyelitis, gadolinium-based contrast agents, gadolinium retention, gadolinium-induced toxicity, imaging mass cytometry, laser ablation inductively coupled plasma mass spectrometry, magnetic resonance imaging, multiple sclerosis, neuroinflammation

(*Invest Radiol* 2022;57: 677–688)

Gadolinium-based contrast agents (GBCAs) are commonly used in contrast-enhanced magnetic resonance imaging (MRI) because of their ability to improve the visibility of internal body structures by increasing the relaxation rate of nearby water protons in vivo.[1] The diagnostic application of GBCAs is currently considered largely safe in patients with normal renal function. However, after repeated administration of mainly linear GBCAs, retention of gadolinium (Gd) within different organs was reported to occur in patients without renal impairment.[2,3] This resulted in restrictions on the use of linear GBCAs by the European Medicines Agency (EMA/625317/2017)[4] and class warnings by the US Food and Drug Administration.[5]

Within central nervous system (CNS) structures, Kanda et al[6] revealed for the first time a positive correlation between previous administrations of linear GBCAs and T1 hyperintensities in unenhanced brain MRI scans, in particular in the dentate nucleus (DN). These observations were confirmed by several other authors in humans[7–12] and rodent models,[13–19] principally after repeated application of linear GBCAs. Moreover, Gd retention in neuronal parenchyma, especially inside the DN, was quantitatively assessed by inductively coupled plasma mass spectrometry (ICP-MS) or laser ablation ICP-MS (LA-ICP-MS)[17,20–26] after in vivo GBCA administration.

Received for publication February 7, 2022; and accepted for publication, after revision, March 16, 2022.

From the [*]Experimental and Clinical Research Center (ECRC), A Cooperation Between the Charité–Universitätsmedizin Berlin, Corporate Member of Freie Universität Berlin and Humboldt-Universität zu Berlin, and Max-Delbrück-Center for Molecular Medicine (MDC) in the Helmholtz Association, Berlin; [†]Einstein Center for Neurosciences and [‡]Department of Radiology, Charité–Universitätsmedizin Berlin, Corporate Member of Freie Universität Berlin and Humboldt–Universität zu Berlin, Berlin; [§]Institute for Translational Medicine and Faculty of Human Medicine, MSH Medical School Hamburg, Hamburg; [||]Bundesanstalt für Materialforschung und -prüfung, Berlin; [¶]Department of Experimental Neurology and Center for Stroke Research and [**]NeuroCure Cluster of Excellence and Charité Core Facility 7T Experimental MRIs, Charité–Universitätsmedizin Berlin, Berlin; and [††]Berlin Institute of Health at Charité–Universitätsmedizin Berlin, Flow & Mass Cytometry Core Facility, Berlin, Germany.

Conflicts of interest and sources of funding: This work was supported by the German Research Foundation (Deutsche Forschungsgemeinschaft, DFG), SFB1340-1 (B05 and C02), the Einstein Center for Neurosciences Berlin (ECN), and by the Hertie Foundation (medMS scholarship: P1180047).

Correspondence to: Carmen Infante-Duarte, PhD, Experimental and Clinical Research Center (ECRC), Charité–Universitätsmedizin Berlin, Campus Buch, Lindenberger Weg 80, 13125 Berlin, Germany. E-mail: carmen.infante@charite.de.

Supplemental digital contents are available for this article. Direct URL citations appear in the printed text and are provided in the HTML and PDF versions of this article on the journal's Web site (www.investigativeradiology.com).

ISSN: 0020-9996/22/5710–0677
DOI: 10.1097/RLI.0000000000000884

The risk of interstitial retention is especially high for the kinetically less stable linear GBCAs compared with macrocyclic agents.[27,28] It is suggested that linear GBCAs partially dechelate in vivo, leading to transmetallation with endogenous cations such as calcium,[29] iron,[30] or zinc,[31] resulting in long-term retention inside the brain. Contrary to that, macrocyclic GBCAs are expected to be washed out continuously in the form of the intact chelate,[17,32] following specific clearance kinetics for the different macrocyclic compounds.[33,34]

In the context of chronic inflammation of the CNS such as in multiple sclerosis, GBCAs are primarily applied to determine the magnitude of blood-brain barrier (BBB) disruption and to estimate the number of active inflammatory lesions within the CNS.[35] Hence, the concern for Gd retention is particularly relevant for patients with multiple sclerosis because GBCA-MRI is commonly used for initial diagnosis as well as for monitoring both clinical course and treatment response.[36] Moreover, we previously reported using the experimental autoimmune encephalomyelitis (EAE) model that neuroinflammation may facilitate the retention of Gd in the mouse brains. We showed that 10 days after repeated gadopentetate injections, Gd levels were higher within inflamed brains compared with healthy controls (HCs) and demonstrated the formation of an elevated number of submicrometric Gd hotspots in the deep cerebellar nuclei (CN) of EAE mice.[37]

However, it has not yet been clarified for how long Gd may be retained in the inflamed CNS compared with healthy CNS, what factors may contribute to brain retention, how linear and macrocyclic GBCAs differ in terms of magnitude and kinetics of retention, and how Gd may affect neuronal tissue under inflammatory conditions. Therefore, we aimed to monitor and quantify Gd retention in brain tissue by MRI and LA-ICP-MS after repeated administration of either the linear gadopentetate or the macrocyclic gadobutrol in both healthy and EAE mice in vivo. Furthermore, using the well-established ex vivo model of organotypic hippocampal slice culture, we assessed Gd toxicity and how an inflammatory milieu may affect its toxic potential.

MATERIALS AND METHODS

Mouse Model of EAE and Study Design

Animal experiments were conducted in accordance with national and institutional guidelines for the care and use of laboratory animals and with directive 2010/63/EU of the European Parliament and of the Council of 22 September 2010 and were approved by the Berlin State Office for Health and Social Affairs (LAGeSo, registration number G106/19). Experimental autoimmune encephalomyelitis was actively induced in 9- to 12-week-old SJL/J female mice (Janvier Labs, France; n = 29) by subcutaneous immunization with 250 μg proteolipid protein peptide (PLP$_{139–151}$; purity 95%; Pepceuticals, Leicester, United Kingdom) and 800 μg *Mycobacterium tuberculosis* H37Ra (Difco, Franklin Lakes, NJ) diluted in 100 μL complete Freund's adjuvant. In addition, 250 ng pertussis toxin (List, Biological Laboratories, Campbell, CA) were injected intraperitoneally on day 0 (day of immunization) and day 2 of the study. The EAE mice were monitored daily for clinical deficiency as follows: 0 = no disease; 1 = complete tail paralysis; 2 = hindlimb paresis; 3 = hindlimb plegia; 4 = paraplegia and forelimb weakness; and 5 = moribund or death. Experimental autoimmune encephalomyelitis (n = 29) and HC (n = 24) mice were exposed to 8 intravenous injections via the tail vein of either a linear GBCA (gadopentetate dimeglumine; Magnevist, Bayer, Germany, n = 27) or a macrocyclic GBCA (gadobutrol; Gadovist, Bayer, n = 26) at 2.5 mmol/kg body weight (BW), which corresponds to a cumulative dose of 20 mmol/kg BW. As displayed in Figure 1A, 4 consecutive daily injections of either gadopentetate or gadobutrol were followed by a 2-day break to reduce stress for the animals and 4 additional injection days as described previously.[37] The GBCA applications started on day 12 to 13 postimmunization when EAE mice showed a peak of disability. The EAE mice presented first clinical signs on days 8 to 10, reached maximal clinical disability on day 12 to 13, and further showed a relapsing-remitting course until day 64 (Fig. 1B). No significant differences in EAE score between the time points of LA-ICP-MS, comparing the gadopentetate and gadobutrol groups, were detected (Kruskal-Wallis test; all EAE animals killed at respective time points [n = 4–5], $P = 0.7509$; EAE animals examined using LA-ICP-MS [n = 2], $P = 0.3824$).

MRI and Image Data Analysis

Whole-brain coronal MRI scans were performed in vivo in EAE and HC mice on a 7 T small-animal scanner (Bruker PharmaScan, Ettlingen, Germany), running ParaVision 6.1 software at baseline (immediately before the first GBCA injection) and 1, 10, and 40 days post final injection (pfi) of either a linear or a macrocyclic GBCA. Measurements were conducted using a 72-mm linear volume coil for excitation (RAPID Biomedical GmbH, Rimpar, Germany) and a mouse head surface coil (Bruker, Ettlingen, Germany). T1 map image acquisition was conducted using an axial 2-dimensional rapid acquisition with relaxation enhancement at variable repetition times (RARE-VTR) sequence (echo time, 9.83 milliseconds; 8 repetition times from 255 to 7000 milliseconds; rare factor = 2; field of view, 19.2 mm^2; matrix, 128 × 128; number of slices = 10; slice thickness, 1 mm; scan time, 17 minutes 13 seconds). During imaging, mice were anesthetized with 1.0% to 1.5% isoflurane in 30% O_2 and 70% N_2O administered via face mask, and gently fixed to the head coil to reduce motion and breathing artifacts. To maintain body temperature constant, animals were placed on a bed with circulating heated water. Respiration was monitored using a pressure-sensitive pad placed on the thorax (Small Animal Instruments Inc, Stony Brook, NY).

Magnetic resonance imaging data were registered to the Allen mouse brain atlas (ABA), as described elsewhere,[38] in a blinded manner using an in-house developed MATLAB toolbox ANTx (available under https://github.com/ChariteExpMri/antx2). The T1 relaxation times of each single ABA brain structure were calculated using the back-transformed atlas, which matched the individual magnetic resonance images. The quantitative relaxometry assessment of Gd retention does not require any reference region. Differences in T1 relaxation time between baseline MRI and MRI at the different time points pfi of GBCAs were quantified as T1 relaxation time change (T1 change (%) = $(T1_{\text{pfi of GBCA}} - T1_{\text{baseline}})/T1_{\text{baseline}} * 100$). In animals with enlarged ventricles due to neuroinflammation, atlas transformation was corrected by subtracting the individual ventricle masks segmented on T2-weighted images using Analyze 10.0 (AnalyzeDirect, Inc).

Tissue Processing and Histology

Mice were sacrificed with an overdose of ketamine/xylazine either 1, 10, or 40 days pfi of GBCAs (n = 4–5 mice/time point). Blood was collected and animals were immediately transcardially perfused with 0.1 M PBS at a continuous perfusion speed of 40 rpm (U/min; Ismatec ISM444B-115 V Analog Peristaltic Pump). Brains were extracted, fixed in 4% paraformaldehyde (PFA) and 30% sucrose, embedded and frozen (−80°C) for subsequent histological examinations. For histology, brains were cut coronally separating the forebrain, midbrain, and cerebellum. Frozen brain sections were cut in the coronal plane into 10-μm-thick cryosections and stored at −80°C. Consecutive frozen sections of those chosen for LA-ICP-MS were stained with hematoxylin and eosin (H&E) according to the standard protocol to assess inflammation. Hematoxylin and eosin images were acquired at ×2 and ×10 magnifications with a Keyence Fluorescence Microscope (BZ-X800, Germany) using the bright field mode.

LA-ICP-MS of Cerebellar Slices

The LA-ICP-MS analysis of 10-μm-thick cerebellar cryosections was performed on a commercial LA system (NWR-213; ESI, Bozeman, MT) equipped with a 2-volume sample chamber coupled to a sector field ICP-MS (Element XR; Thermo Fisher Scientific, Bremen, Germany). A Y-piece was used to add argon to the helium carrier gas before entering the plasma. The ICP-MS was tuned daily for maximum ion intensity, signal stability (relative standard deviation <5%), and oxide ratio (ThO/Th <1%) during continuous ablation on a microscopic glass slide.

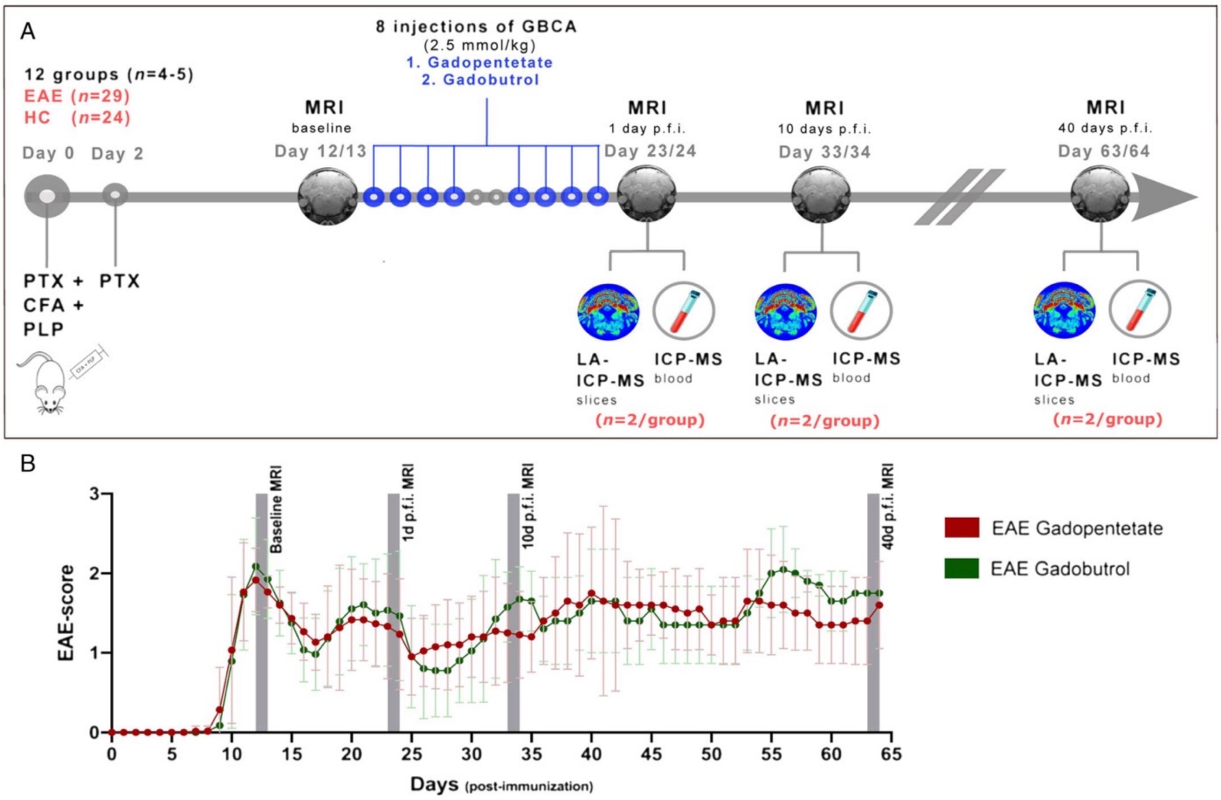

FIGURE 1. Animal study design. A, Schematic illustration of the in vivo setup. A total of 24 HC and 29 EAE mice received 8 intravenous injections of either gadopentetate or gadobutrol at 2.5 mmol/kg BW (cumulative dose: 20 mmol/kg BW, 2-day pause after 4 consecutive applications). Mice underwent a baseline MRI before the first injection and further scans at day 1, 10, and 40 pfi of GBCAs. In EAE mice, baseline MRI started on day 12 to 13 postimmunization (peak of disease). After the MRI scans, 4 to 5 animals per group were sacrificed; brains were processed for LA-ICP-MS, and blood was collected for ICP-MS (n = 2/group). B, Clinical course of EAE animals based on the EAE score (mean ± SD). Red: gadopentetate-treated animals (n = 15), green: gadobutrol-treated animals (n = 14).

Instrumental parameters of the ICP-MS system include radio frequency (RF) power: 1350 W; plasma gas flow (Ar): 16 L min^{-1}; sample gas flow (Ar): 0.660 L min^{-1}; auxiliary gas flow (Ar); 1.05 L min^{-1}; mass resolution: 300 m/Δm; scanning mode: line by line; detected isotopes: ^{31}P, ^{34}S, ^{44}Ca, ^{55}Mn, ^{57}Fe, ^{65}Cu, ^{66}Zn, ^{153}Eu, ^{158}Gd, and ^{160}Gd. Parameters of the LA system include wavelength: 213 nm; helium gas flow: 1 L min^{-1}; laser fluence: 1.9 J cm^{-2}; spot size: 100 μm; scan speed: 100 μm s^{-1}; repetition rate: 20 Hz; and line overlap: 20 μm. Data visualization was done in Origin 2018 (OriginLab Corporation, Northampton, MA). Calibration for ^{65}Cu, ^{66}Zn, and ^{158}Gd (translation of count per spot of ablation [CPS] into fg/pixel) and drift correction was carried out by measuring matrix-matched standards cast on glass slides using analyte spiked agarose gels (analyte contents 0–310 fg/pixel).[39] For further analysis of Gd retention in the whole cerebellar slice (mean), DN, and CN, manual regions of interest (ROIs) were applied to the calibrated LA-ICP-MS images of ^{158}Gd. The analysis of each region was conducted 3 times in an independent randomized manner using ImageJ software[40] for better reliability, and obtained Gd concentrations were averaged. Calibrated concentrations of ^{66}Zn and ^{158}Gd (fg/pixel) were translated into molar values (μM) where 1 pixel corresponded to 80 μm × 22 μm × 10 μm (1.76 × 10^{-11} L) of brain volume.

Analysis of Blood Samples by ICP-MS

Blood samples were thawed and digested by a high-pressure asher (HPA-S, Anton Paar GmbH, Graz, Austria). In brief, 0.5 mL subboiled nitric acid (HNO_3, 65%) was added to 100 mg of each blood sample and incubated overnight. Thereafter, samples were incinerated for 3 hours at 300°C. After cooling, the digested samples were diluted to a volume of 5 mL with MilliQ water. Samples were measured with an Element 2 ICP sector field mass spectrometer (Thermo Fisher Scientific) in combination with the autosampler 4DXF-73A (ESI Elemental Service & Instruments GmbH, Mainz, Germany). Calibration was carried out by standard addition of diluted multielement ICP standards. Blood control samples were obtained from an unmanipulated age- and sex-matched mouse. Instrumental parameters of the ICP-MS system for blood analysis include RF power: 1250 W; plasma gas flow (Ar): 16 L min^{-1}; sample gas flow (Ar): 1.215 L min^{-1}; auxiliary gas flow (Ar); 1.05 L min^{-1}; mass resolution: 4000 m/Δm; detected isotopes: ^{55}Mn, ^{115}In, ^{155}Gd, ^{156}Gd, ^{157}Gd, ^{158}Gd, and ^{160}Gd.

Generation of Chronic Organotypic Hippocampal Slices and Applied Culture Conditions

SJL/J pups (7–10 days) were decapitated, brains removed, and hippocampi extracted and sectioned coronally into 350-μm-thick slices using a McIlwain Tissue Chopper (Mickle Laboratory Engineering Co Ltd, UK). Six single slices from different mice were placed on 1 membrane of a cell culture insert (Millicell inserts, Merck, Germany) in a 6-well plate with 2 mL prewarmed (37°C) and oxygenized modified Opitz-Araya slice culture medium (SCM; 75% minimum essential medium (MEM) ×1, 20% normal horse serum heat-inactivated, 30 mM N-2-hydroxyethylpiperazine-N-2-ethane sulfonic acid (HEPES), 13 mM D-glucose, 5.2 mM $NaHCO_3$, 2 mM $MgSO_4$, 1 mM L-glutamine, 1 mM $CaCl_2$, 1 mg/L insulin-transferrin-selenium supplement, 0.004% ascorbic acid, pen/strep) per well.[41] Chronic slices were cultured for 12 days at 37°C and 5% CO_2; SCM was changed every 2 days. From day 13 on, treatment with tumor necrosis factor α (TNF-α; mouse recombinant, lyophilized; Invitrogen) and the 2 different GBCAs (gadopentetate and gadobutrol) was initiated as displayed in Figure 2. To mimic inflammation, TNF-α at 50 ng/mL was added to half of the slices for a 48-hour preincubation period. On day 15, medium was exchanged and either gadopentetate or gadobutrol diluted in SCM was added on the top of the membranes at 1, 10, or 50 mM, respectively. In control cultures, no GBCA was applied. In addition, TNF-α at 50 ng/mL was added again to the corresponding slices for simultaneous coincubation with the GBCAs for an additional 48 hours. In positive control slices only, N-methyl-D-aspartic acid (NMDA) at 50 μM was added on day 16 for 4 hours to induce neurotoxicity.

Tissue Processing and Histology of the Chronic Hippocampal Slices

Treatment of slices with GBCAs ± TNF-α was stopped on day 17 by washing the membranes with fresh SCM. To assess cell death, propidium iodide (PI) was added to each well at 10 μg/mL for 30 minutes at 37°C. Further steps were performed without direct illumination to prevent photobleaching of the PI fluorophore. Subsequently, the membrane inserts were washed twice in prewarmed SCM for 10 minutes, followed by 1-hour fixation in 4% PFA. Thereafter, the membranes were transferred into sucrose (30%) in 0.1 M PBS for 2 days for further fixation. After fixation, slices were removed from the membranes and processed for cryosectioning. Cryostat slicing was performed at a thickness of 20 μm for assessment of the cell death ratio, at 10 μm for imaging mass cytometry (IMC) measurements. To analyze the cell death rate, hippocampal cryosections were counterstained with 4′,6-diamidin-2-phenylindol (DAPI) and subsequently mounted in a mounting medium (Thermo Fisher Scientific, Shandon Immu-Mount). Negative and positive controls were pooled for further analysis using fluorescence microscopy. Three independent rounds of experiments were conducted according to the experimental setup shown in Figure 2.

Fluorescence Microscopy and Toxicity Assay

Fluorescence images were taken from the section of the middle layer of slices and acquired using a Keyence Fluorescence Microscope (BZ-X800, Germany). Overview snapshots at ×2 magnification (CFI Plan Apo Lambda 2x; numerical aperture: 0.10, working distance: 8.50 mm) were taken in the DAPI filter line (BZ-X filter DAPI, model OP-87762; excitation wavelength: 360/40 nm, emission wavelength: 460/50 nm) for orientation. Thereupon, the dentate gyrus (DG) was imaged at ×20 magnification (CFI Plan Apo Lambda 20x; numerical aperture: 0.75, working distance: 1.00 mm). Only those DGs that passed the following criteria were imaged: (1) DG and hippocampal C1 region were distinguishable; (2) the original DG shape was maintained; and (3) neuronal cells of DG were in a good focus and distinguishable. Resulting DGs were imaged for DAPI fluorescence in the DAPI filter line and PI fluorescence in the Texas Red filter line (BZ-X filter TexasRed, model OP-87765; excitation wavelength: 560/40 nm, emission wavelength: 630/75 nm). Photobleaching was minimized by reducing laser power and exposure time between image acquisitions. Per treatment group 8 to 12 DG images were obtained. All images were blindly analyzed using ImageJ software.[40] In stacks combining PI fluorescence and DAPI fluorescence images, manual ROIs around the single DG were drawn and the cell death rate was calculated (%, proportion of PI+ cells to DAPI+ cells). Recounting by independent investigators revealed a mean count-recount difference of 0.18% in cell death rate and a maximal count-recount difference of 1%.

Imaging Mass Cytometry

Gadolinium-based contrast agent penetration within the chronic slices during the 48 hours of incubation was quantified by IMC of 10-μm-thick cryosections. Two untreated control sections, 2 sections treated with 10 mM gadopentetate, and 2 treated with 10 mM gadobutrol were ablated. Before the ablation process, nucleic acids were labeled with Iridium-Cell-IDTM Intercalator (125 μM; Fluidigm, Canada) according to IMC staining protocols (available at www.fluidigm.com) for subsequent colocalization of nucleic acids with elemental Gd. Imaging mass cytometry was performed on a CyTOF2/upgraded to Helios

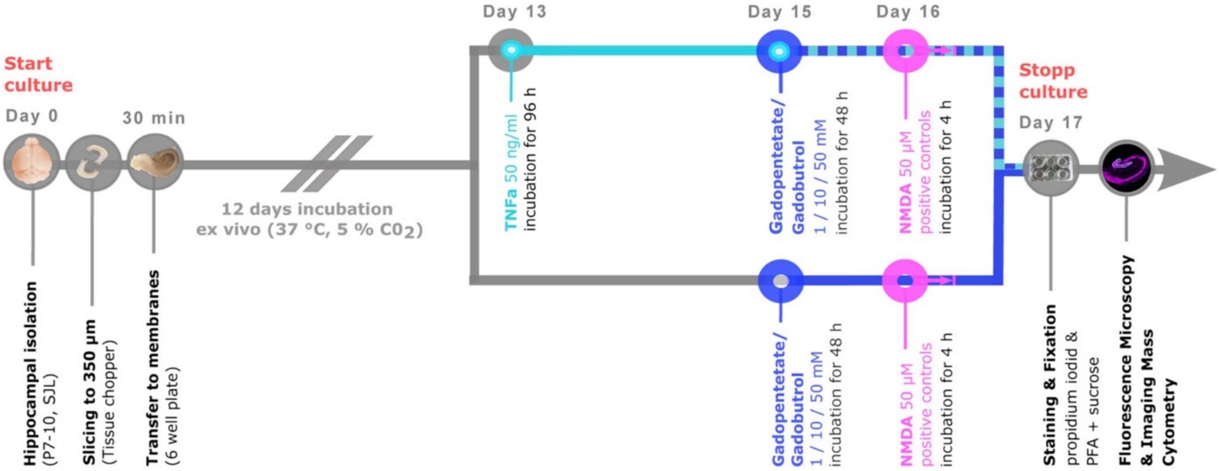

FIGURE 2. Schematic illustration of the ex vivo study design. Organotypic hippocampal slices were incubated for 12 days after initial preparation. On day 13 treatment with TNF-α at 50 ng/mL was started in half of the slices (total incubation time: 96 hours). On day 15, treatment with either gadopentetate or gadobutrol was initiated (total incubation time: 48 hours), whereas simultaneous incubation with TNF-α at 50 ng/mL was continued. Incubation with NMDA for 4 hours was performed in positive control slices only on day 16. On day 17, the chronic cultures were terminated, followed by live staining with PI and further fixation in PFA and sucrose. Cell viability was assessed using fluorescence microscopy; IMC was conducted to visualize Gd tissue content.

specifications coupled to a Hyperion Tissue Imager (Fluidigm, Canada), using CyTOF software version 7.0.8493. The instrument was tuned according to the manufacturer's instructions, using the 3-Element Full Coverage Tuning Slide (Fluidigm, Canada). The dried slide was loaded into the imaging module and ROIs were selected for each sample on a preview (panorama). Optimal laser power was determined for each sample to obtain complete ablation of the tissue. Laser ablation was performed at a resolution of 1 μm and a frequency of 200 Hz in a mass range of 75 to 209 Da. Data were stored as MCD files. For semiquantitative comparison of the elemental content of Gd inside the ablated hippocampal slices, the mean ion count of 6 ROIs per DG of defined size (100 μm × 100 μm) was calculated using the MCD Viewer v1.0.560.6. The mean ion counts of the 2 ablated hippocampal slices per treatment group were averaged.

Statistical Analysis

Data were analyzed using the GraphPad Prism software (version 8.4.3; GraphPad Software, San Diego, California). Normal distribution of the variables was assessed using 3 normality tests (Shapiro-Wilk normality test, D'Agostino and Pearson normality test, and Anderson-Darling test); all data shown here were considered nonparametric. Values are expressed as geometric means and standard deviations. Two-group comparisons were performed by Mann-Whitney tests applying the Bonferroni correction for multiple testing over 3 consecutive time points. Because of the low sample size (n = 2 per group), merely descriptive statistics are shown for ^{158}Gd and ^{66}Zn concentrations measured using LA-ICP-MS and ICP-MS. As this was contemplated as an exploratory pilot study, no formal hypothesis testing was initially planned. Comparisons between more than 2 groups were accomplished by the Kruskal-Wallis test for nonparametric data followed by Dunn's post hoc test for multiple rank comparisons (α power = 0.05). Correlations among T1 relaxation times and the amount of detected Gd in cerebellar tissue were computed by the nonparametric Spearman rank correlation. P values <0.05 were indicative of significant group differences. The significance level of shown data was further displayed as * implying $P < 0.05$, ** implying $P < 0.01$, *** implying $P < 0.001$, and **** implying $P < 0.0001$.

RESULTS

Inflammation Promotes Long-term Gd Retention After Gadopentetate but Not Gadobutrol Application

To assess the effects of neuroinflammation on Gd retention after multiple injections of either linear gadopentetate or macrocyclic gadobutrol, T1 map RARE-VTR magnetic resonance images were acquired at day 1, 10, and 40 pfi (Fig. 3A). T1 relaxation time change (%) was calculated for the different brain areas that have been reported to retain Gd, including cerebellum (C), DN, CN, globus pallidus, thalamus, pons, medulla, hippocampus, and DG (supplementary Figure SDC 1, http://links.lww.com/RLI/A703). Whereas in HC animals, gadopentetate but not gadobutrol applications led to a negative T1 time change in the studied brain areas until 40 days pfi, in the EAE brain areas, both GBCAs appeared to be retained with similar regional distribution, although less pronounced for gadobutrol. Significant differences in T1 time change between inflamed and healthy brains at 24 hours pfi were observed for both linear gadopentetate and macrocyclic gadobutrol. Areas affected included the whole cerebellum, C, DN, CN, globus pallidus, thalamus, pons, medulla, hippocampus, and DG (supplementary Figure SDC 1, http://links.lww.com/RLI/A703).

Especially the cerebellar ROIs (C, DN, and CN) were identified as regions showing differences in T1 relaxation time change (%) between EAE and HC animals, as displayed in Figure 3B. Strikingly, differences between cerebellar ROIs of EAE and HC animals remained significant until 40 days pfi of gadopentetate (C, −10.61% ± 2.87% vs −2.76% ± 3.03%, $P = 0.0477$; DN, −15.13% ± 4.72% vs −3.64% ± 5.94%, $P = 0.0477$; CN, −13.69% ± 4.53% vs −2.64% ± 4.31%, $P = 0.0477$). Within the EAE group, T1 time change even increased when comparing 10 and 40 days pfi of gadopentetate, in particular within the DN and CN, suggesting long-term Gd retention within these areas. Contrary to that, as shown in Figure 3B, 10 and 40 days pfi of gadobutrol, no significant differences between EAE and HC ROIs regarding T1 changes were detected (C, −1.95% ± 3.30% vs 0.83% ± 1.67%; DN, 1.95% ± 4.03% vs 4.95% ± 7.75%; CN, −1.93% ± 3.96% vs −0.33% ± 2.89%), suggesting a continuous clearance of gadobutrol from the brain toward day 40 pfi also in the inflamed tissue.

LA-ICP-MS Confirmed Regional Patterns and Kinetics of Gd Retention in Inflamed Versus Healthy Brains

Gadolinium retention inside the brain, as well as the distribution of different elements including zinc (Zn), copper (Cu), calcium (Ca), phosphorus (P), sulfur (S), manganese (Mn), and iron (Fe), was confirmed and quantified by LA-ICP-MS in representative 10-μm-thick cerebellar cryosections (n = 2 per group). Consecutive H&E-stained sections were imaged for localization of cerebellar ROIs (Fig. 4A).

Confirming MRI data, differences in Gd content between EAE and HC animals were obvious for both administered GBCAs (Fig. 4B). Whereas HC tissues retained Gd strictly limited to the areas of CN (including DN), the EAE cerebella presented Gd additionally localized within the granular layers of the cerebellar cortex, reaching mean Gd concentrations of 41.24 ± 6.97 μM on day 40 pfi of gadopentetate (Fig. 4B). In contrast, administration of gadobutrol led to a qualitatively much lower and diffuse Gd retention around the fourth ventricle (periventricular) and within the choroid plexus, as well as among marginal parts of the cerebellar cortex (Fig. 4B). The highest Gd levels were detected in brains of EAE animals receiving gadopentetate at all given time points of ablation. Gadolinium levels were 2- to 3-fold higher in EAE animals compared with HC mice at all measured time points, that is, 24 hours and 10 and 40 days pfi of gadopentetate, in particular inside the whole cerebellar slice (2.05–3.65-fold), the DN (1.66–2.03-fold), and CN (1.81–2.12-fold) (Fig. 4C). Interestingly, there was a trend of increasing Gd levels at day 40 pfi of gadopentetate in both EAE and HC mouse brains (EAE vs. HC; C, 11.51 ± 0.64 μM vs 3.15 ± 0.24 μM; DN, 49.03 ± 4.73 μM vs 29.46 ± 0.57 μM; CN, 55.06 ± 0.16 μM vs 30.44 ± 4.43 μM).

Regarding gadobutrol, Gd levels inside the C, DN, and CN were approximately 2- to 3-fold higher in EAE animals than HC mice 24 hours pfi. These levels were reduced at day 10 within all assessed brain areas but still higher in EAE. On day 40 pfi, Gd levels diminished to less than 0.40 μM regarding both EAE and HC animals as shown in Figure 4C (EAE vs HC: C, 0.28 ± 0.03 μM vs 0.14 ± 0.04 μM; DN, 0.37 ± 0.08 μM vs 0.17 ± 0.04 μM; CN, 0.38 ± 0.08 μM vs 0.17 ± 0.03 μM).

In particular, in the inflamed CN, administrations of gadopentetate resulted in retention of Gd 24 hours pfi approximately 4-fold higher compared with gadobutrol (DN, 4.43-fold; CN, 4.13-fold) and 7 to 8-fold higher regarding HC (DN, 8.53-fold; CN, 7.14-fold) (Fig. 4C). Differences between both GBCAs became more apparent on day 40, as Gd amounts pfi of gadopentetate were even increased, in contrast to strongly reduced Gd concentrations found after gadobutrol administration (Fig. 4C).

In addition, as shown in the supplementary Figure SDC 2A, http://links.lww.com/RLI/A704, we demonstrated an inverse correlation of Gd concentrations and mean T1 relaxation times for all 3 analyzed cerebellar ROIs, that is C ($r_s = -0.93$, $P < 0.0001$), DN ($r_s = -0.74$, $P = 0.0078$), and CN ($r_s = -0.78$, $P = 0.0043$) (see Supplemental Digital Content, Figure SDC 2A, http://links.lww.com/RLI/A704).

Gd Was Detectable in Blood Samples 40 Days pfi of Both Tested GBCAs

To evaluate the potential mobilization of Gd from organs to the blood circulation during the observation period, Gd concentrations (μg/g blood) in blood samples of EAE mice (n = 2/time point) and HC mice (n = 2/time point) were assessed by ICP-MS. Elevated Gd

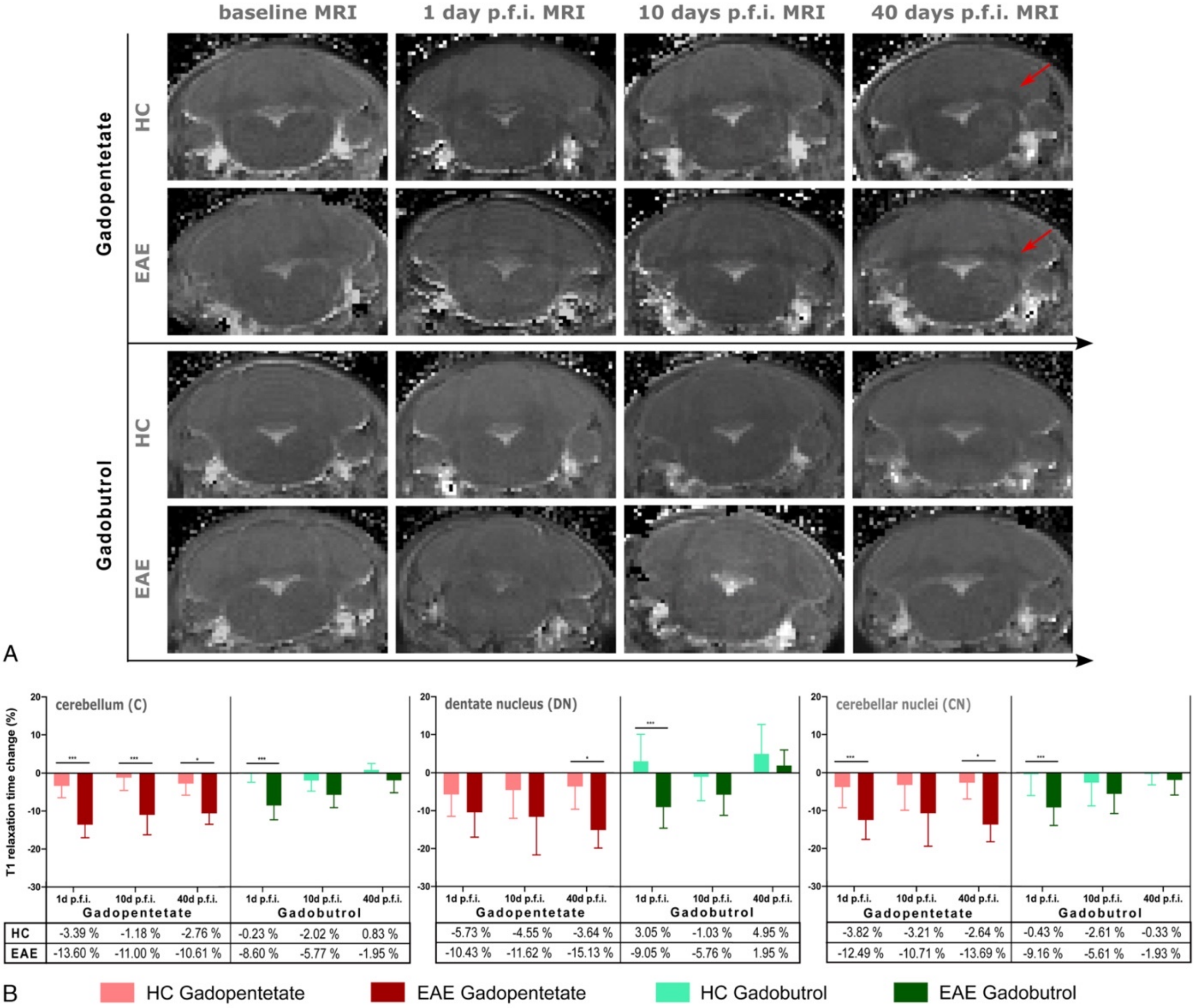

cerebellum (C)

	Gadopentetate 1d p.f.i.	Gadopentetate 10d p.f.i.	Gadopentetate 40d p.f.i.	Gadobutrol 1d p.f.i.	Gadobutrol 10d p.f.i.	Gadobutrol 40d p.f.i.
HC	-3.39 %	-1.18 %	-2.76 %	-0.23 %	-2.02 %	0.83 %
EAE	-13.60 %	-11.00 %	-10.61 %	-8.60 %	-5.77 %	-1.95 %

dentate nucleus (DN)

	Gadopentetate 1d p.f.i.	Gadopentetate 10d p.f.i.	Gadopentetate 40d p.f.i.	Gadobutrol 1d p.f.i.	Gadobutrol 10d p.f.i.	Gadobutrol 40d p.f.i.
HC	-5.73 %	-4.55 %	-3.64 %	3.05 %	-1.03 %	4.95 %
EAE	-10.43 %	-11.62 %	-15.13 %	-9.05 %	-5.76 %	1.95 %

cerebellar nuclei (CN)

	Gadopentetate 1d p.f.i.	Gadopentetate 10d p.f.i.	Gadopentetate 40d p.f.i.	Gadobutrol 1d p.f.i.	Gadobutrol 10d p.f.i.	Gadobutrol 40d p.f.i.
HC	-3.82 %	-3.21 %	-2.64 %	-0.43 %	-2.61 %	-0.33 %
EAE	-12.49 %	-10.71 %	-13.69 %	-9.16 %	-5.61 %	-1.93 %

FIGURE 3. 7 T MRI relaxometry in vivo. A, Representative longitudinal MRI scans (T1 map RARE-VTR sequence) of animals sacrificed 40 days pfi of GBCAs. Relaxometry revealed decreasing T1 relaxation times within the CN (red arrow) toward day 40 pfi of gadopentetate in EAE and HC animals. Gadobutrol-treated animals did not show prominent qualitative T1 shortening within the CN. B, T1 relaxation time change (%) differences between EAE and HC animals within the C, DN, and CN for both tested GBCAs. Mann-Whitney tests were computed for EAE versus HC after gadopentetate or gadobutrol treatment and the Bonferroni correction was applied for multiple testing over 3 consecutive time points. Data are displayed as mean ± SD.

levels were detected in all blood samples at all analyzed time points pfi of both GBCAs, gadopentetate and gadobutrol (supplementary Figure SDC 2B, http://links.lww.com/RLI/A704). In line with Gd content within cerebellar brain slices assessed using LA-ICP-MS, EAE animals showed elevated Gd levels compared with HC animals (except at day 10 pfi of gadopentetate). Maximal Gd concentrations detected corresponded to 0.0054% of the intravenously injected cumulative dose of 20 mmol/kg BW (24 hours pfi of gadopentetate in EAE mice). A negative control sample (untreated age- and sex-matched mouse) demonstrated a very low Gd concentration of 0.0002 μg/g, as shown in the supplementary Figure SDC 2B, http://links.lww.com/RLI/A704. Because of the low sample size (n = 2 per group; HC at day 1 pfi of gadopentetate: n = 1 due to sample contamination) and high variation, only descriptive statistics were performed (see Supplemental Digital Content, Figure SDC 2B, http://links.lww.com/RLI/A704).

LA-ICP-MS Revealed Elevated Zinc Content in Inflamed Mouse Brains

Next, we aimed to identify endogenous metals whose distribution may be affected by inflammation and could be related to Gd retention within cerebellar structures. Interestingly, elevated Zn levels were found in cerebellar slices of EAE animals compared with HC mice at all time points, irrespective of the applied GBCA (Fig. 5A, B). Zn was diffusely distributed in the EAE cerebellar sections at 24 hours pfi of GBCAs, whereas 10 and 40 days pfi, high Zn levels were predominantly located within and around the CN within the white matter and layers of the cerebellar cortex (Fig. 5A). Furthermore, cerebellar EAE slices, as well as HC slices, revealed a decreasing trend in Zn levels toward day 40 pfi. This trend was particularly pronounced in the inflamed DN and CN, irrespective of the applied GBCA, as shown in Figure 5B. Amounts of Zn in

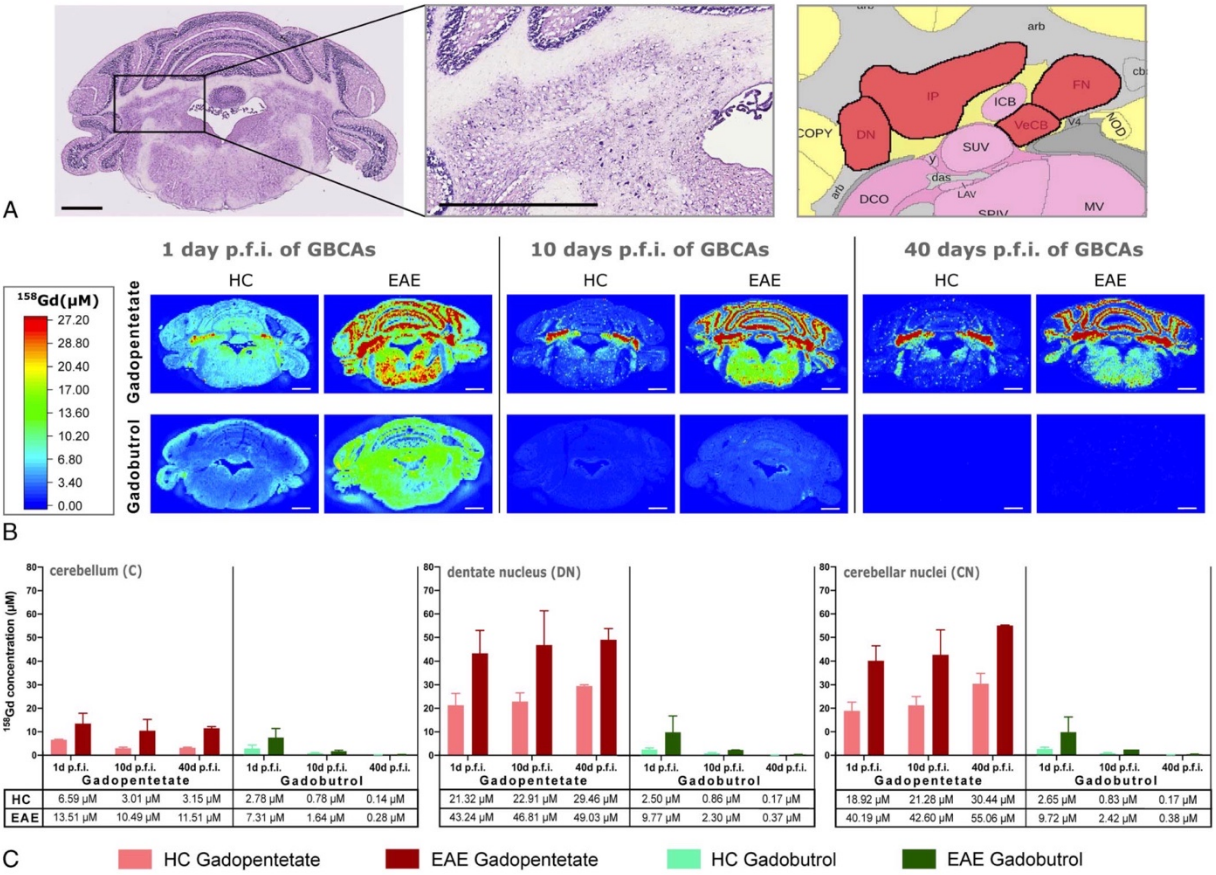

	C Gadopentetate 1d p.f.i.	C Gadopentetate 10d p.f.i.	C Gadopentetate 40d p.f.i.	C Gadobutrol 1d p.f.i.	C Gadobutrol 10d p.f.i.	C Gadobutrol 40d p.f.i.	DN Gadopentetate 1d p.f.i.	DN Gadopentetate 10d p.f.i.	DN Gadopentetate 40d p.f.i.	DN Gadobutrol 1d p.f.i.	DN Gadobutrol 10d p.f.i.	DN Gadobutrol 40d p.f.i.	CN Gadopentetate 1d p.f.i.	CN Gadopentetate 10d p.f.i.	CN Gadopentetate 40d p.f.i.	CN Gadobutrol 1d p.f.i.	CN Gadobutrol 10d p.f.i.	CN Gadobutrol 40d p.f.i.
HC	6.59 μM	3.01 μM	3.15 μM	2.78 μM	0.78 μM	0.14 μM	21.32 μM	22.91 μM	29.46 μM	2.50 μM	0.86 μM	0.17 μM	18.92 μM	21.28 μM	30.44 μM	2.65 μM	0.83 μM	0.17 μM
EAE	13.51 μM	10.49 μM	11.51 μM	7.31 μM	1.64 μM	0.28 μM	43.24 μM	46.81 μM	49.03 μM	9.77 μM	2.30 μM	0.37 μM	40.19 μM	42.60 μM	55.06 μM	9.72 μM	2.42 μM	0.38 μM

FIGURE 4. Analysis of Gd distribution using LA-ICP-MS. A, On the left, H&E bright field image of cerebellar slice containing the CN corresponding to LA-ICP-MS tissue layer at ×2 magnification; CNs are additionally displayed at ×10 magnification. On the right, Allen brain atlas correlation image of CN formation. Nuclei from lateral to medial: DN, interposed nucleus (IP), vestibulocerebellar nucleus (VeCB), fastigial nucleus (FN). Scale bars: 1 mm. B, LA-ICP-MS images showing Gd distribution in cerebellar slices. Red areas display high and blue areas low Gd content (μM). Scale bars: 1 mm. C, Gd concentrations measured within the whole C, DN, or CN in μM of brain volume. Because of the low sample size, merely descriptive statistics are shown (mean ± SD).

EAE brains regarding the C, DN, and CN decreased by 25%, 26%, and 26%, respectively, whereas in HC brains, Zn levels decreased by 14%, 21%, and 22%, respectively, toward day 40 pfi (Fig. 5B).

The overall distribution of Cu, Ca, P, S, Mn, and Fe concentrations seemed to be unaffected by inflammation (supplementary Figure SDC 3, http://links.lww.com/RLI/A705). However, areas with high Gd content overlapped with areas of high Fe levels (see Supplemental Digital Content, Figure SDC 3, http://links.lww.com/RLI/A705).

Gadopentetate but Not Gadobutrol Exerts a Neurotoxic Effect on Living Organotypic Hippocampal Slices

To assess the potential toxicity of GBCAs, we measured the cell death rate (%) after 48-hour treatment of chronic hippocampal slices with gadopentetate or gadobutrol at 1, 10, and 50 mM, respectively (Fig. 6). To simulate neuroinflammatory conditions, TNF-α at 50 ng/mL was added to half of the slices. Gadopentetate promoted cell death within the DG only at 50 mM (Fig. 6A, B). No toxicity was observed for gadobutrol. Tumor necrosis factor α at 50 ng/mL enhanced the gadopentetate-induced cell death rate significantly (with vs without TNF-α: 3.15% ± 01.18% vs 2.17% ± 1.14%; $P = 0.0345$), as shown in Figure 6B. NMDA incubation at 50 μM served as a positive control. Its neurotoxic effect was also increased by TNF-α (34.34% ± 11.14% vs 19.70% ± 9.19%; $P = 0.0002$) (Fig. 6B).

To examine whether the lack of cytotoxicity of GBCAs at especially lower concentrations was caused by deficient penetration of the compounds into the living slices, IMC was performed using slices treated with 10 mM of GBCAs. Gadolinium was detectable inside hippocampal slices after treatment with both GBCAs, gadopentetate and gadobutrol (Fig. 6C). However, the mean ^{158}Gd count inside the DG region was 26 times higher in slices treated with gadopentetate than in those treated with gadobutrol (6.07 ± 1.32 ion count vs 0.23 ± 0.02 ion count). Nevertheless, the mean ion count for ^{158}Gd within the gadobutrol-treated slices was still on average 12 times higher compared with untreated control slices (0.23 ± 0.02 ion count vs 0.02 ± 0.01 ion count). Interestingly, in gadopentetate-treated slices, detected $^{191,\,193}$Ir (labels nucleic acids) colocalized with areas of high ^{158}Gd counts within the DG (Fig. 6C).

DISCUSSION

We demonstrated previously that after repeated applications of gadopentetate, neuroinflammation favors the retention of Gd within

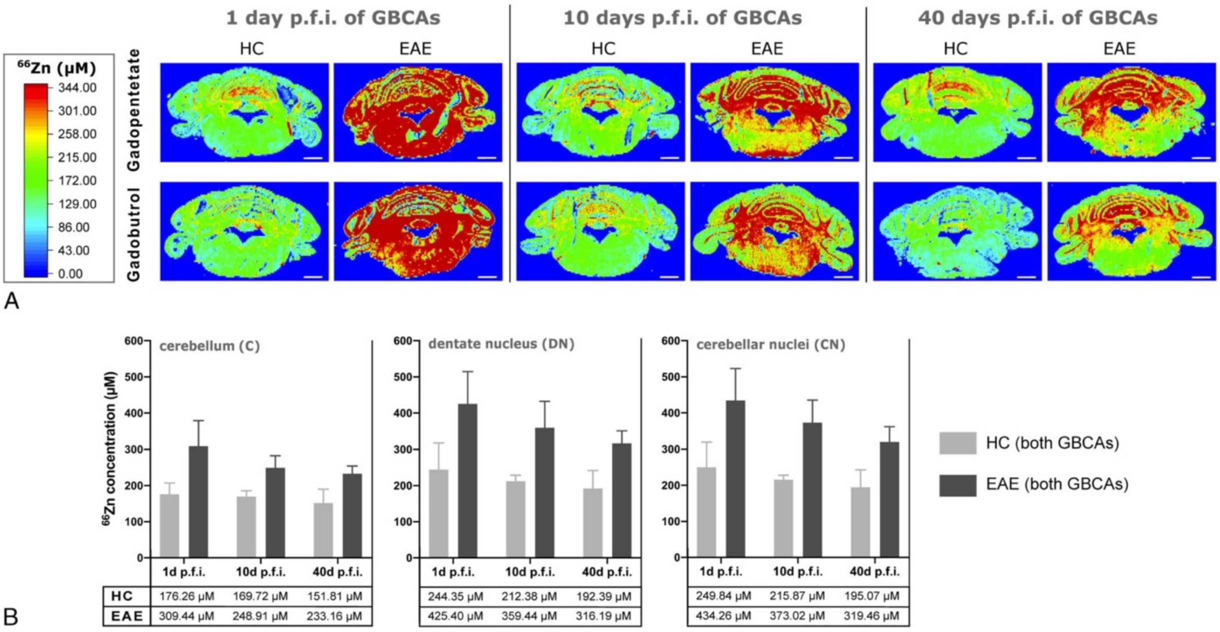

	1d p.f.i.	10d p.f.i.	40d p.f.i.	1d p.f.i.	10d p.f.i.	40d p.f.i.	1d p.f.i.	10d p.f.i.	40d p.f.i.
HC	176.26 µM	169.72 µM	151.81 µM	244.35 µM	212.38 µM	192.39 µM	249.84 µM	215.87 µM	195.07 µM
EAE	309.44 µM	248.91 µM	233.16 µM	425.40 µM	359.44 µM	316.19 µM	434.26 µM	373.02 µM	319.46 µM

FIGURE 5. Analysis of elemental colocalization using LA-ICP-MS. A, Laser ablation images of cerebellar Zn distribution. Red areas display high and blue areas low Zn content (µM). The EAE animals in both GBCA groups showed qualitatively higher Zn levels compared with HC. Scale bars: 1 mm. B, Demonstration of Zn levels within the whole C, the DN, and CN (µM). The EAE animals consistently presented higher elemental Zn levels than HC animals irrespective of the applied GBCA with a tendency to decrease toward day 40 pfi of GBCAs.

the CNS in vivo.[37] Here, in a murine model of multiple sclerosis as well as in living brain tissue, we compared the linear gadopentetate and the macrocyclic gadobutrol in terms of dynamics and patterns of inflammation-promoted Gd retention in vivo as well as potential cytotoxic effects ex vivo. Using T1 relaxometry and LA-ICP-MS, we found that gadopentetate was retained in the brain up to 40 days pfi, whereas gadobutrol was efficiently washed out toward day 40 pfi. Although for both GBCAs inflammation favored enhanced Gd retention within cerebellar structures, gadopentetate led to much larger Gd brain retention compared with gadobutrol. Finally, using an ex vivo model of neuronal tissue, we showed that gadopentetate but not gadobutrol induced cell death in the living brain tissue and that this process was enhanced in the presence of the inflammatory mediator TNF-α.

Our study revealed significantly decreased T1 relaxation times after multiple injections of GBCAs in EAE brains compared with HC. T1 relaxometry is a robust tool to study MRI alterations related to Gd retention after administration of GBCAs in a quantitative manner,[42,43] without the need for a reference region, which in itself may be a confounding factor.[13,44] Using the well-established ABA registration tool, we chose an automated approach to identify T1 relaxation decreases within different brain areas, ensuring higher validity and comparability. The LA-ICP-MS data confirmed the relaxometry findings, as cerebellar Gd levels in EAE mice were 2- to 3-fold higher than in HC mice and within the range previously reported by us and others.[15,37,45] Maximal Gd contents inside the CN and DN after repeated injections of gadopentetate corresponded to approximately 4.51 µg/g in HC mice and 8.28 µg/g in EAE mice (30 µM and 55 µM, respectively).

Comparing the 2 applied GBCAs overtime, LA-ICP-MS data confirmed that neuroinflammation enhanced Gd retention especially after gadopentetate administration. We observed a long-term retention in the EAE cerebellum and its nuclei, and to a lower extent also in HC brains, up to 40 days pfi of the linear compound. However, gadobutrol administration led to a rather low and transient retention of Gd until day 10 pfi, which was also enhanced during inflammation but was completely cleared from the brain at day 40 pfi. Recent studies demonstrated a nonpermanent retention of macrocyclic GBCAs[33,34,46,47] with clearance rates dependent on the specific washout kinetics.[33,34] Frenzel et al suggested that gadobutrol remained in its intact form inside the body as it was exclusively present in the soluble fraction of the brain as a low-molecular-weight molecule. In contrast, linear GBCAs at day 24 pfi were present to a large extent in an insoluble form, whereas in its soluble fraction, a portion of Gd was bound to large macromolecules, suggesting that Gd had dissociated from the chelate.[15] These findings were confirmed in recent rodent studies.[45,48,49]

We speculate that BBB disruption[37] and/or alterations of the choroid plexus[50] occurring during EAE contribute to the enhanced entry of GBCA into the brain, whereas inflammation-mediated tissue alterations[51–54] may promote enhanced Gd retention. In healthy individuals, Gd retention inside the brain seems to be the result of an entry of GBCA through the blood-CSF barrier[55] at the choroid plexus and from the CSF via the glymphatic system,[56–59] into the brain. Along these lines, Öner et al[60] reported on DN T1 hyperintensities after only a single intrathecal injection of gadopentetate in patients with normal renal function. It has been shown that alterations of the choroid plexus observed in multiple sclerosis[61] and EAE[62] may contribute to CNS pathology. Thus, an enhanced entry of GBCA into the CSF via the inflamed choroid plexus could be assumed.

Moreover, BBB breakdown is considered an early hallmark in multiple sclerosis that permits large CNS infiltration of peripheral activated autoreactive lymphocytes into the CNS. In addition, inflammation-related release of chemokines, free radicals, activated matrix metalloproteinases (MMP) and the consequent enhanced extravasation of immune cells may further compromise BBB integrity.[63] Blood-brain barrier disruption occurs in a similar way in the EAE model, in which T lymphocytes have been demonstrated to induce tight junction alterations in BBB endothelium initiating barrier disruption and enhanced permeability.[64,65] Whereas a leaky BBB may result in elevated GBCA diffusion, additional cellular and tissue

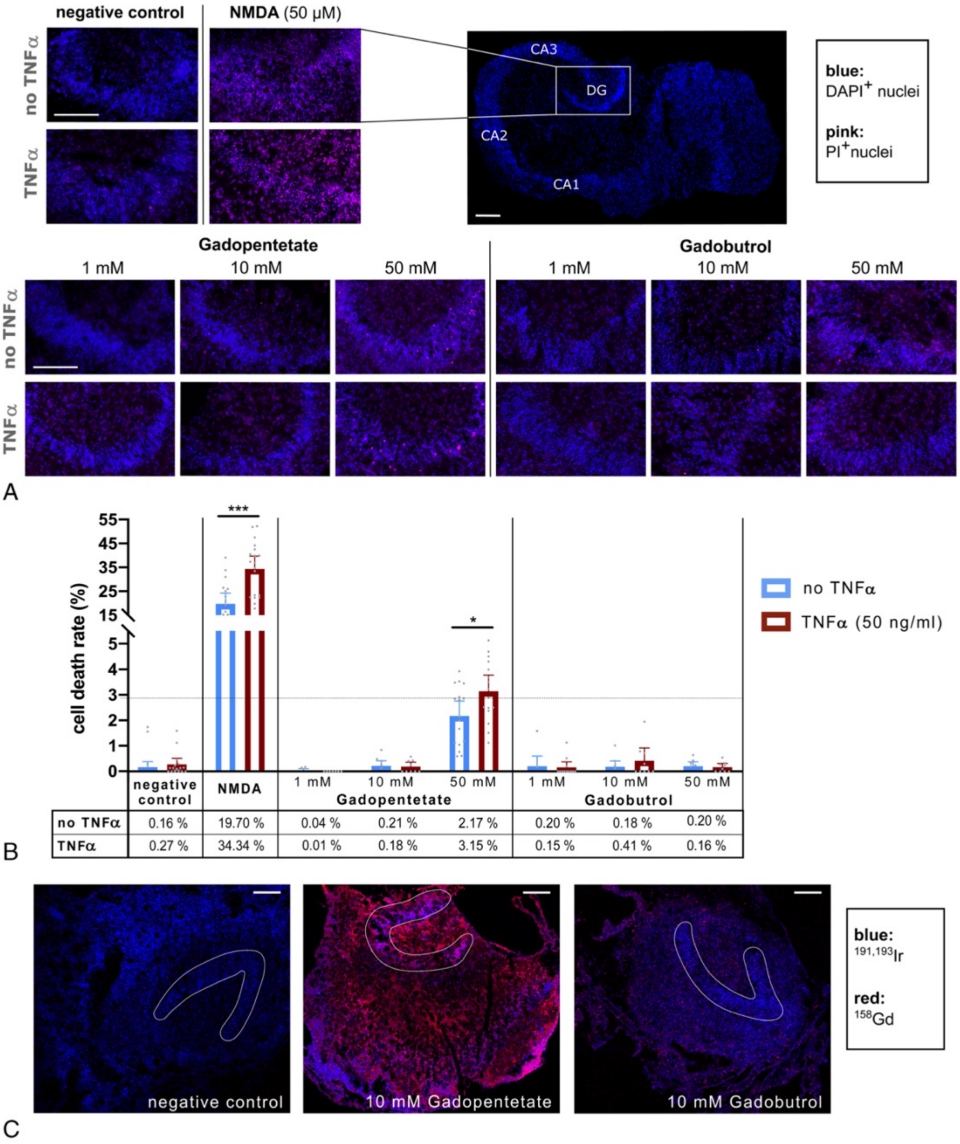

	negative control	NMDA	1 mM Gadopentetate	10 mM Gadopentetate	50 mM Gadopentetate	1 mM Gadobutrol	10 mM Gadobutrol	50 mM Gadobutrol
no TNFα	0.16 %	19.70 %	0.04 %	0.21 %	2.17 %	0.20 %	0.18 %	0.20 %
TNFα	0.27 %	34.34 %	0.01 %	0.18 %	3.15 %	0.15 %	0.41 %	0.16 %

FIGURE 6. Toxicity of GBCAs on organotypic hippocampal slices. A, Representative fluorescence images of the DG; all nuclei in blue (DAPI), dead nuclei in red (PI). The DGs of slices coincubated with/without TNF-α (50 ng/mL) are displayed for all experimental conditions. The PI-positive cells appear in NMDA-treated (±TNF-α) and gadopentetate-treated slices at 50 mM (±TNF-α). Scale bars: 200 µm. B, Cell death rate (%) was elevated in NMDA (positive control)-treated slices and slices treated with 50 mM gadopentetate. Tumor necrosis factor α enhanced cell death rate significantly. Data were evaluated using Mann-Whitney tests (mean ± SD). C, IMC images of 10-µm-thick slices after gadopentetate or gadobutrol treatment at 10 mM and negative control. The DGs were surrounded by manually drawn ROIs (white), and thresholds were adjusted for optimal visualization. Scale bars: 200 µm.

alterations such as demyelination, microglial activation, changes in elemental metal distribution, or/and alterations of the extracellular matrix may contribute to enhanced retention. In this context, it has been suggested that inflammation-mediated alterations in the extracellular matrix composition such as glycosaminoglycans (GAGs) may favor GBCA dechelation and parenchymal retention of Gd.[37] We previously reported that in EAE, inflammation-induced modifications of GAG sulfation on brain endothelial cells facilitate the uptake of very small superparamagnetic iron oxide nanoparticles.[51] The GAG network on endothelial cells of vessels may act as an ion exchanger with complexing abilities.[66] Interestingly, the DN was found to contain elevated amounts of microvessels that may bind Gd[23] and to be enriched in endogenous metals such as Fe, Cu, and Zn that may facilitate transmetallation processes.[67]

Strikingly, we observed increasing Gd levels within the CN (DN included) from day 10 to day 40 pfi, which was observed also in HC but was more pronounced in the EAE animals. We speculate that this increase over time within the CN on day 10 and 40 pfi may be the result of a release of Gd^{3+} from other storage organs such as the bones.[3,68–70]

Stable Gd retention inside the bone has been reported for a period of more than 8 years most likely caused by the transmetallation of Gd^{3+} with resident calcium ions.[69,71] Thakral and Abraham[72] reported on increasing Gd amounts in sequential skin biopsies of patients with nephrogenic systemic fibrosis although no more GBCA was administered. Bone storage may also contribute to maintain Gd tissue levels by its mobilization into the bloodstream, since it was reported that Gd was still detectable in the red blood cell compartment 10 days pfi of principally linear GBCAs.[18] Our ICP-MS analysis of blood samples revealed indeed that Gd was present in all samples up to day 40 pfi within the same range as detected in the cerebellum (approximately 0.2–2.0 μg/g). This supports the hypothesis of long-term retention, release, and recirculation of Gd through the body according to the Le Chatelier principle.[73]

We also showed that Zn levels in EAE brains were elevated compared with HC brains irrespective of the administered GBCA at all investigated time points. It has been suggested that disruption of brain Zn homeostasis may play an active role in the pathogenesis of multiple sclerosis and EAE.[74,75] Zn acts as a cofactor for numerous enzymes like MMPs, is component of various proteins including myelin basic protein,[74] and was reported to induce mitochondrial production of reactive oxygen species.[75] Hence, increased neuronal Zn release may lead to MMP activation compromising BBB integrity and mediate neuronal injury. In this line, Choi et al[75] reported on decreased BBB impairment and reduced immune cell infiltration and myelin destruction in the spinal cord of EAE mice after oral zinc chelator application.

We further observed that cerebellar Zn concentrations decreased until day 40 pfi, whereas Gd levels increased. Several studies reported on Zn depletion due to transmetallation with Gd and resulting zincuria after injections of linear GBCAs.[31,76,77] Thus, increased Zn content in EAE brains may lead to elevated transmetallation rates with administered Gd and therefore facilitate its retention.

Furthermore, we investigated how GBCAs may affect cell viability using a model of organotypic hippocampal slice cultures in which the 3-dimensional histological architecture and cellular composition of neuronal tissue are well preserved.[78] We demonstrated that tissue retention of Gd was 26-fold higher after gadopentetate incubation compared with gadobutrol as measured by IMC and that gadopentetate induced neural death. Preincubation and coincubation of chronic hippocampal cultures with TNF-α at 50 ng/mL increased cell death induced by gadopentetate but did not influence gadobutrol effects. This finding underlines the hypothesis that not only an impaired BBB but also tissue alterations attributable to a proinflammatory milieu may cause elevated Gd retention in the CNS. Tumor necrosis factor α is a pleiotropic cytokine playing an essential role in the immunopathogenesis of multiple sclerosis and EAE[64] that is widely used in in vitro paradigms of inflammation.[51] In our ex vivo model, TNF-α may increase GBCA toxicity by enhancing cell death–inducing pathways as part of its immunomodulatory capacity.[64,79] However, it cannot be excluded that TNF-α triggers a decreased chelate stability owing to changes in endogenous ions resulting in a dose-dependent increase in GBCA-induced toxicity.[80] Our findings are consistent with a recent study that demonstrated toxicity for linear GBCAs in vitro in human dopaminergic neurons.[81] Moreover, Xia et al[82] observed that Gd chloride (20 μM) reduced cell viability and led to rapid accumulation of intracellular calcium and reactive oxygen species. However, the in vivo relevance of those findings remains unclear. Whereas Radbruch et al[83] reported on reduced intraepidermal nerve fiber density in mice after a single application of linear GBCAs and to a lesser extent after macrocyclic GBCAs, Davies et al, among others,[19,25,84,85] did not detect any histopathological changes suggestive of neurotoxicity in rat tissue after multiple injections of gadodiamide. Furthermore, in vivo administration of gadodiamide did not lead to persistent clinical and behavioral alterations in healthy rats.[85] Nevertheless, further investigations on the genotoxic potential of GBCAs are needed, as Gd retention was found inside nuclei of neuronal cells.[22] Our IMC measurements showed that Gd retained inside the DG was colocalized with Ir-tagged nucleic acids. However, because of limited image resolution, we were not able to differentiate between an intracellular or extracellular location of retained Gd.

It is uncertain whether Gd retention may promote neuronal alterations in vivo and lead, for instance, to additional clinical impairment in patients with multiple sclerosis.[42,86–89] Only a few studies reported an increase in clinical disability after GBCA administration.[42,88] Further investigations are needed to determine to what extent parenchymal retention of potentially dissociating and, hence, toxic Gd^{3+} represents a long-term hazard in particular for patients with neuroinflammatory diseases.

Limitations of the Study

Although the EAE recapitulates many of the pathological hallmarks of multiple sclerosis, the pattern of GBCA administration (8 injections in 10 days), the high dosage (single daily dose of 2.5 mmol/kg BW), and the time points selected for long-term measures (up to 40 days pfi of GBCAs) represent a well-established rodent paradigm[16,17,25,37,90] but differ considerably from the reality in patients in terms of concentrations and time frame of the applications. Moreover, the sample size of n = 2 animals per group for LA-ICP-MS measurements was too small to make any quantitative statement about Gd retention but did show obvious and consistent qualitative trends in EAE versus HC animals. In addition, we did not conduct any structural analysis on Gd retained in the tissue and cannot distinguish between intact GBCA, free Gd^{3+}, and Gd bound in insoluble deposits or to soluble macromolecules. Further studies are currently ongoing to clarify this important issue. Finally, using the technique of chronic slice culture for toxicity assessment, initially applied GBCA concentrations ex vivo were approximately 1000-fold higher than Gd concentrations identified inside the CN and DN in vivo using LA-ICP-MS. However, we were not able to determine the specific gadopentetate concentration that infiltrated the chronic tissue slices and consequently led to neuronal cell death within the DG or the mechanisms, leading to increased cell death with simultaneous TNF-α incubation. This should be also assessed in future studies. Furthermore, because of fixation and staining procedures on hippocampal slices, a partial washout of intact GBCA cannot be excluded. Nevertheless, we here aimed to assess tissue-bound Gd potentially leading to neurotoxicity of DG neuronal cells rather than measuring additional intact GBCA amounts.

CONCLUSIONS

Using in vivo MRI and LA-ICP-MS, we studied the effect of inflammation on the long-term retention and cerebellar distribution of Gd after repeated administration of linear gadopentetate and macrocyclic gadobutrol. The kinetics of Gd retention and ICP-MS analysis of blood samples indicated that Gd from gadopentetate may be stored in nonneuronal tissue and recirculated through the body for a long time after the last GBCA application. In addition, regarding gadobutrol, we showed that inflammation led to a nonpermanent Gd retention most likely owing to an increased influx into the cerebellum of EAE mice, which was efficiently cleared over time. Finally, using living brain tissue, we demonstrated that gadopentetate but not gadobutrol induced cell death within the chronic hippocampal slices; a process that was also increased in an inflammatory milieu. Thus, our study confirmed the higher kinetic stability of macrocyclic GBCAs compared with the linear compounds in vivo. Although macrocyclic GBCAs do not seem to cause long-term Gd retention either in inflamed or in healthy brain parenchyma, there is a substantial need to elucidate the mechanisms causing enhanced retention inside inflamed brain parenchyma and to determine if even transient short-term Gd retention after the use of kinetically more stable agents may exert toxic effects on inflamed brain tissue in vivo.

ACKNOWLEDGMENTS

The authors thank Natascha Asselborn for the expert technical assistance. Lina Anderhalten acknowledges financial support from the Hertie Foundation (medMS program).

REFERENCES

1. Hao D, Ai T, Goerner F, et al. MRI contrast agents: basic chemistry and safety. *J Magn Reson Imaging*. 2012;36:1060–1071.
2. Do QN, Lenkinski RE, Tircso G, et al. How the chemical properties of GBCAs influence their safety profiles in vivo. *Molecules*. 2021;27:58.
3. Runge VM. Dechelation (transmetalation): consequences and safety concerns with the linear gadolinium-based contrast agents, in view of recent health care rulings by the EMA (Europe), FDA (United States), and PMDA (Japan). *Invest Radiol*. 2018;53:571–578.
4. European Medicines Agency. EMA's final opinion confirms restrictions on use of linear gadolinium agents in body scan. 2017. https://www.ema.europa.eu/en/news/emas-final-opinion-confirms-restrictions-use-linear-gadolinium-agents-body-scans. Assessed March 2, 2022.
5. US Food and Drug Administration. FDA warns that gadolinium-based contrast agents (GBCAs) are retained in the body; requires new class warnings. 2017. https://www.fda.gov/drugs/drug-safety-and-availability/fda-drug-safety-communication-fda-warns-gadolinium-based-contrast-agents-gbcas-are-retained-body. Accessed March 2, 2022.
6. Kanda T, Ishii K, Kawaguchi H, et al. High signal intensity in the dentate nucleus and globus pallidus on unenhanced T1-weighted MR images: relationship with increasing cumulative dose of a gadolinium-based contrast material. *Radiology*. 2014;270:834–841.
7. Errante Y, Cirimele V, Mallio CA, et al. Progressive increase of T1 signal intensity of the dentate nucleus on unenhanced magnetic resonance images is associated with cumulative doses of intravenously administered gadodiamide in patients with normal renal function, suggesting dechelation. *Invest Radiol*. 2014;49:685–690.
8. Quattrocchi CC, Mallio CA, Errante Y, et al. Gadodiamide and dentate nucleus T1 hyperintensity in patients with meningioma evaluated by multiple follow-up contrast-enhanced magnetic resonance examinations with no systemic interval therapy. *Invest Radiol*. 2015;50:470–472.
9. Radbruch A, Weberling LD, Kieslich PJ, et al. High-signal intensity in the dentate nucleus and globus pallidus on unenhanced T1-weighted images: evaluation of the macrocyclic gadolinium-based contrast agent gadobutrol. *Invest Radiol*. 2015;50:805–810.
10. Weberling LD, Kieslich PJ, Kickingereder P, et al. Increased signal intensity in the dentate nucleus on unenhanced T1-weighted images after gadobenate dimeglumine administration. *Invest Radiol*. 2015;50:743–748.
11. Ramalho J, Castillo M, AlObaidy M, et al. High signal intensity in globus pallidus and dentate nucleus on unenhanced T1-weighted MR images: evaluation of two linear gadolinium-based contrast agents. *Radiology*. 2015;276:836–844.
12. Cao Y, Huang DQ, Shih G, et al. Signal change in the dentate nucleus on T1-weighted MR images after multiple administrations of gadopentetate dimeglumine versus gadobutrol. *AJR Am J Roentgenol*. 2016;206:414–419.
13. Robert P, Lehericy S, Grand S, et al. T1-weighted hypersignal in the deep cerebellar nuclei after repeated administrations of gadolinium-based contrast agents in healthy rats: difference between linear and macrocyclic agents. *Invest Radiol*. 2015;50:473–480.
14. Robert P, Violas X, Grand S, et al. Linear gadolinium-based contrast agents are associated with brain gadolinium retention in healthy rats. *Invest Radiol*. 2016;51:73–82.
15. Frenzel T, Apte C, Jost G, et al. Quantification and assessment of the chemical form of residual gadolinium in the brain after repeated administration of gadolinium-based contrast agents: comparative study in rats. *Invest Radiol*. 2017;52:396–404.
16. Lohrke J, Frisk AL, Frenzel T, et al. Histology and gadolinium distribution in the rodent brain after the administration of cumulative high doses of linear and macrocyclic gadolinium-based contrast agents. *Invest Radiol*. 2017;52:324–333.
17. Jost G, Frenzel T, Boyken J, et al. Long-term excretion of gadolinium-based contrast agents: linear versus macrocyclic agents in an experimental rat model. *Radiology*. 2019;290:340–348.
18. Di Gregorio E, Furlan C, Atlante S, et al. Gadolinium retention in erythrocytes and leukocytes from human and murine blood upon treatment with gadolinium-based contrast agents for magnetic resonance imaging. *Invest Radiol*. 2020;55:30–37.
19. Davies J, Marino M, Smith APL, et al. Repeat and single dose administration of gadodiamide to rats to investigate concentration and location of gadolinium and the cell ultrastructure. *Sci Rep*. 2021;11:13950.
20. McDonald RJ, McDonald JS, Kallmes DF, et al. Intracranial gadolinium deposition after contrast-enhanced MR imaging. *Radiology*. 2015;275:772–782.
21. Kanda T, Fukusato T, Matsuda M, et al. Gadolinium-based contrast agent accumulates in the brain even in subjects without severe renal dysfunction: evaluation of autopsy brain specimens with inductively coupled plasma mass spectroscopy. *Radiology*. 2015;276:228–232.
22. McDonald RJ, McDonald JS, Kallmes DF, et al. Gadolinium deposition in human brain tissues after contrast-enhanced MR imaging in adult patients without intracranial abnormalities. *Radiology*. 2017;285:546–554.
23. Fingerhut S, Sperling M, Holling M, et al. Gadolinium-based contrast agents induce gadolinium deposits in cerebral vessel walls, while the neuropil is not affected: an autopsy study. *Acta Neuropathol*. 2018;136:127–138.
24. El-Khatib AH, Radbruch H, Trog S, et al. Gadolinium in human brain sections and colocalization with other elements. *Neurol Neuroimmunol Neuroinflamm*. 2019;6:e515.
25. El Hamrani D, Vives V, Buchholz R, et al. Effect of long-term retention of gadolinium on metabolism of deep cerebellar nuclei after repeated injections of gadodiamide in rats. *Invest Radiol*. 2020;55:120–128.
26. Radbruch A, Richter H, Fingerhut S, et al. Gadolinium deposition in the brain in a large animal model: comparison of linear and macrocyclic gadolinium-based contrast agents. *Invest Radiol*. 2019;54:531–536.
27. Frenzel T, Lengsfeld P, Schirmer H, et al. Stability of gadolinium-based magnetic resonance imaging contrast agents in human serum at 37 degrees C. *Invest Radiol*. 2008;43:817–828.
28. Port M, Idee JM, Medina C, et al. Efficiency, thermodynamic and kinetic stability of marketed gadolinium chelates and their possible clinical consequences: a critical review. *Biometals*. 2008;21:469–490.
29. Idée JM, Port M, Raynal I, et al. Clinical and biological consequences of transmetallation induced by contrast agents for magnetic resonance imaging: a review. *Fundam Clin Pharmacol*. 2006;20:563–576.
30. Telgmann L, Wehe CA, Kunnemeyer J, et al. Speciation of Gd-based MRI contrast agents and potential products of transmetalation with iron ions or parenteral iron supplements. *Anal Bioanal Chem*. 2012;404:2133–2141.
31. Boyken J, Frenzel T, Lohrke J, et al. Impact of treatment with chelating agents depends on the stability of administered GBCAs: a comparative study in rats. *Invest Radiol*. 2019;54:76–82.
32. Robert P, Fingerhut S, Factor C, et al. One-year retention of gadolinium in the brain: comparison of gadodiamide and gadoterate meglumine in a rodent model. *Radiology*. 2018;288:424–433.
33. Bussi S, Coppo A, Botteron C, et al. Differences in gadolinium retention after repeated injections of macrocyclic MR contrast agents to rats. *J Magn Reson Imaging*. 2018;47:746–752.
34. Bussi S, Coppo A, Celeste R, et al. Macrocyclic MR contrast agents: evaluation of multiple-organ gadolinium retention in healthy rats. *Insights Imaging*. 2020;11:11.
35. Giorgio A, De Stefano N. Effective utilization of MRI in the diagnosis and management of multiple sclerosis. *Neurol Clin*. 2018;36:27–34.
36. Wattjes MP, Ciccarelli O, Reich DS, et al. 2021 MAGNIMS-CMSC-NAIMS consensus recommendations on the use of MRI in patients with multiple sclerosis. *Lancet Neurol*. 2021;20:653–670.
37. Wang S, Hesse B, Roman M, et al. Increased retention of gadolinium in the inflamed brain after repeated administration of gadopentetate dimeglumine: a proof-of-concept study in mice combining ICP-MS and micro- and nano-SR-XRF. *Invest Radiol*. 2019;54:617–626.
38. Koch S, Mueller S, Foddis M, et al. Atlas registration for edema-corrected MRI lesion volume in mouse stroke models. *J Cereb Blood Flow Metab*. 2019;39:313–323.
39. Stärk HJ, Wennrich R. A new approach for calibration of laser ablation inductively coupled plasma mass spectrometry using thin layers of spiked agarose gels as references. *Anal Bioanal Chem*. 2011;399:2211–2217.
40. Schneider CA, Rasband WS, Eliceiri KW. NIH image to ImageJ: 25 years of image analysis. *Nat Methods*. 2012;9:671–675.
41. Opitz-Araya X, Barria A. Organotypic hippocampal slice cultures. *J Vis Exp*. 2011;2462.
42. Forslin Y, Martola J, Bergendal Å, et al. Gadolinium retention in the brain: an MRI relaxometry study of linear and macrocyclic gadolinium-based contrast agents in multiple sclerosis. *AJNR Am J Neuroradiol*. 2019;40:1265–1273.
43. Deike-Hofmann K, Reuter J, Haase R, et al. No changes in T1 relaxometry after a mean of 11 administrations of gadobutrol. *Invest Radiol*. 2020;55:381–386.
44. Jost G, Lenhard DC, Sieber MA, et al. Signal increase on unenhanced T1-weighted images in the rat brain after repeated, extended doses of gadolinium-based contrast agents: comparison of linear and macrocyclic agents. *Invest Radiol*. 2016;51:83–89.
45. Strzeminska I, Factor C, Jimenez-Lamana J, et al. Comprehensive speciation analysis of residual gadolinium in deep cerebellar nuclei in rats repeatedly administered with gadoterate meglumine or gadodiamide [published online ahead of print January 19, 2022]. *Invest Radiol*. doi:10.1097/RLI.0000000000000846.
46. Frenzel T, Ulbrich HF, Pietsch H. The macrocyclic gadolinium-based contrast agents gadobutrol and gadoteridol show similar elimination kinetics from the brain after repeated intravenous injections in rabbits. *Invest Radiol*. 2021;56:341–347.
47. Strzeminska I, Factor C, Robert P, et al. Long-term evaluation of gadolinium retention in rat brain after single injection of a clinically relevant dose of gadolinium-based contrast agents. *Invest Radiol*. 2020;55:138–143.

48. Gianolio E, Bardini P, Arena F, et al. Gadolinium retention in the rat brain: assessment of the amounts of insoluble gadolinium-containing species and intact gadolinium complexes after repeated administration of gadolinium-based contrast agents. *Radiology.* 2017;285:839–849.
49. Strzeminska I, Factor C, Robert P, et al. Speciation analysis of gadolinium in the water-insoluble rat brain fraction after administration of gadolinium-based contrast agents. *Invest Radiol*. 2021;56:535–544.
50. Millward JM, Schnorr J, Taupitz M, et al. Iron oxide magnetic nanoparticles highlight early involvement of the choroid plexus in central nervous system inflammation. *ASN Neuro*. 2013;5:e00110.
51. Berndt D, Millward JM, Schnorr J, et al. Inflammation-induced brain endothelial activation leads to uptake of electrostatically stabilized iron oxide nanoparticles via sulfated glycosaminoglycans. *Nanomedicine*. 2017;13:1411–1421.
52. Millward JM, Ariza de Schellenberger A, Berndt D, et al. Application of europium-doped very small Iron oxide nanoparticles to visualize Neuroinflammation with MRI and fluorescence microscopy. *Neuroscience*. 2019;403:136–144.
53. Silva RV, Morr AS, Mueller S, et al. Contribution of tissue inflammation and blood-brain barrier disruption to brain softening in a mouse model of multiple sclerosis. *Front Neurosci*. 2021;15:701308.
54. Wang S, Millward JM, Hanke-Vela L, et al. MR elastography-based assessment of matrix remodeling at lesion sites associated with clinical severity in a model of multiple sclerosis. *Front Neurol*. 2020;10:1382.
55. Jost G, Frenzel T, Lohrke J, et al. Penetration and distribution of gadolinium-based contrast agents into the cerebrospinal fluid in healthy rats: a potential pathway of entry into the brain tissue. *Eur Radiol*. 2017;27:2877–2885.
56. Rasschaert M, Idée JM, Robert P, et al. Moderate renal failure accentuates T1 signal enhancement in the deep cerebellar nuclei of gadodiamide-treated rats. *Invest Radiol*. 2017;52:255–264.
57. Taoka T, Naganawa S. Gadolinium-based contrast media, cerebrospinal fluid and the glymphatic system: possible mechanisms for the deposition of gadolinium in the brain. *Magn Reson Med Sci*. 2018;17:111–119.
58. Nehra AK, McDonald RJ, Bluhm AM, et al. Accumulation of gadolinium in human cerebrospinal fluid after gadobutrol-enhanced MR imaging: a prospective observational cohort study. *Radiology.* 2018;288:416–423.
59. Rasschaert M, Schroeder JA, Wu TD, et al. Multimodal imaging study of gadolinium presence in rat cerebellum: differences between Gd chelates, presence in the Virchow-Robin space, association with lipofuscin, and hypotheses about distribution pathway. *Invest Radiol*. 2018;53:518–528.
60. Öner AY, Barutcu B, Aykol Ş, et al. Intrathecal contrast-enhanced magnetic resonance imaging-related brain signal changes: residual gadolinium deposition? *Invest Radiol*. 2017;52:195–197.
61. Solár P, Zamani A, Kubíčková L, et al. Choroid plexus and the blood-cerebrospinal fluid barrier in disease. *Fluids Barriers CNS*. 2020;17:35.
62. Engelhardt B, Wolburg-Buchholz K, Wolburg H. Involvement of the choroid plexus in central nervous system inflammation. *Microsc Res Tech*. 2001;52:112–129.
63. Balasa R, Barcutean L, Mosora O, et al. Reviewing the significance of blood-brain barrier disruption in multiple sclerosis pathology and treatment. *Int J Mol Sci*. 2021;22:8370.
64. Fresegna D, Bullitta S, Musella A, et al. Re-examining the role of TNF in MS pathogenesis and therapy. *Cell*. 2020;9:2290.
65. Robinson AP, Harp CT, Noronha A, et al. The experimental autoimmune encephalomyelitis (EAE) model of MS: utility for understanding disease pathophysiology and treatment. *Handb Clin Neurol*. 2014;122:173–189.
66. Taupitz M, Stolzenburg N, Ebert M, et al. Gadolinium-containing magnetic resonance contrast media: investigation on the possible transchelation of Gd^{3+} to the glycosaminoglycan heparin. *Contrast Media Mol Imaging*. 2013;8:108–116.
67. Popescu BF, Robinson CA, Rajput A, et al. Iron, copper, and zinc distribution of the cerebellum. *Cerebellum*. 2009;8:74–79.
68. White GW, Gibby WA, Tweedle MF. Comparison of Gd(DTPA-BMA) (Omniscan) versus Gd(HP-DO3A) (ProHance) relative to gadolinium retention in human bone tissue by inductively coupled plasma mass spectroscopy. *Invest Radiol*. 2006;41:272–278.
69. Darrah TH, Prutsman-Pfeiffer JJ, Poreda RJ, et al. Incorporation of excess gadolinium into human bone from medical contrast agents. *Metallomics*. 2009;1:479–488.
70. Murata N, Murata K, Gonzalez-Cuyar LF, et al. Gadolinium tissue deposition in brain and bone. *Magn Reson Imaging*. 2016;34:1359–1365.
71. Ramalho J, Semelka RC, Ramalho M, et al. Gadolinium-based contrast agent accumulation and toxicity: an update. *AJNR Am J Neuroradiol*. 2016;37:1192–1198.
72. Thakral C, Abraham JL. Gadolinium-induced nephrogenic systemic fibrosis is associated with insoluble Gd deposits in tissues: in vivo transmetallation confirmed by microanalysis. *J Cutan Pathol*. 2009;36:1244–1254.
73. Gromov D, Toikka A. Toward formal analysis of thermodynamic stability: Le Chatelier-Brown principle. *Entropy (Basel)*. 2020;22:1113.
74. Bredholt M, Frederiksen JL. Zinc in multiple sclerosis: a systematic review and Meta-analysis. *ASN Neuro*. 2016;8:175909141665151.
75. Choi BY, Jung JW, Suh SW. The emerging role of zinc in the pathogenesis of multiple sclerosis. *Int J Mol Sci*. 2017;18:2070.
76. Puttagunta NR, Gibby WA, Smith GT. Human in vivo comparative study of zinc and copper transmetallation after administration of magnetic resonance imaging contrast agents. *Invest Radiol*. 1996;31:739–742.
77. Rasschaert M, Emerit A, Fretellier N, et al. Gadolinium retention, brain T1 Hyperintensity, and endogenous metals: a comparative study of macrocyclic versus linear gadolinium chelates in renally sensitized rats. *Invest Radiol*. 2018;53:328–337.
78. Humpel C. Organotypic brain slice cultures. *Curr Protoc Immunol*. 2018;123:e59.
79. Aktas O, Smorodchenko A, Brocke S, et al. Neuronal damage in autoimmune neuroinflammation mediated by the death ligand TRAIL. *Neuron*. 2005;46:421–432.
80. Tweedle MF, Wedeking P, Kumar K. Biodistribution of radiolabeled, formulated gadopentetate, gadoteridol, gadoterate, and gadodiamide in mice and rats. *Invest Radiol*. 1995;30:372–380.
81. Bower DV, Richter JK, von Tengg-Kobligk H, et al. Gadolinium-based MRI contrast agents induce mitochondrial toxicity and cell death in human neurons, and toxicity increases with reduced kinetic stability of the agent. *Invest Radiol*. 2019;54:453–463.
82. Xia Q, Feng X, Huang H, et al. Gadolinium-induced oxidative stress triggers endoplasmic reticulum stress in rat cortical neurons. *J Neurochem*. 2011;117:38–47.
83. Radbruch A, Richter H, Bücker P, et al. Is small fiber neuropathy induced by gadolinium-based contrast agents? *Invest Radiol*. 2020;55:473–480.
84. Smith AP, Marino M, Roberts J, et al. Clearance of gadolinium from the brain with no pathologic effect after repeated administration of gadodiamide in healthy rats: an analytical and histologic study. *Radiology.* 2017;282:743–751.
85. Habermeyer J, Boyken J, Harrer J, et al. Comprehensive phenotyping revealed transient startle response reduction and histopathological gadolinium localization to perineuronal nets after gadodiamide administration in rats. *Sci Rep*. 2020;10:22385.
86. Roccatagliata L, Vuolo L, Bonzano L, et al. Multiple sclerosis: hyperintense dentate nucleus on unenhanced T1-weighted MR images is associated with the secondary progressive subtype. *Radiology.* 2009;251:503–510.
87. Schlemm L, Chien C, Bellmann-Strobl J, et al. Gadopentetate but not gadobutrol accumulates in the dentate nucleus of multiple sclerosis patients. *Mult Scler*. 2017;23:963–972.
88. Forslin Y, Shams S, Hashim F, et al. Retention of gadolinium-based contrast agents in multiple sclerosis: retrospective analysis of an 18-year longitudinal study. *AJNR Am J Neuroradiol*. 2017;38:1311–1316.
89. Cocozza S, Pontillo G, Lanzillo R, et al. MRI features suggestive of gadolinium retention do not correlate with expanded disability status scale worsening in multiple sclerosis. *Neuroradiology.* 2019;61:155–162.
90. McDonald RJ, McDonald JS, Dai D, et al. Comparison of gadolinium concentrations within multiple rat organs after intravenous administration of linear versus macrocyclic gadolinium chelates. *Radiology.* 2017;285:536–545.

Curriculum Vitae

Mein Lebenslauf wird aus datenschutzrechtlichen Gründen in der elektronischen Version meiner Arbeit nicht veröffentlicht.

Publication list

Top journal publication (thesis):

Anderhalten L, Silva RV, Morr A, Wang S, Smorodchenko A, Saatz J, Traub H, Mueller S, Boehm-Sturm P, Rodriguez-Sillke Y, Kunkel D, Hahndorf J, Paul F, Taupitz M, Sack I, Infante-Duarte C. Different Impact of Gadopentetate and Gadobutrol on Inflammation-Promoted Retention and Toxicity of Gadolinium Within the Mouse Brain. *Investigative radiology*. 2022;57(10):677-88. DOI: 10.1097/rli.0000000000000884.
Advance online publication: https://doi.org/10.1097/RLI.0000000000000884

Journal Impact Factor (2020): ***6.016***

Additional publications:

Ludwig R, Malla B, Höhrhan M, Infante-Duarte C, **Anderhalten L**. Investigating the Mitoprotective Effects of S1P Receptor Modulators Ex Vivo Using a Novel Semi-Automated Live Imaging Set-Up. *Int J Mol Sci*. 2023;25(1). DOI: 10.3390/ijms25010261.

Praet J*, **Anderhalten L***, Comi G, Horakova D, Ziemssen T, Vermersch P, Lukas C, van Leemput K, Steppe M, Aguilera C, Kadas EM, Bertrand A, van Rampelbergh J, de Boer E, Zingler V, Smeets D, Ribbens A, Paul F. A future of AI-driven personalized care for people with multiple sclerosis. Front Immunol. 2024;15:1446748. DOI: 10.3389/fimmu.2024.1446748. * Contributed equally.

Anderhalten L, Wohlrab F, Paul F. Emerging MRI and biofluid biomarkers in the diagnosis and prognosis of multiple sclerosis. The Lancet Regional Health – Europe. 2024;44. DOI: 10.1016/j.lanepe.2024.101023.

Acknowledgments

I am sincerely grateful to my supervisors Carmen Infante Duarte, Matthias Taupitz, and Volker Siffrin for their brilliant support during my MD/PhD study, excellent scientific education, and productive discussions. I would like to express my special thanks to Carmen, who always stood by my side in a supportive, motivating, and critical manner. I am grateful for the cordial work environment and your trust and appreciation. Your supervision has made me an enthusiastic, independent researcher and shaped me for my further scientific career.

I would like to thank the whole AG Infante Duarte, who supported me during my time in the laboratory. Thank you for the lively scientific exchange, the productive feedback, and the time we experienced together; be it at conferences, in laboratory meetings, or in our private time. Special thanks to Shuanqing Wang, who introduced me to the animal MRI scanner and supported me during the first year of my doctorate. To Rafaela Viera da Silva, thanks for your expertise and help with the experimental mice, in particular the EAE inductions. To Natascha Asselborn, thank you for the expert technical assistance during my MD/PhD study.

To Alina Smorodchenko, who skilfully introduced me to the generation of organotypic hippocampal slice cultures, and to Susanne Mueller, who actively supported me with the analysis of MRI data. I further want to thank Heike Traub, Jessica Saatz, Desiree Kunkel, and Yasmina Rodriguez-Sillke for the excellent collaboration. Without your expertise in sample processing using LA-ICP-MS, ICP-MS, and IMC it would not have been possible to work on the aims of my doctoral thesis.

I am thankful to the Hertie Foundation for financially supporting me with a scholarship and giving me the opportunity to attend a summer school and two international congresses during my doctoral phase. Thank you also for the organization of enriching reporting symposia, workshops, and lively scientific discussions.

To my partner, who stood by my side during the entire doctoral thesis and picked me up after long laboratory shifts. To my little sister, who encouraged me during the manuscript preparation and revision, providing me with fabulous food. And to my parents, Petra and Claus, who made my academic path possible and actively supported me during my doctoral phase.